

João Ricardo Silva Barbosa

Bachelor in Micro and Nanotechnologies Engineering

Point contact structures for Thin Film Solar Cells

Dissertation submitted in partial fulfillment of the requirements for the degree of

Master of Science in Micro and Nanotechnology Engineering

Adviser: Pedro Salomé, Professor, PhD, International

Iberian Nanotechnology Laboratory

Co-adviser: Manuel João Mendes, Professor, PhD, NOVA

University of Lisbon

Examination Committee

Chair: Rodrigo Martins, Full Professor, NOVA

University of Lisbon

Rapporteur: Rui Vilão, Professor, University of Coimbra Member: Pedro Salomé, PhD, International Iberian

Nanotechnology Laboratory



Point contact structures for Thin Film Solar Cells Copyright © João Ricardo Silva Barbosa, NOVA School of Science and Technology, NOVA University Lisbon. The NOVA School of Science and Technology and the NOVA University Lisbon have the right, perpetual and without geographical boundaries, to file and publish this dissertation through printed copies reproduced on paper or on digital form, or by any other means known or that may be invented, and to disseminate through scientific repositories and admit its copying and distribution for non-commercial, educational or research purposes, as long as credit is given to the author and editor.

Acknowledgements

Each and every Master's student has to set out on their own pilgrimage through the realms of Science. Yet, this journey is rarely accomplished alone, and mine was no exception. Therefore, I want to acknowledge and express my thankfulness to everyone that in some shape or form aided me in this journey. Firstly, I want to disclose my gratitude towards Professor Rodrigo Martins and Professor Elvira Fortunato, for the opportunity by them provided through not just the creation of the Master course in Micro and Nanotechnology Engineering, but also the access to the exceptional facilities at CENIMAT|i3N and CEMOP.

To my adviser Professor Pedro Salomé, I have nothing but high praise to give and admiration to show. In the past four years, not only I have learned so much from you, but I have grown to be a better person and student of science. I thank you for all the support and encouragement you provided throughout all these years and this thesis. Likewise, I want to convey my gratitude to Professor Manuel Mendes, not just due to the help by him provided in this thesis, for but as well for all that you taught me throughout the entire course.

I want show my gratefulness to everyone in the Nanofabrication for Optoelectronic Applications group, as I had an amazing experience with each and everyone of you. Thank you Professor Paulo Fernandes, Dr. Jennifer Teixeira and MSc. Marco Alberto for everything that you taught me and for all the support by you selflessly provided. It is immeasurable how much I have learned from all of you. To MSc. José Cunha and MSc. Tomás Lopes I can not thank you enough for all the teachings, help, attention and company so graciously provided by you both. Without a doubt, my work would be considerably less valuable without your wonderful contributions. A special thank you to MSc. Kevin Oliveira and MSc. António Oliveira for the phenomenal and generous support you two provided throughout my thesis, and made it possible to achieve the attained results. Likewise, I want to thank André Violas, Célia Rocha and Margarida Monteiro for not just the assistance and information you all provided during this thesis, but as well for everything you helped me with during the entirety of this degree. This thesis would not be possible without the expertise of Dr. Jérôme Borme, always available to no just provide exceptional advice, but ever helpful in the cleanroom as well. I also want to thank Olivier Donzel-Gargand for the invariably beautiful microscopy data you so generously provided. The cleanroom fabrication processes would not be possible without the support and expertise of Professor João Gaspar, MSc. Helder Fonseca, MSc. Joana Santos, MSc. José Rodrigues and Dr. José Fernandes. Thank you for all the assistance and advice, kindly given to me since the very beginning. I want to extend my gratitude to Dr. Wei-Chao Chen and Professor Marika Edoff for your gracious help and cooperation.

To Margarida Glória I give you my thank you, as without you, the quality of my writing would surely have plunged. To my family I dedicate this thesis, was without all your effort, dedication and kindness this would not be possible. Lastly but certainly not least, I have to thank Gabriela Monteiro for all your affection, devotion, helpfulness and support all along. Without you, I would not be who I am today.

"Nothing of me is original. I am the combined effort of everyone I've ever known" Chuck Palahniuk

Abstract

Ultrathin Cu(In, Ga)Se₂ (CIGS) has an immense potential to expand the application spectrum of photovoltaic technologies, such as Building Integrated Photovoltaics (BIPV) or as the power source Internet of Things devices, due to its high efficiency, flexibility, stability and low cost. However, since the low cost stems from a absorber thickness reduction, ultrathin CIGS faces some challenges that are not present in standard thickness CIGS, such as a decreased light absorption and degraded electrical performance.

This thesis is focused on the development and fabrication of mitigation strategies through the use of rear passivation and optically enhancing structures fabricated by several e-beam lithography steps. Due to the elemental diffusion and detrimental reactions with selenium, the encapsulation of the optically enhancing rear reflector ensures that the CIGS absorber will not be negatively affected, while simultaneously increasing the photocurrent generation. Additionally, the rear passivation dielectric layer reduces the recombination velocity of the Mo/CIGS interface and, consequently, increased the open circuit voltage. In addition to the fabrication and characterization of solar cells with an encapsulated passivation layer, these modifications were studied with optical and electrical simulations and delivered a 3.2 % absolute efficiency increase.

Keywords: CIGS; solar cells; ultrathin; passivation; optical enhancement; e-beam; FDTD; CHARGE

Resumo

Cu(In, Ga)Se₂ (CIGS) ultrafino possui amplo potencial para expandir o leque de aplicações das tecnologias fotovoltaicas, por exemplo, painéis fotovoltaicos integrados em edifícios (BIPV), ou como fonte de alimentação para dispositivos Internet das Coisas, graças á alta eficiência, flexibilidade, estabilidade e baixo custo. Todavia, visto que o baixo custo provém da redução da espessura do CIGS, as células ultrafinas encontram desafios que não estão presentes no CIGS de espessura padrão, nomeadamente a redução da absorção da luz incidente e um decréscimo no desempenho elétrico.

Esta tese foca-se no desenvolvimento e fabricação de estratégias de mitigação, através da aplicação de estruturas de passivação traseira e aumento ótico, fabricadas por vários passos de litografia de feixe de eletrões. O encapsulamento do refletor ótico traseiro garante que o CIGS não será negativamente afetado devido à difusão atómica e reações prejudiciais com o selénio, enquanto que ao mesmo tempo a geração da fotocorrente é aumentada. Adicionalmente, a passivação traseira constituída por uma camada de dielétrico, reduz a velocidade de recombinação na interface Mo/CIGS, e consequentemente, leva ao aumento da tensão de circuito aberto. Além da fabricação e caracterização de células solares com passivação encapsulada, estas modificações foram estudadas através de simulações óticas e elétricas, resultando num aumento absoluto de 3.2 % da eficiência da célula solar.

Palavras-chave: CIGS; células solares; ultrafino; passivação; aumentos óticos; feixe de eletrões; FDTD; CHARGE

Contents

Lis	st of Figures	xv					
Lis	st of Tables	xvii					
Ac	ronyms						
Sy	rmbols	xxi					
Mo	otivation and objectives	xxv					
1	Introduction	1					
	1.1 State of the Art 1.2 Single Diode Equivalent Model 1.3 Carrier Recombination & Passivation	2 2 4					
	1.4 Light Management	4					
2	Materials and Methods 2.1 Device Fabrication Process	7 7 8 9 10					
	2.2 Characterization	11 11 11 11					
3	Results and Discussion	13					
	3.1 Previous Results 3.1.1 Insulator Passivation Layer 3.1.2 Metal back reflector	13 13 15					
	3.2 Optical Simulations	17 18 22					
	3.3.1 Electrical Simulations Results	22 25					
4	Conclusion and Future Perspectives	29					
Bi	bliography	31					
Ap	ppendices	41					
A	FDTD Simulations Supplementary Data	41					
В	CHARGE Simulations Supplementary Data	43					
C	Python Tools	47					
Ar	nnexes	49					

C	\bigcirc	NI	$\Gamma \Gamma$	NT	TS
•	.,	I N	ΙС	IN	כיו

Ι	Annex 1	49
II	Annex 2	51

List of Figures

0.1	A PV facade of a building constructed by ZSW in Stuttgart	
1.1	Chalcopyrite structure of CuInSe ₂ . The Cu atoms are represented in red, In in blue and Se in green. In CuGaSe ₂ crystals, the In is replaced by Ga atoms	1
1.2	Structural schematic of a CIGS solar cell. Diagram for illustrative purposes. Not at scale.	1
1.3	Equivalent circuit and Current-Voltage plot	3
1.4	Locations where metal diffusion and selenium reaction occur during the CIGS fabrication process.	5
2.1	Proposed passivation structure. Diagrams for illustrative purposes. Not at scale	7
2.2	Schematic representing the alignment markers fabrication process	8
2.3	Schematic representing the fabrication process of the metal mirror layer	9
2.42.5	Schematic representing the fabrication process of the insulator layer	10
3.1		13
3.2	Results from J-V and EQE measurements of reference and passivated solar cells	14
3.3	Pseudo-color SEM cross sections of a reference and passivated solar cell. The Mo rear contact is colored in blue, the SiO ₂ in red, CIGS in green, CdS in purple and the	
	ZnO/Zno:Al window layer in orange. The passivated solar cell has a insulator pitch of 8 μm.	15
3.4	Schematic representing the fabricated structures	15
3.5	Results from J-V and EQE measurements of reference and passivation/reflector samples	16
3.6	Results from the design parameters optimization simulations	19
3.7	Optical performance of the several iterations of rear contact passivation and optically enhancing layers.	20
3.8	Current density generated throughout the height of the CIGS layer	21
3.9	Simulated power conversion efficiency and Fill Factor depending on the total rear contact passivated area	23
3.10	Simulated J-V plots of the reference and encapsulated designs	23
3.11	Simulated EQE with and without charge transport mechanics of passivated and reference solar cells. The charge carrier extraction ratio per wavelength is shown	
	with the respective axis on the right side	24
		25
	SEM images showcasing an example for both a successful and failed lithographic alignment.	26
	Electrical measurements of reference and encapsulated architecture solar cells	26
3.15	Electronic microscopy analysis of the substrate before and after the CIGS deposition process	27
3.16	Elemental composition distribution of an encapsulated rear passivated CIGS solar	28
3.17	Aluminium elemental distribution in green, overlayed over the oxygen elemental distribution.	28
A.1	Generation rate per wavelength and depending on the height of the CIGS, with 0 of the CIGS height at the Mo rear contact.	41

LIST OF FIGURES

	Optical performance of the several iterations of rear contact passivation and optically enhancing layers.	
A.3	Simulated reflection of 10 nm Al and Al ₂ O ₃ films	42
	Simulated electron current density distribution in a passivated ultrathin CIGS solar cell	46
C.1	Screen capture of the graphical user interface developed for the automation scripts.	47

List of Tables

3.1	Average and standard deviation values of each passivation pattern	14
3.2	Average and standard deviation values of each sample with different metals as back	
	reflector	16
3.3	Simulated figures of merit of the reference and encapsulated designs	23
3.4	Average and standard deviation values of the J-V figures of merit.	27
B.1	Model parameters used in the CIGS electrical model	45

Acronyms

AFM - Atomic Force Microscopy

BIPV - Building-Integrated Photovoltaics

CBD - Chemical Bath Deposition

CIGS - $Cu(In_{1-X}Ga_X)Se_2$

DC - Direct Current

EDS - Energy Dispersive X-ray Spectroscopy

EQE - External Quantum Efficiency

FDTD - Finite-Difference Time-Domain Method

FF - Fill Factor

ICP - Inductively Coupled Plasma Etching

imec - Interuniversity Microelectronics Centre

INL - International Iberian Nanotechnology Laboratory

IoT - Internet of Things

J-V - Current Density-Voltage

NIR - Near-infrared

NOA - Nanofabrication for Optoelectronic Applications

PECVD - Plasma Enhanced Chemical Vapor Deposition

PMMA - Poly(methyl methacrylate)

PR - Photoresist

PV - Photovoltaic

SEM - Scanning Electron Microscopy

SLG - Soda-Lime Glass

STEM - Scanning Transmission Electron Microscopy

TEM - Transmission Electron Microscopy

TFSC - Thin Film Solar Cell

Symbols

- A Diode ideality factor
- Abs Total absorbed power
- Al Aluminium
- $\textbf{\textit{I}}_{\textbf{\textit{AM}}\textbf{\textit{1.5G}}}$ Standard terrestrial solar spectrum 'Air Mass 1.5 Global'- W \cdot m $^{-2}$ \cdot m $^{-1}$
- a-Si Amorphous silicon
- E_G Bandgap eV
- N_t Bulk-trap concentration cm⁻³
- c Speed of light in vacuum m/s
- CdS Cadmium Sulfide
- CdTe Cadmium Telluride
- c-Si Crystalline silicon
- Cu Copper
- \overrightarrow{D} Displacement field C/m2
- $\boldsymbol{D_n}$ Electron Diffusion coefficient cm²/s
- D_p Hole Diffusion coefficient cm²/s
- $|E|^2$ Electric field intensity V/cm
- \overrightarrow{E} Electric field V/m
- η Power conversion efficiency %
- χ Electron affinity eV
- C_n Electron capture rate cm⁶/s
- m_e^* Electron effective mass kg
- au_e Electron carrier lifetime s
- m_e Electron rest mass kg
- σ_e Capture cross-section for electrons cm²
- SRV_n Electron surface recombination velocity cm/s
- ε_0 Permittivity of free space- F/m
- ε_r Complex relative dielectric permittivity F/m
- Ga Gallium
- G_S Series conductance mS/cm²

 G_{SH} - Shunt conductance - mS/cm²

h - Planck constant

 \overrightarrow{H} - Magnetic field - A/m

 C_p - Hole capture rate - cm⁶/s

 m_h^* - Hole effective mass - kg

 τ_h - Hole carrier lifetime - s

 σ_h - Capture cross-section for holes - cm²

 SRV_p - Hole surface recombination velocity - cm/s

i-ZnO - Intrinsic Zinc Oxide

In - Indium

J - Current density - A/m²

 J_0 - Saturation-current density- A/cm²

 J_{MP} - Maximum Power Current Density- A/m²

 J_{ph} - Photogenerated current density - A/cm²

 J_{SC} - Short-Circuit Current density - A/m²

k - Extinction coefficient

 k_B - Boltzmann constant - m² · kg · s⁻² · K⁻¹

 λ - Wavelength - m

Mo - Molybdenum

MoSe₂ - Molybdenum diselenide

n - Concentration of free electrons - cm⁻³

n - Refractive index

Ni - Nickel

 ω - Angular frequency - rad/s

p - Concentration of free holes - cm⁻³

 P_{abs} - Power absorbed per unit of volume - W/m³

 μ_0 - Permeability of free space - H/m

Pinc - Incident Optical Power- mW/cm²

poly-Si - Polycrystalline silicon

q - Elementary charge - C

 R_r - Radiative recombination rate - cm³/s

- R_n Net electron recombination rate cm⁻³s⁻¹
- R_p Net hole recombination rate cm⁻³s⁻¹
- ρ Charge density C/cm³
- R_{SH} Shunt resistance Ω
- R_S Series resistance Ω
- Se Selenium
- $N_C\,$ Effective density of states in conduction band 1/cm 3
- N_V Effective density of states in valence band $1/\text{cm}^3$
- *t* Time s
- T Temperature K
- μ_e Electron mobility cm²/V · s
- μ_h Hole mobility cm²/ $V \cdot$ s
- V Electrostatic potential V
- V_{MP} Maximum Power Voltage V
- V_{OC} Open Circuit Voltage V
- ϕ Work function eV
- **ZnO** Zinc Oxide

Motivation and Objectives

In today's modern world, the importance of the photovoltaic (PV) module, as a source of clean energy is undeniable. Be it as a cheap energy source, as an alternative to fossil fuels or as one of the most environmental friendly energy supplies available to Humanity [1–4]. Consequently, the PV industry has been on the rise, with a compound annual growth rate of the production volume at over 40 % in the past 15 years [5].

Due to its current production low-cost, good light to power conversion efficiency values[6] and high existent manufacturing capability, the PV market has been historically dominated by the c-Si technology[7, 8], with currently 95% of the world's market share[9]. This dominance, however, does not signify that c-Si, also designated as First Generation PV, is the be-all and end-all of photovoltaic scientific know-how. The scientific comprehension of solar cells has had a remarkable expansion in the last decades, since the start of the c-Si dominance, thus, alternatives with interesting properties over c-Si have been developed, opening application possibilities outside the reach of traditional PV. One of said alternatives, are Thin Films Solar Cells (TFSC), a term typically applied to CdTe, a-Si and $Cu(In_{1-X}Ga_X)Se_2$ (CIGS) solar cells. Another designation frequently attributed to the specified technologies is Second Generation PV. Designated as "thin", since with thicknesses in the range of single digit µm and below 10, 11], Second Generation PV solar cells are dozens to hundreds of times thinner than standard silicon solar cells, which have thicknesses around 200 µm[10–12]. Second Generation solar cells have the ability to function with such a reduction in the thickness values, due to the materials composing them being classified as direct band-gap semiconductors, opposed to the indirect band-gap of c-Si. The direct band-gap bestows the TFSCs with much higher optical absorption coefficients[11, 13], when compared to the their first generation c-Si counterpart, as the Figure 0.1 shows.

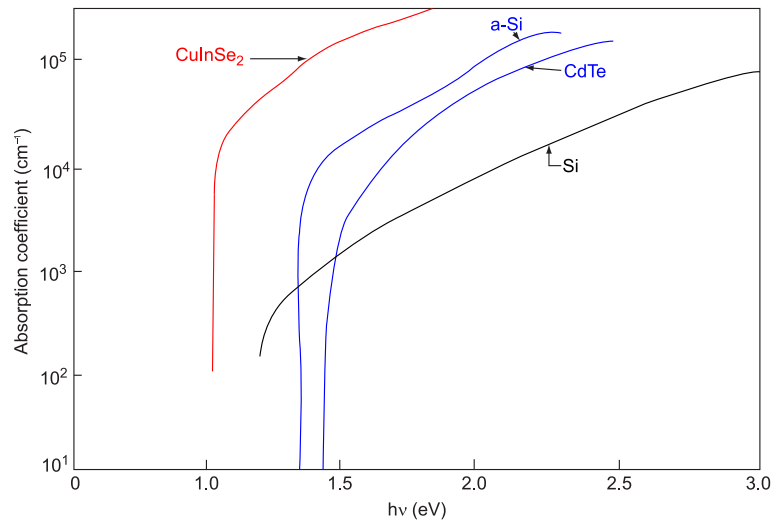


Figure 0.1: Absorption spectra of various semiconductors. Adapted from [13].

Additionally, TFSCs exhibit superior low light performance[14, 15], relatively to the first generation c-Si solar cells. This is in turn, translated into superior stability of the light to power conversion efficiency value in locations where the weather conditions lead to an increased offaxis diffuse incident light [14]. Furthermore, the superior low light performance enables the use of TFSCs in low irradiance environments and low power applications, such as Internet of Things smart sensors inside a building[16, 17]. Unlike standard c-Si, TFSCs have a range of suitable materials that can be employed as the solar cell substrate, such as flexible polymer films and metal foils[18, 19], or more traditional rigid soda-lime glass. This capability gives TFSCs the option to be fabricated for a specific use case, thus, allowing for a greater optimization of

the design for each application. A good showcase of the exceptional potential of TFSCs for certain uses cases, resulting from the sum of these advantages, is in architectural integration applications[20–22]. A striking example of what can already be achieved with standard PV modules, is a new building constructed by the Centre for Solar Energy and Hydrogen Research (ZSW) in Stuttgart, as show in the Figure 0.2.



Figure 0.2: A PV facade of a building constructed by ZSW in Stuttgart[23].

The lighter and flexible substrates allow for a more seamless installation of solar panels in the building structure, without the requirement of stringent structural support. Additionally, the greater electrical performance stability due to higher off-axis diffuse incident light performance, results in a reduced negative impact compared to c-Si, if the installation is placed in a non-ideal position relative to the solar illuminance. The impact in the visual aspect is significantly mitigated as well, as the second generation solar cells do not possess the large grain patterns found in p-Si, nor do they necessarily require metal grids for the electrical contacts, since it is possible to delegate that function to transparent conductive oxides. Furthermore, TFSCs are not limited by the wafer sizes, and can be fabricated into continuous sheets or rolls, foregoing the interconnects between individual cells, found on traditional c-Si solar panels. The argument for the architectural use of TFSCs is further strengthened by the commercial availability of CIGS solar panels with multiple color options[24, 25]. Taking a step even further, second generation solar cells can even be deployed as semi-transparent windows[20, 26], thus not only can they act as electrical power generation devices, but can also provide to some degree, additional building thermal management capabilities.

Even though thin film solar cells, namely CdTe, a-Si and CIGS share several common advantageous characteristics, these three technologies do not possess the same level of success and future potential. Amorphous silicon solar cells are quite behind the other two technologies in terms of power conversion efficiency, with the best a-Si research cell achieving a 14% record efficiency, while research CdTe and CIGS solar cells have reached 22.1% and 23.4% respectively[10, 27]. Furthermore, a-Si solar cells suffer from light-induced degradation due to the Staebler-Wronski effect[28] thus, between the low efficiencies and the degradation under illumination, the commercial prospects of a-Si are quite limited[9, 29]. Even though cadmium telluride has had the largest market share of thin-film PV in the last decade[9], due mainly to this technology having the lowest price per kW of any TFSCs[10, 30, 31], worries about the toxicity of cadmium[29, 32, 33] during the manufacture and the disposal of CdTe solar cells are poised to only increase if the market share of CdTe PV increases as well. On the other hand, CIGS boasts the lowest environmental impact, when compared to the remaining TFSCs and c-Si[34], and even though CIGS historically uses cadmium sulfide as the buffer layer, the latest world records have been achieved with a Cd free solar cells[35, 36]. Moreover, CIGS has the

TFSC efficiency lead in both research cells and commercial modules [6, 27, 37], even slightly surpassing the poly-Si research cell world record, with a 0.1 % [27] advantage over the silicon counterpart, at the time of writing. Even the price advantage that CdTe has held over CIGS is being threatened, as cost projections predict a significant reduction in the CIGS cost per watt, once certain technological hurdles are overcome and a greater large scale manufacturing effort takes place [21, 25, 38].

One of the main factors currently thwarting the market expansion of the CIGS technology into the broader PV market, is the price advantage enjoyed by c-Si, mainly poly-Si over TF-SCs[39], as price per kW is one of the most important factors in the energy industry. Additional points of contention are the claims that the natural reserves of the CIGS essential element, Indium, are not large enough to accommodate the boom of the CIGS industry, and that supply issues and price fluctuations will inevitably arise [40, 41]. To tackle these issues, CIGS can resort to its set of properties in order to gain the advantage. By reducing the absorber thickness from 2 μm to 0.5 μm, the dependence in the scarce element is also slashed to a quarter, increasing its immunity to price fluctuations, furthermore, as less material is required for the fabrication of the same area, the machine time required will therefore be reduced. These improvements will have a compounding effect on the price of the CIGS solar cell and increasing its market attractiveness. Additionally, ultrathin CIGS solar cells have the potential to achieve higher electrical performance, due to lower bulk recombination, when compared to standard bulk thickness CIGS[42-44]. Even if CIGS fails to beat c-Si head-on, its peculiar properties make it much more well suited for applications where the shortcomings of c-Si prevent it from large scale deployment, making CIGS still a worthy endeavour to develop[34, 38, 45]. On the other hand, reducing the absorber layer thickness down to a quarter, does have negative effects, such as, the incomplete optical absorption of the incident spectrum[46], which will result in degraded power conversion efficiencies. Moreover, the absorber thickness decrease negatively affects the electrical performance of the CIGS, since it results in an increase of the recombination of the charge carriers in the rear contact interface[47, 48], with this being one of the main limiting factors of CIGS solar cells[49].

To tackle the points of concern of ultrathin devices, more specifically, the rear contact recombination, the deposition of insulating material between the rear contact and the absorber layer as a passivation layer, has been proposed and demonstrated by several authors[43, 50-52], including past work developed by the Nanofabrication for Optoelectronic Applications (NOA) group at the International Iberian Nanotechnology Laboratory (INL), where I partook in the development of the fabrication process of said passivating structure[53]. While the passivation layer is focused on improving the electrical performance, it possesses beneficial optical properties, partially curtailing the optical losses[53]. Nonetheless, even with the dielectric layer, the optical losses are still significant, and need to be thoroughly addressed[54]. Consecutively, the optical deficit can be decomposed into two smaller challenges affecting the solar cell performance: i) high optical parasitic losses due to the high optical absorption and poor reflectivity of the molybdenum (Mo) rear contact[55]; ii) weak optical absorption of the absorber layer in the near infrared range [49]. Replacing the Mo back contact with a metal with higher reflection properties is not an option, since Mo has empirically outperformed other alternatives, and it has been the only metal to reliably form a good electrical contact with CIGS at the rear contact [56, 57]. Thus, in order to reduce the optical parasitic losses and increase the mean optical path, a highly reflective metal film can be deposited between the rear contact metal and the dielectric passivation layer, therefore providing an increase in the rear reflection and the augment to the optical absorption of the CIGS layer, as a consequence of said reflection increase. Such work was performed by T. S. Lopes et al.[54], where once again I contributed in the fabrication development procedures. The results did not meet the expectations, as some CIGS solar cells had their performance severely degraded, and it was concluded that the culprit was the unwanted elemental diffusion from the metal reflector to the CIGS layer, which would then negatively

alter the characteristics of the absorber layer [19, 54, 56].

It is this pitfall of the previous architecture that lead to the need of the work that shall hereby be presented and developed. Therefore, the need to create a passivating structure with the correct optical properties, capable of increasing the optical absorption remains, but with the added constraint that the new layout needs to eliminate any possible diffusion paths between the metal film and the absorber layer. In other words, the design needs to encapsulate the metal, and shield it from contact with the CIGS. The structure will be fabricated using traditional cleanroom additive and subtractive techniques e.g. Magnetron Sputtering and Inductively Coupled Plasma Etching (ICP), with the addition of the use of electron beam lithography. The resulting product shall be characterized by Scanning Electron Microscopy (SEM), Transmission Electron Microscopy (TEM) and Scanning Transmission Electron Microscopy (STEM) Energy Dispersive X-ray Spectroscopy (EDS). Furthermore, the proposed structure will undergo optical simulations through Finite-Difference Time-Domain methods (FDTD) and additional 3D electrical simulations by a self consistent Poisson solver, all part of the *Lumerical Suite*[58], in order to better understand the underlying causes and effects, and better optimize the fabrication process.

1 | Introduction

 $Cu(In_{1-X}Ga_X)Se_2$ is a chalcopyrite semiconductor alloyed from the $CuInSe_2$ and $CuGaSe_2$ ternary compounds in a variable X ratio. It belongs to the I-II-VI $_2$ family of semiconductors, and it is the light absorbing material of the namesake CIGS class of thin film solar cells[59]. The crystal structure is organized in a tetragonal crystal system, where each Copper (Cu) or Indium/Gallium (In/Ga) atom has four bonds to a Selenium atom (Se). Conversely, each Se atom has two bonds to Cu and two to In/Ga[59]. A representation of the crystal structure is available in Figure 1.1. CIGS is a p-type semiconductor, and it is suitable as an absorber material due to its direct bandgap and comparatively high optical absorption coefficient, as demonstrated previously in Figure 0.1.

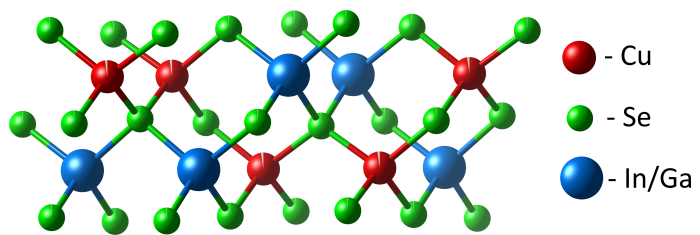


Figure 1.1: Chalcopyrite structure of CuInSe₂. The Cu atoms are represented in red, In in blue and Se in green. In CuGaSe₂ crystals, the In is replaced by Ga atoms[60, 61].

CIGS has the inherent ability to tailor its bandgap by varying the [Ga]/([Ga]+[In]) content ratio, creating the possibility of having different band gaps at different depths[47]. Furthermore, the electrical conductivity can be fine-tuned by varying the CIGS constitution, with one of the major contributing factors being the [Cu]/([Ga]+[In]) ratio[13, 62]. The CIGS quaternary compound is an intermediate layer in a heterostructure solar cell device, whose construction relevant to this work can be seen in the Figure 1.2, and is constituted in the following manner, starting from the bottom:

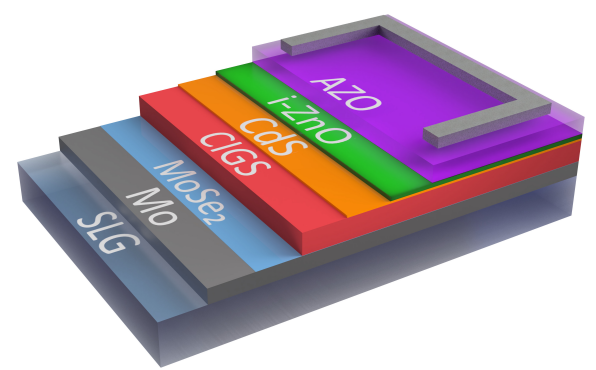


Figure 1.2: Structural schematic of a CIGS solar cell. Diagram for illustrative purposes. Not at scale.

i) The substrate is soda-lime glass (SLG), due to its widespread availability, relative low-cost and good thermal expansion compatibility with the CIGS[63]. Additionally, the sodium content from the glass will diffuse into the CIGS layer and significantly improve its performance[64]; ii) The rear contact is composed of molybdenum, due to the good adhesion it possesses with the SLG anddue the ohmic contact with CIGS, as result of the p-type semiconductor MoSe₂ layer that is formed during the CIGS deposition stage [56, 65]; iii) With the rear contact in place, the p-type CIGS layer is deposited, where Cu, In, Ga and Se are co-evaporated at specific rates in order to achieve the desired stoichiometry; iv) The p-n junction is then formed by the deposition of the CdS n-type buffer layer through Chemical Bath Deposition (CBD); v) The buffer layer is followed up by a transparent window bilayer composed of an intrinsic ZnO film and a second

ZnO layer doped with aluminium. The i-ZnO deposition process eliminates surface oxides from the CdS[66], and its high resistance aids in the elimination of shunt current paths and sites of locally enhanced recombination[67], while the Al:ZnO layer has a high conductivity for efficient charge extraction[59, 68]. vi) Concluding the fabrication, the following step consists in the deposition of a metal grid on top of the Al:ZnO layer, with the intention of facilitating the connection between the solar cell and external circuitry. This grid is composed of a Ni/Al/Ni stack deposited by evaporation, with the grid being delineated by a shadow mask. The first Ni layer function is to create an ohmic contact with the Al:ZnO, while the function of the second Ni layer is to shield the Al layer from atmospheric exposure. The purpose of the Al layer is to offer a current path with higher electrical conductivity.

1.1 State of the Art

With the first CuInSe₂ solar cells being created with crystals of said material in 1975[69], followed soon after by the development of the first CuInSe₂ thin film solar cell in 1976[70]. From then on, the CIGS technology has been under a constant development over the years, with efforts being focused on different sections of the solar cell structure throughout time[32].

Recently, the research efforts have been focused on tackling key issues hampering a wider market adoption of CIGS technology, with those being the toxicity of cadmium[71], the risk of indium supply scarcity in the foreseeable future[41] and its cost competitiveness when compared to the conventional Si-based solar cells[39].

The CIGS world record already belongs to a cadmium free cell[35], showing that it is not only possible to create efficient cells without Cadmium Sulfide (CdS), but that it is the way forward. In order to tackle possible indium supply chain restrictions, efforts have been made to develop solar cells with absorber thicknesses under a single µm, classified as ultrathin[72]. The reduction of the active layer thickness also has the benefit of reducing material usage, lowering cost and increasing manufacture throughput, which in turn, lowers cost even further. In order to tackle the reduced optical absorption created by the reduction of the absorber layers, efforts are being made with the intent of increasing the optical path through light trapping, by using reflective back structures[48, 54, 73] and nanoparticles[74]. Moreover, the electrical performance of ultrathin cells can be further improved by employing passivation layers, on both the front CIGS interface[75], and the back contact[50, 53]. These concepts are developed to a greater extent below. The work being developed in this thesis, will focus on tackling both the increase of the light absorption of the solar cell, and the electrical performance of the rear contact.

Additional efforts to lower the cost of these types of solar cells are under way, for instance, the use of flexible substrates, such as steel or polymer films[18], and the use of low-temperature and high-output production using printing techniques for the deposition of the active layer[76].

1.2 Single Diode Equivalent Model

In order to better understand the various phenomena that occur in a solar cell, and what are the causes and consequences of such, it is necessary to comprehend the electronic behaviour of a solar cell. For such, one can be aided by the use of a equivalent model constructed out of discrete electrical components of which, the properties are well understood. This will thus allow the determination of the equations that describe the behavior of the photovoltaic device. In this segment, the equivalent circuit is shown in Figure 1.3a, as well as a few important equations that describe the most important parameters of a solar cell.

The equivalent circuit is composed of a photogenerated controlled current source, I_{PH} , the I_D is the designation of the current flowing through the diode described by the Shockley diode equation, which represents the PN junction of the solar cell, and finally the two resistors R_P and R_S account for the parasitic parallel and series resistance present in real devices [77].

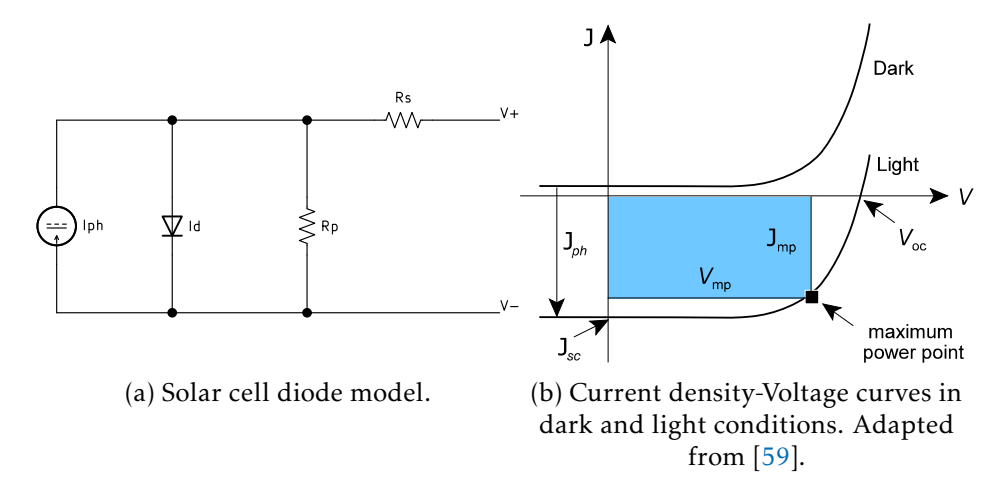


Figure 1.3: Equivalent circuit and Current-Voltage plot.

The most pertinent behaviour-describing equations will be displayed, while the deduction of said equations lays beyond the scope of this work, thus I relegate such developments to the referenced material [13, 77, 78].

The current-voltage relation in a solar cell is described by the following equation:

$$J = J_0 \cdot \left(\exp\left(\frac{qV - qJR_S}{Ak_BT}\right) - 1 \right) + \frac{V - JR_S}{R_{SH}} - J_{ph}$$

$$\tag{1.1}$$

where J, J_0 and J_{ph} represent the current density, the saturation current and the photogenerated current respectively. R_S and R_{SH} signify the specific series and shunt resistance ($\Omega \cdot \text{cm}^2$), as exemplified on Figure 1.3a. The diode ideality factor is represented by A, with V being the voltage difference on the solar cells terminals, while T is the temperature of the solar cell. Finally, k_B is the Boltzmann constant and q is the electron elementary charge.

When the current in the solar cell is equal to 0, the cell is in the "open circuit" condition, on which, the open circuit voltage is the following:

$$V_{OC} = \frac{Ak_bT}{q} \cdot \ln\left(\frac{J_{ph}}{J_0} + 1\right) \tag{1.2}$$

It is worth mentioning the logarithmic relation between the saturation current, J_0 , and the open circuit voltage of the solar cell, as it is this relation that gives further relevance and importance to the surface recombination and consequent passivation layer, such as it will be described in the Section 1.3.

One important figure of merit is the Fill Factor (FF), which is defined by the ratio of the product of the voltage and current density at maximum power (V_{MP} and J_{MP} respectively) by the product of the J_{SC} and V_{OC} , as shown in equation 1.3.

$$FF = \frac{V_{MP}J_{MP}}{V_{OC}I_{SC}} \tag{1.3}$$

Ranging between one and zero, the **FF** gives the ratio of how close the solar cell is near to an ideal solar cell, as it is affected by many deficiencies present in the solar cell, such as the series and shunt resistance mentioned antecedently, thus being an useful indicator of the overall quality of the solar cell.

Knowing J_{SC} , V_{OC} and **FF**, it is possible to calculate the light to power conversion efficiency of the solar cell (η), that is, how efficiently the solar cell can convert the power of the incident light into electrical power. The efficiency equation is the following:

$$\eta = \frac{J_{SC}V_{OC}FF}{P_{inc}} \tag{1.4}$$

P_{inc} stands for the incident optical power on the solar cell.

1.3 Carrier Recombination & Passivation

As elaborated in Motivation and in the section 1.1, it is desirable to couple the increase of CIGS solar cells efficiency, with the reduction of the absorber thickness. Howbeit, this subtraction is met with a degradation of the solar cell performance, manifested across all solar cell's figure of merit, i.e. the short-circuit current (I_{SC}), open-circuit voltage (V_{OC}), Fill Factor (FF) and efficiency(η). This section will focus in the V_{OC} deficiency, which is a consequence of an adverse effect present in the CIGS solar cells, the rear interface recombination. An effect that gains further prominence through the absorber thickness reduction since the photogeneration of carriers will be situated closer to the back contact, and thus the probability of the rear interface recombination will be higher [79, 80].

Recombination is the opposing mechanism of the fundamental photovoltaic effect. It consists in the charge carrier annihilation that occurs when an excited electron, through several mechanisms, stabilizes from the conduction band into an empty valence band state, thus occupying the vacant state that was represented by the hole charge carrier, effectively removing the electron from the photogenerated current. The subtraction from the photogenerated current can be represented as a current of opposing polarity, as is conventionally designated as the recombination current[81, 82]. The recombination current is detrimental to the solar cell performance, as it significantly impacts the V_{OC} . The reason being the logarithmic decrease of the V_{OC} with the increase of the dark saturation current (J_0), which in turn is dependent on the recombination current of the solar cell, as the equation 1.2 dictates [83]. Additionally, the reduction in charge carriers has a direct and negative impact on the short circuit current, further plunging the solar cell efficiency [84].

One of the critical locations in a CIGS solar cell, where of one the detrimental recombination processes occurs at a higher rate, is the rear contact interface between the CIGS and the MoSe₂ layer[50, 84–86]. This effect is already present on standard thickness solar cells, but in ultrathin devices, it gains further prominence as a larger portion of the generated minority charge carriers are located closer to this recombinative hotspot, meaning that the negative effects of the recombination are further augmented[47, 48]. Therefore, it is of the utmost importance that an effective approach is developed in order diminish the recombination velocity of the rear interface in ultrathin CIGS solar cells.

Since this obstacle is caused due do the interface between the CIGS absorber and the metal contact, one of the most direct approaches to have been deployed, is the reduction of the area between these two critical layers. This is designated by *chemical passivation*, a term originated in the silicon industry, that involves the reduction of the total number of electrically active defects in an interface, by selectively distributing insulator material and thus, restricting the locations where the electrical contact takes place[43]. Since the total number of electronic defects was reduced, the interface recombinative velocity will thusly be reduced, resulting in a positive impact on the solar cell performance. Additionally, the dielectric materials intended to be used as passivation layers, ideally possess a high density of fixed charges that create a built-in electric field into the semiconductor. This is commonly designated as field-effect passivation. This phenomena is beneficial since, with the correct polarity, such field will repel the minority carriers from the highly recombinative interface, hence reducing the effective recombination velocity and bolstering even further the passivating effect of this layer[43, 53, 87].

1.4 Light Management

Reducing the absorber thickness has additional detrimental effects on the solar cell. Due to several factors, a significant loss in short-circuit current occurs. The predominant factor is the incomplete optical absorption in the longer wavelengths of the incident spectrum [49, 88]. Additionally, the Mo rear contact possesses a high parasitic optical absorption, meaning that a significant percentage of photocurrent (I_{ph}) is lost due to the optical absorption occurring in the metal layer, instead of it taking place in the absorber [48, 54]. Replacing the Mo rear contact

with a conductor with more favorable optical properties is not a feasible option. Certain metals can outperform molybdenum in particular aspects, but no other metal is able to offer as a good balance in characteristics. Mo possesses good adhesion to the SLG substrate, high thermal stability, low electrical resistivity and high corrosion resistance against the Se present during CIGS deposition, forming a thin layer MoSe₂ that forms an ohmic contact with the absorber layer[13, 89]. Consequently, it is desirable that a solution is found that is capable of bolstering the optical absorption in the CIGS layer, by increasing the optical length of the incident photons in the absorber layer, and reducing the losses of the incident power absorbed in the molybdenum rear contact.

A solution was demonstrated in one of my earlier contributions, published by T. S. Lopes *et al.*[54], where it was proposed the placement of a thin layer of a highly reflective metal beneath the passivation layer, in order to increase the reflectivity of the rear contact. The consequences of the increase in reflectivity is the second chance given to the non-absorbed photons, to be absorbed in the CIGS layer when they are reflected back into it. In this manner, the photocurrent is compensated for the reduction created by issues above described. Furthermore, this structure has the benefit of potentiating other light trapping schemes due to the reduction in parasitic losses as it was mentioned in the references[74, 90]. Unfortunately, this architecture is not without its faults, and in the article in question, the shortcomings of the proposed architecture were demonstrated. Even though the majority of the metal mirror is slated between the molybdenum rear contact, and the dielectric layer, thus being mostly shielded during the remaining fabrication steps of the solar cell, the metal film is exposed in the contact zones as a consequence of the fabrication process, as shown in Figure 1.4.

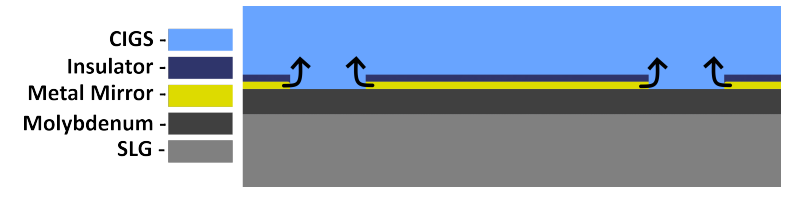


Figure 1.4: Locations where metal diffusion and selenium reaction occur during the CIGS fabrication process.

This small exposed section is enough for vile reactions to occur during the CIGS deposition step which resulted in degradation of the solar cell performance. Said reactions ranged from atomic diffusion of the metal elements into the absorber layer, which in turn negatively altered the properties of the CIGS film[19, 56], harmful reactions between the metal and the selenium atmosphere, to the complete detachment (peel-off) of the metal layer, which would in turn remove the layers situated above, from the substrate, thus destroying the entire solar cell[54]. Despite this, positive results were achieved on solar cells made with zinc and tungsten-titanium alloy back mirrors, as they proved to be quite resilient to high temperatures ($\approx 550~{\rm ^{\circ}C}$) and the harshness of the chemical atmosphere present during the fabrication step of the CIGS layer[68]. Additionally, they were capable of providing considerable gains in the performance of the solar cell. Nevertheless, as demonstrated in the article in question, other metals such as silver, should be used in order to fabricate back mirrors with higher reflectance, which creates the necessity for the development of a passivation/rear mirror structure that will not suffer from the same flaws, and can accommodate a much broader range of back mirror structures and materials.

Accounting for this issue, the design proposed in this thesis will have a buffer zone in the contacting area, where the metal layer will be subtracted, leaving sections containing only the dielectric material. This effort is made with the intention of eliminating any exposed metal and preventing the consequent reactions delineated above.

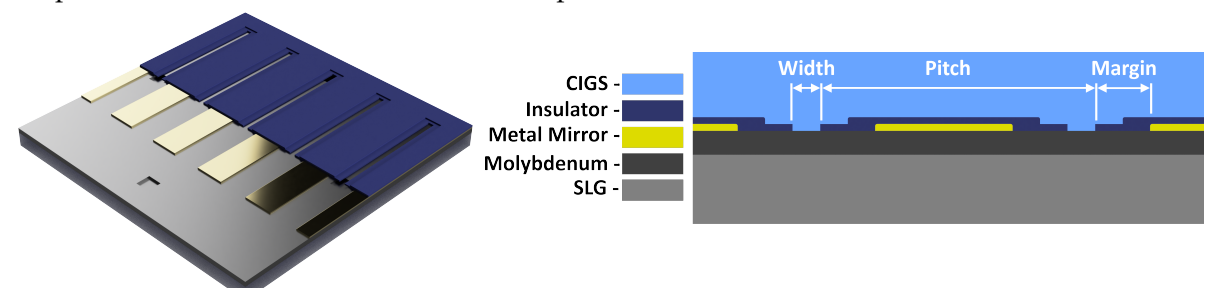
2 Materials and Methods

In the previous Introduction chapter it was set forth the motivation and reasoning behind the passivation layer and what it had to accomplish. The Materials and Methods segment will elaborate on the advanced fabrication process and characterization techniques necessary to fabricate and survey the desired structure. Furthermore, optical and electrical simulation studies were conducted with the intent of aiding the design process and the decisions involved, and to better understand the underlying effects that are responsible for the augmentation of the performance on passivated CIGS solar cells. Thus, a small description of those methods will be given.

2.1 Device Fabrication Process

The institution where this Thesis was developed in, the International Iberian Nanotechnology Laboratory (INL), does not have a CIGS TFSC production line, being the solar cell production delegated to our Swedish partners in Uppsala University. Instead, in this Thesis the focus is set on the rear contact and passivation structure that was previously described, with a complete overview of the CIGS fabrication process available elsewhere[68]. Previous iterations of my work, have their fabrication process described in detail in the following works by Bose *et al.*[53] and Lopes *et al.*[54], with a short description of each given in the Results Chapter. Therefore, only the most recent architecture will receive a detailed description of the fabrication process.

Before the description of the process begins, I draw the attention of the reader to Figure 2.1, where a cross-section and a 3D illustration of the Mo/CIGS interface passivated by the proposed structure are shown. The design can be summarized into a 2D layout, represented in Figure 2.1b that was extended throughout the entire length of the substrate. The design consists on the placement of the metal mirror segments on top of the molybdenum contact, followed by the encapsulation of the mentioned metal with an insulator, in order to physically shield the metal from the CIGS harsh growth conditions. The electrical contact is done in-between these passivation structures at specific intervals, allowing for an effective extraction of charge carriers. In Figure 2.1b, the dimensions designations are presented. The margin consists on the distance between the edge of the metal mirror and the insulator layer. The width is the distance between the edges of two insulator lines, and it is where the electrical contact occurs. Finally, the pitch is the distance between the same point of two different lines.



- (a) 3D Render of the passivation stack.
- (b) Cross-section of the passivation stack with CIGS.

Figure 2.1: Proposed passivation structure. Diagrams for illustrative purposes. Not at scale.

In order for the encapsulation of the metal mirror to occur, the width of the insulator segments need to be wider than the width of the metal mirror lines, otherwise, the pitfall of previous architectures will be repeated[54], and the exposed metal will deteriorate the solar cell performance, as it will be further developed in the Results Chapter below. The proposed design modification aims to solve the issues created by the exposed metal reflector, but with the repercussion being that, while in previous processes a single lithography step would suffice, that is not the case in this design. Due to the two different widths of the metal and insulator

patterns, and considering the fabrication equipment available at the INL cleanroom, this design requires two distinct lithographic processes. One to define the pattern of the metal mirror layer, and the second lithography to define the larger segments of the insulator layer. This, in turn, requires further modification to the existing processes. Since the rear reflector/passivation layer pattern transfer occurs in two steps, and due to the need to ensure the metal encapsulation, the two lithographies need to be well aligned with one another. To guarantee the correct pattern alignment, the lithography equipment requires the use of alignment markers, which in turn, need to be created in a third lithography step to ensure proper layer alignment.

The fabrication process starts in the Ångström Solar Center, where 5×5 cm² SLG substrates undergo the process of DC sputtering the Mo rear contact, in a MRC 603 sputtering system at 0.8 Pa and 1500 W, represented in Figure 2.2 with the a) step. When completed, the resulting Mo layer possesses a sheet resistance of $0.6\pm0.1~\Omega/\Box$ and a thickness of $350\pm20~\text{nm}$.

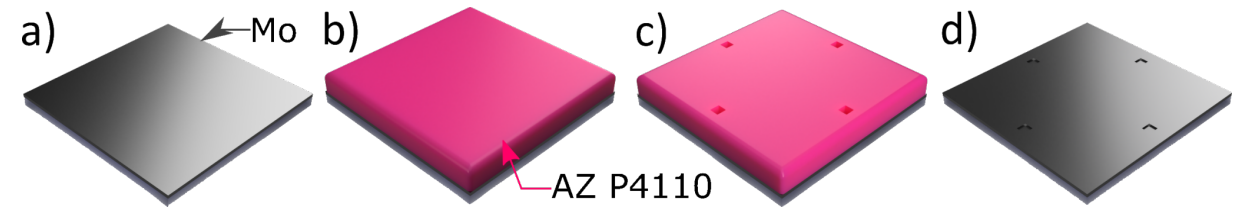


Figure 2.2: Schematic representing the alignment markers fabrication process. Not at scale.

2.1.1 Alignment Markers

On reception of the substrates at the INL facilities, they were submerged in an acetone ultrasound bath for 10 minutes, followed by a 10 minutes ultrasound bath in isopropanol, rinsed with deionised water and blown dry with nitrogen. The second major step involved the fabrication of the required alignment markers, represented in Figure 2.2 by the b), c) and d) steps. This fabrication stage started with a hexamethyldisilazane (HMDS; $C_6H_{19}NSi_2$) treatment applied to the substrates at 150°C, creating an adhesion promoter layer for the photoresist film. The latter being spin-coated onto the substrate, creating a 2.2 µm film of the positive optical photoresist (PR) AZ P4110 on top of the Mo layer. This step was achieved using a SUSS Microtec Gamma Cluster and a standard INL recipe. On completion, the PR coated substrates were exposed using direct laser optical lithography on a Heidelberg DWL 2000 equipment, with the laser operating at the 405 nm wavelength, and with standard exposure conditions at the time of the exposure. The marker lithography was executed in this equipment due to: i) it relinquishing the need of physical lithography masks, thus providing a greater process flexibility; ii) the chosen lithography system requires square markers with a 20 µm length, which is significantly above the 700 nm resolution limit of said equipment; iii) from initial sample loading to the removal of the exposed substrate, the exposure step can be done in approximately five minutes, making it one of the fastest lithography process available at INL. The PR development was executed in the Gamma Cluster, using AZ 400K:H₂O 1:4 developer for 300 seconds. The resulting exposed pattern conformity to the original design mask, was checked through an optical microscope. The substrates underwent the transfer of the markers pattern from the PR onto the Mo layer through reactive ion etching on a SPTS Inductively Coupled Plasma tool (ICP). The etching process needed to remove a minimum of 120 nm from the 350 nm layer of Mo, in order to attain a sufficient marker electronic contrast when said markers were analysed by the 100 kV electron beam lithography tool. Taking into account the Mo etch rate, the thermal limitations of the PR layers and the typical substrate temperatures during reactive ion etching, the 5 minutes long etching process was segmented into a set of smaller 30 and 60 seconds steps with the intent of minimizing the damage to the PR layer, so that it can be effectively stripped from the substrate. With the marker pattern transfer process complete, the remaining PR was removed by submerging the substrates for at least 20 minutes in an acetone ultrasound bath. Afterwards, the substrates were submitted to a 230 W O₂ plasma ashing step on a PVA TEPLA

Plasma Asher for 6 minutes. On completion, the samples were submitted to another 20 minutes acetone ultrasound bath, and a subsequent 5 minutes isopropanol ultrasound bath, rinsed with deionised water and blown dry with nitrogen.

2.1.2 Metal Mirror Layer

With the markers defined, the substrates went on to receive the metal back mirror, represented by the steps e), f), g) and h) in Figure 2.3.

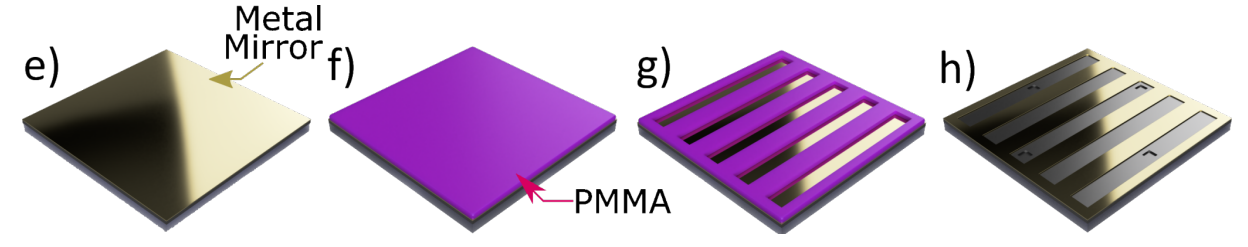


Figure 2.3: Schematic representing the fabrication process of the metal mirror layer. Not at scale.

The first task involved the selection of the metal for the back reflector function. Said decision was done in accordance to the following criteria: i) the metal had to possess a superior optical reflectance spectrum when compared to Mo; ii) the metal needed to be compatible with the fabrication process; and iii) it had to be available to be deposited at the INL cleanroom. In Figure 2.4 the reader can find the reflectance spectra[91, 92] of a few of the most relevant metal options, as well as the spectrum of the transmitted optical power through a 500 nm ultrathin CIGS solar cell, simulated by FDTD methods.

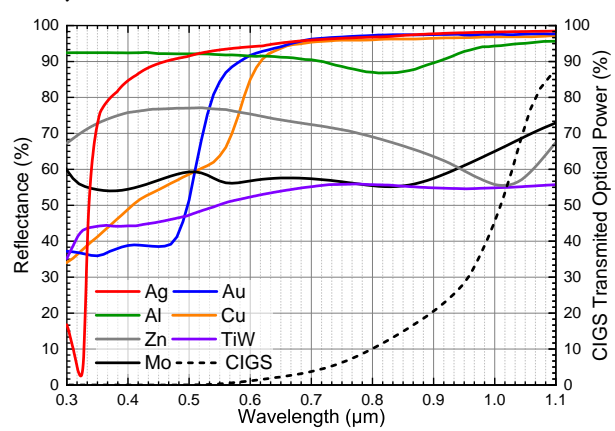


Figure 2.4: Reflectance spectra of possible metals to be employed as the back metal mirror [91].

Copper, silver and gold stand out, as their reflectance is above 95 %, between 0.7 µm and 1.1 µm wavelengths. This high reflectance value is highly desirable, as it is in the longer wavelengths, where the ultrathin CIGS suffers the most from incomplete optical absorption. Unfortunately, these metals are incompatible with the current fabrication process, due to material redeposition that occurs during the etch step in the ICP tool[93]. The next best option is aluminium, having a reflectance of 87 % and above throughout the entire relevant spectrum. More importantly, depending on the wavelength, aluminium has a 18 % to 38 % higher reflectance, in comparison to the molybdenum rear contact. In terms of compatibility with the fabrication process, aluminium does not have the same redeposition issues mentioned previously, nor does it have other relevant hindrances. Furthermore, when compared to Ag, Au and Cu, Al is more advantageous due to its lower price, increasing the feasibility of process's future scale-up. For these reasons, it was decided that aluminium, deposited by a Kenosistec multitarget UHV sputtering system, would be the constituting element of the rear reflector. In terms of the thickness value of the Al layer, the decision was influenced by the necessity to guarantee

the complete encapsulation of the reflector layer. Moreover, the lack of previous definitive conclusions related to the conformability of the insulator deposited on top, and especially, on the side walls of the metal layer, influenced the decision. Thus, a consensus was formed around the 10 nm value for the thickness of the Al layer for the initial fabrication run, as this value is half of the thickness of the insulator layer, thus reducing the chance of encapsulation failure. After the quality of the encapsulation was established in the initial fabrication run, the metal mirror thickness was increased to 25 nm, for additional optical gains. As it will be shown in the Optical Simulations Results section, a 10 nm thick metal reflector still provides significant aid to the CIGS optical reabsorption.

With the metal mirror deposited, the process advanced into the second lithography step, accomplished in the Vistec EBPG 5200 electron beam lithography system, due to its superior alignment and resolution capabilities, when compared with the optical Heidelberg DWL 2000 system[94, 95]. A 430 nm layer of undiluted Polymethyl methacrylate (PMMA; $(C_5O_2H_8)_n$), an electron sensible positive resist, was spun on top of the metal mirror and baked at 150 °C for one minute, with the aid of the SUSS Microtec Gamma Cluster track. Before the exposure, the samples were placed inside the loading chamber of the electron beam lithography system for approximately eight hours, in order to reach thermal equilibrium with the system and eliminate alignment errors caused by the thermal expansion of the glass substrate. The exposure occurred at a beam acceleration voltage of 100 kV, and at a beam current of 100 nA. The pattern consisted on array of lines with a width varying from 0.7 μ m to 1.2 μ m, depending on the sample, a pitch of 2 μ m and a length of 4 cm. A representation of the exposed pattern can be found in Figure 2.3 g). After the, up to, 25 hours long exposure, the exposed PMMA was submitted to the development process, which again was executed in the Gamma Cluster. The development process lasted 40 seconds, using a Methyl isobutyl ketone based developing solution.

After the development, line shaped sections of the metal mirror were exposed, in the locations where the electrical contact with the rear electrode will be made. This meant that the exposed metal could now be selectively removed, and this step was achieved with the second ICP etch of the fabrication process, this time lasting for 20 seconds. The process to strip the remaining PMMA was the same described for the stripping of the AZP 4110 in the marker fabrication segment.

2.1.3 Insulator Layer

With the metal mirror layer fabricated, the process advanced into the passivation layer assembly stage, depicted in Figure 2.5 by the steps i), j) k) and l).

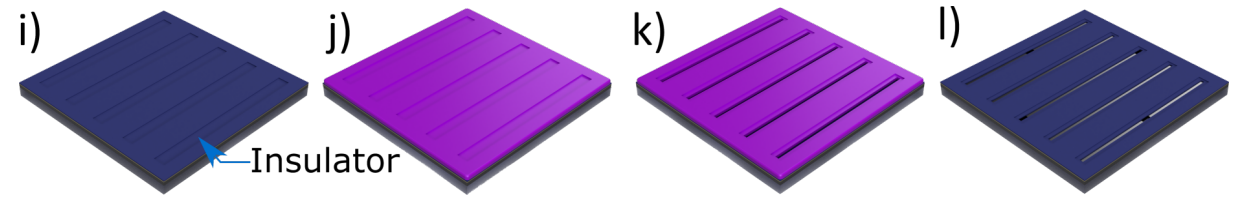


Figure 2.5: Schematic representing the fabrication process of the insulator layer. Not at scale.

The insulator selection process had two points in common with the metal selection: i) the chosen insulator had to be compatible with the fabrication process; ii) and it had to be available at the INL facilities, since it was an intermediate step of the fabrication process. Moreover, the insulator had to fulfill two additional requirements: iii) it needed to be capable of withstanding the high temperatures of the CIGS deposition process (≈ 550 °C)[50, 68]; iv) the insulator had to exhibit both good chemical, and field-effect passivation capabilities, in order to maximize the solar cell performance. From the available material pool, only two insulator materials fulfilled the specifications, SiO_x and Al₂O₃. While Al₂O₃ has seen wide usage as the rear passivation layer in CIGS[48, 50, 54, 85], in this process, the selected insulator was SiO_x, with it holding a proven track record as a passivation layer as well[53, 85, 87]. The main factor that lead to

the choice of SiO_x as the insulator material in this fabrication process, was the quality of the deposited films of both the SiO_x and Al_2O_3 materials, at the INL facilities. From previous experience and unpublished data, the RF sputtered Al_2O_3 in a Timaris FTM tool, has proven to have a lower quality consistency in terms of the passivation layer performance, when compared to the SiO_x deposited by Plasma Enhanced Chemical Vapor Deposition (PECVD) in a *SPTS* MPX CVD tool. With the insulator selection process complete, the substrates underwent the deposition of 20 nm of SiO_x by PECVD at 300 °C on a *SPTS* MPX CVD, as it is represented in the step i) of the Figure 2.5.

As preparation for the third lithography step, the substrate was spin-coated with 430 nm of PMMA, with the same conditions as described previously. After, the sample was loaded into the Vistec EBPG 5200 e-beam lithography tool, and a thermalisation interval occurred. The aligned exposure consisted on the same line pattern with the same length and pitch, but with a width 0.5 μ m smaller, meaning that the pattern had a 0.25 μ m margin on each side, i.e. if the first e-beam exposure consisted of lines with a width of 0.66 μ m, in the second e-beam exposure, the line width would be 0.16 μ m. The beam acceleration voltage remained at 100kV, but the beam current was reduced from 100 nA to 70 nA, as the μ C dosage was lower. Afterwards, the substrate was again developed for 40 seconds with a Methyl isobutyl ketone based developer in the Gamma Cluster.

The third and last etching step, with the intent of removing the excess SiO_x and creating the contact openings to the Mo rear electrode, was again executed in the *SPTS* ICP tool. The conditions were the same as the previous etch steps, but the duration was adjusted to 30 seconds, in order to account for the thickness and etch rate of the SiO_x layer. After performing the strip of the remaining PMMA through the use of acetone and the plasma asher as previously described, the fabrication process was complete.

2.2 Characterization

Throughout the several stages of the various fabrication processes that lead to complete CIGS solar cells, careful examination of the samples was required, in order to accurately assess the resulting quality of each process.

2.2.1 Sample Analysis

During the interim steps of the previously described fabrication phase, the quality of the alignment markers, and the status of the sample's overall cleanliness after each resist strip step, was obtained through a Nikon Eclipse L200N 100x optical microscope. After the completion of the fabrication of the passivation structure, the samples were taken into a NovaNanoSEM 650 Scanning Electron Microscope (SEM), operating at 5 kV, for surface analysis. Through this data, it was possible do determine the accuracy of the alignment, and the likelihood of the metal layer encapsulation having been successful or not.

Post CIGS solar cell fabrication, multiple solar cell cross sections where analyzed through a Transmission Electron Microscopy (TEM) FEI Titan Themis operated at 200 kV. The extracted data allows the determination of the level of success of the fabrication stage, by the analysis of the subsequent structure. Additionally, elemental analysis through Scanning Transmission Electron Microscopy (STEM) Energy Dispersive X-ray Spectroscopy (EDS) was performed, in order to ascertain the status of the back reflector and passivation layer, and to determine if the encapsulation was successful.

2.2.2 Solar Cell Electrical Characterization

The completed CIGS solar cells were subjected to current density-voltage (J-V) measurements, in order to ascertain the electrical performance gains of the solar cells that received the encapsulated back structure. These results were then compared to reference solar cells, produced in the same run of the Ångström Solar Center pilot line, at Uppsala University. The J-V measurements were accomplished through the use of a modular system developed at the Ångström

Solar Center, with a tungsten halogen lamp outputting an optical power density calibrated to 1 kW/m², and a voltage sweep from -0.5 V to 1 V in 5 mV steps. External quantum efficiency (EQE) measurements accompanied the J-V results, being the data extracted from representative cells of each fabricated substrate. During the EQE measurements, the sample was illuminated with monochromatic light ranging between the 330 nm wavelength and 1000 nm, in 2 nm steps.

2.2.3 Architecture Simulation

Accompanying the fabrication of the solar cell substrates, extensive optical and electrical simulations were performed, intended at providing both a better understanding of the underlying effects, and allow for the optimization of the proposed design, with the intent of maximizing the solar cell performance.

The optical simulations were performed using the commercial software solution *Lumerical* Finite-Difference Time-Domain (FDTD) solver[96]. Said software is capable of resolving the Maxwell's equations in complex 3D geometries by decomposing said structures into a discrete spatial and temporal grid. Some of the solved equations, but not limited to, are the following[96–98]:

$$\frac{\partial \overrightarrow{D}}{\partial t} = \nabla \times \overrightarrow{H} \tag{2.1}$$

$$\overrightarrow{D}(\omega) = \varepsilon_0 \varepsilon_r(\omega) \overrightarrow{E}(\omega)$$
 (2.2)

$$\frac{\partial \overrightarrow{H}}{\partial t} = -\frac{1}{u_0} \nabla \times \overrightarrow{E} \tag{2.3}$$

These are the Maxwell's curl equations solved in non-magnetic materials, where \overrightarrow{H} , \overrightarrow{E} and \overrightarrow{D} are the magnetic, electric and displacement fields respectively. The complex relative permittivity, or dielectric constant, is represented by $\varepsilon_r(\omega) = n^2$, where n is the material refractive index. Additionally, μ_0 is the permeability of free space and ε_0 is the permittivity of free space. ω and t represent angular frequency and time, respectively[97–99]. Further details of the FDTD simulations will be provided in the optical simulation results section.

The electrical simulations were executed using the *Lumerical* CHARGE software, a 3D charge transport simulator capable of solving the Poisson's electrostatic potential equations and the drift-diffusion equations [100, 101]:

$$J_n = q u_e n E + q D_n \nabla_n \tag{2.4}$$

$$J_p = qu_h pE - qD_p \nabla_p \tag{2.5}$$

where J is the current density, μ_h and μ_e are the hole and electron mobility respectively, n stands for the concentration of free electrons while p represents the concentration of free hole carriers. The electron elementary charge is represented by q, while D_p and D_n stand for the diffusion coefficient of holes and electrons, respectively.

In order to solve the drift-diffusion equations (2.4;2.5), it is necessary to know the electric field, which can be determined by solving the following equation [100, 101]:

$$-\nabla \cdot (\varepsilon_r \nabla V) = q\rho \tag{2.6}$$

where V is the electrostatic potential, and ρ is the net charge density. In order to account for the charge conservation, the auxiliary continuity equations are required [100, 101]:

$$\frac{\partial n}{\partial t} = \frac{1}{q} \nabla \cdot \mathbf{J}_n - R_n \tag{2.7}$$

$$\frac{\partial p}{\partial t} = -\frac{1}{a} \nabla \cdot \mathbf{J}_p - R_p \tag{2.8}$$

where R_n and R_p are the net recombination rate of electrons and holes, i.e. the difference between the recombination rate and generation rate of each carrier.

3 Results and Discussion

The research and development of microfabrication processes is highly iterative in nature, meaning that current efforts are based in the findings and conclusions of previous versions of the work in question, with the intent of further improving the previous result. This thesis is no exception, and in order to validate the hypothesis that served as the cornerstones of this thesis, the main outcomes of previous iterations will be presented, works in which I partook in [53, 54]. Subsequently, the results of the optical and electrical simulations of the current and previous designs versions will be presented, in order to provide a direct comparison between the presented architectures and to allow for further study of the current proposed design. Ultimately, the results of the characterization of the fabricated substrates will be shown, as well as the results corresponding to the analysis of the complete solar cells.

3.1 Previous Results

Before advancing into the latest results, the outcome of my precedent works relevant to this thesis, will be presented. For the sake of brevity, an abridged version will be showcased.

3.1.1 Insulator Passivation Layer

The first results pertain to the article "Optical Lithography Patterning of SiO₂ Layers for Interface Passivation of Thin Film Solar Cells" [53] published by Bose *et al.* The aim of this article was to study the impact of a passivation structure fabricated through optical lithography on a ultra thin CIGS solar cell. For such, a 25 nm thick layer of SiO₂, positioned on top of the Mo rear contact, was fabricated with a stripped pattern. In addition, the dimensions of the pattern were varied in order to study the relation of the distance between electrical contacts and the efficacy of the charge carrier extraction. A schematic representing the fabricated structures is found in Figure 3.1. Furthermore, the article showcased the capabilities of SiO₂ as a passivation material for CIGS solar cells.

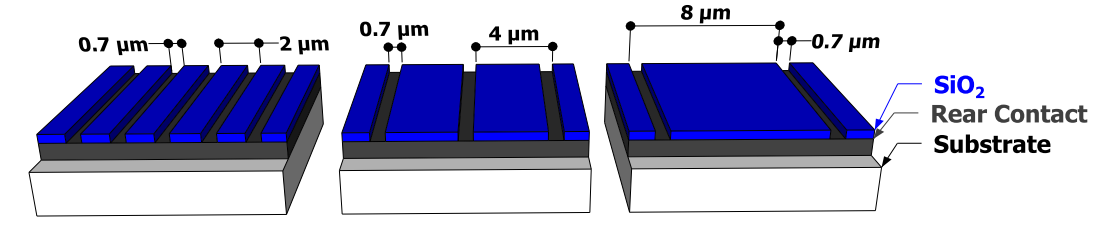


Figure 3.1: Schematic representing some of the fabricated structures. Adapted from [53].

The fabricated substrates underwent the processing required for the fabrication of a complete solar cell at imec[53, 102]. The solar cells had a similar structure as described previously, that is: $SLG/Mo/SiO_2/CIGS/CdS/i-ZnO/Zno:Al/Ni-Al-Ni$ grid, with the CIGS layer being coevaporated at 550 °C and with a final thickness of 450 nm. The elemental composition of the CIGS layer was measured by X-ray fluorescence and was determined to be the following: $\frac{[Cu]}{[Ga]+[In]}=0.7$ and $\frac{[Ga]}{[Ga]+[In]}=0.3$. Reference substrates possessed, apart from the passivation layer, the same cell structure, elemental composition, and were processed in the same batch.

The resulting solar cells underwent J-V and EQE characterization, in order to measure the impact of the passivation structures and the different distances between electrical contacts. Representative plots of the results can be found in Figure 3.2, and the averaged values of the J-V figures of merits can be found in the Table 3.1

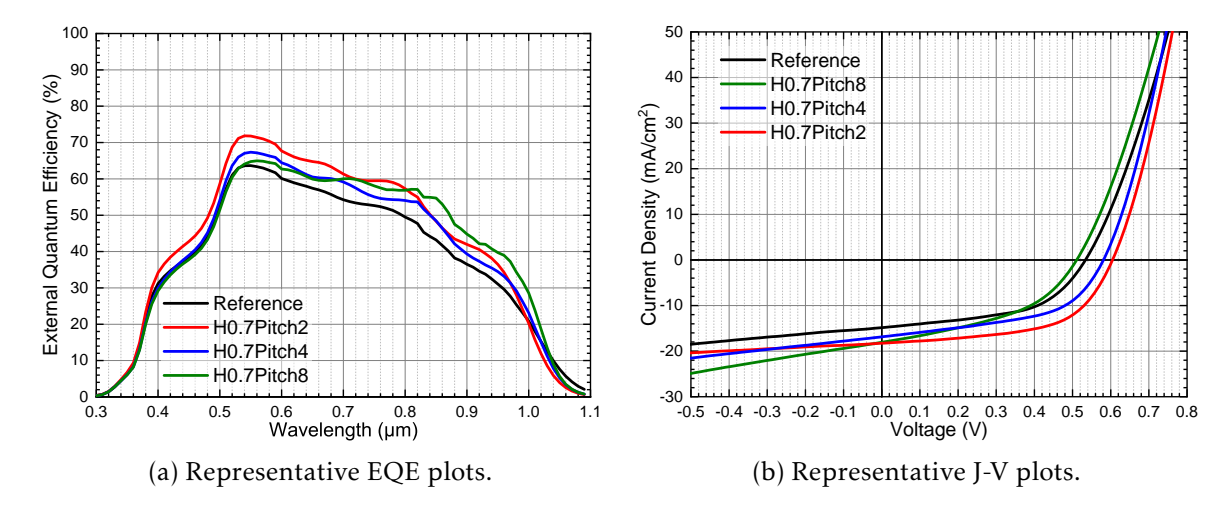


Figure 3.2: Results from J-V and EQE measurements of reference and passivated solar cells.

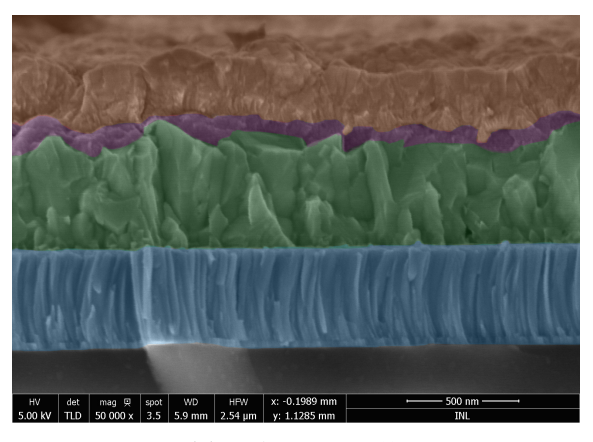
Table 3.1: Average and standard deviation values of each passivation pattern.

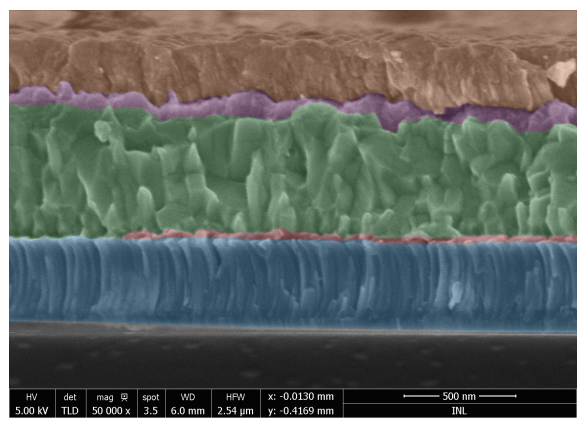
Sample	Line Width (µm)	Pitch (µm)	Passivation Area (%)	J _{SC} (mA/cm ²)	V _{OC} (mV)	FF (%)	η (%)
Reference	No passivation layer			16.60 ± 0.94	536±16	55.2±3.4	4.9 ± 0.6
H0.7Pitch2	0.7	2	65.0	18.22 ± 0.31	607±5	52.2±8.9	5.8 ± 1.0
H0.7Pitch4	0.7	4	82.5	16.96±0.39	580±1	59.3 ± 4.2	5.8 ± 0.5
H0.7Pitch8	0.7	8	91.3	17.72±1.09	518±16	46.3 ± 6.1	4.3 ± 0.8

The EQE measurements, displayed in Figure 3.2a, demonstrate the optical enhancements induced by the passivation layer, such as it was hypothesised in previous chapters. All the passivated samples demonstrated a superior external quantum efficiency in comparison with the reference cell. Such EQE increase is then translated in a consequent augmented J_{SC} in all the passivated solar cells.

When analysing the J-V data in Figure 3.2b and the Table 3.1, a distinct behaviour is observed with the samples H0.7Pitch2 and H0.7Pitch4. These two samples possess the hallmark effects of rear interface passivation. They present an increase in the V_{OC} , an increased J_{SC} and similar values of FF, when compared to the reference solar cell[43, 50, 103]. These gains are translated into a final gain in efficiency up to 18 %, relative to the reference non-passivated solar cell. The hypothesis that SiO₂ can be utilized as the constituent material of passivation layers is thus confirmed. Additionally, the beneficial effects of a passivation layer are demonstrated as well. On the contrary, the sample H0.7Pitch8 displayed an efficiency loss, even though it possesses the highest passivation area. Despite of the H0.7Pitch8 sample having the highest average J_{SC}, both the FF and the V_{OC} were the lowest. The reduced fill-factor indicates insufficiencies in charge extraction. This deficiency might be attributed to the high contact resistance caused by the hole accumulation in the rear interface, and the increase of the current density in the contacts, due to the high passivation area [104]. Furthermore, the literature indicates that passivation structures should be designed taking into account the minority carrier diffusion length in order to be effective [43, 50, 75]. The minority carrier diffusion length is known to typically be between 0.75 μ m and 2 μ m[50, 105, 106], however, the 8 μ m pitch of the H0.7Pitch8 sample is higher than the double of the 2 µm maximum of the diffusion length interval, possibly leading to ineffective charge carrier extraction. This sample showcases the consequences of a poorly designed passivation architecture.

In addition to the electrical studies, SEM analysis was performed on the cross section of a reference and a passivated solar cell. The intent was to determine the state of the passivation layer after it being exposed to the harsh conditions of the CIGS deposition. Furthermore, the study allowed to verify the morphological influence of the passivation layer on the CIGS absorber. The processed pseudo-color SEM images can be found in Figure 3.3:





(a) Reference Cell.

(b) Passivated Cell.

Figure 3.3: Pseudo-color SEM cross sections of a reference and passivated solar cell. The Mo rear contact is colored in blue, the SiO_2 in red, CIGS in green, CdS in purple and the ZnO/Zno:Al window layer in orange. The passivated solar cell has a insulator pitch of 8 μ m.

Figure 3.3b indicates that the SiO_2 passivation layer is capable of withstanding the harsh CIGS deposition environment, and does not present adhesion issues. The CIGS absorber layer does not exhibit observable divergences in its morphology, indicating that the passivation layer does not precipitate undesirable changes to the CIGS structure [107].

3.1.2 Metal back reflector

With the impact of passivation structures in ultrathin CIGS solar cells demonstrated, the focus was set on the optical phenomena that were the subject of the article "Rear Optical Reflection and Passivation using a Nanopatterned Metal/Dielectric Structure in Thin-Film Solar Cells"[54] by Lopes *et al.* In the mentioned article, it was demonstrated that the current losses due to insufficient optical absorption of the CIGS layer could be reduced by depositing a layer of a highly reflective metal, in between the insulator passivation layer and the Mo rear contact. For a more extensive description of this concept, the reader may refer to the "Light Management" subsection of the introduction chapter of this thesis.

In Figure 3.4 the reader can find a schematic of the metal reflector and passivation layer structure proposed by the article in question.

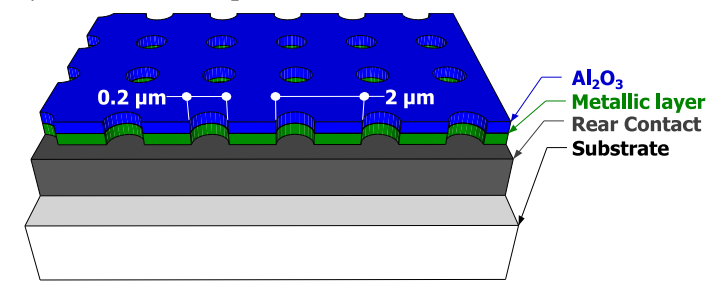


Figure 3.4: Schematic representing the fabricated structures. Adapted from [54].

In comparison to the structure from the article by Bose *et al.*[53], the structure in Figure 3.4 consists of a dotted pattern, with the same dimensions used throughout all the fabricated samples. The electrical contact diameter is 0.2 μ m and the pitch between the same point of the electrical contacts is 2 μ m. These dimensions result in a passivation area of 96.86 %. In this work, the insulator material chosen for the passivation layer was Al₂O₃, a material widely used as a passivation layer for CIGS[52, 54, 85, 108, 109]. The variable distinguishing the samples was the material used as the rear reflector layer. A total of eight metals and metal alloys were used, namely: Ag, Au, AlSiCu (98.34 % Al; 1.45 % Si; 0.21% Cu), Cu, Ta, Ti, TiW (97.19 % Ti; 2.81 % W) and Zn.

The fabricated substrates underwent the CIGS deposition process in the Ångström Solar Center pilot line, at Uppsala University[68]. The 500 nm thick CIGS layer deposition occurred at 520 °C and the measured compositional values were $\frac{[Cu]}{[Ga]+[In]}$ =0.85 and $\frac{[Ga]}{[Ga]+[In]}$ =0.28.

The completed solar cells were submitted to J-V and EQE characterization, for the sake of determining the repercussion of the metal reflector and the insulator passivation layer, on the performance of the solar cell. In Figure 3.5, the reader finds the J-V and EQE curves of the highest efficiency device, of representative samples. The average values of the J-V analysis are in Table 3.2. It is noteworthy that, as previously mentioned, some of the data published in the article in question, was omitted from the following charts and table for the sake of density. Nevertheless, the conclusions remain unaltered, and the complete data can be found in the annexes.

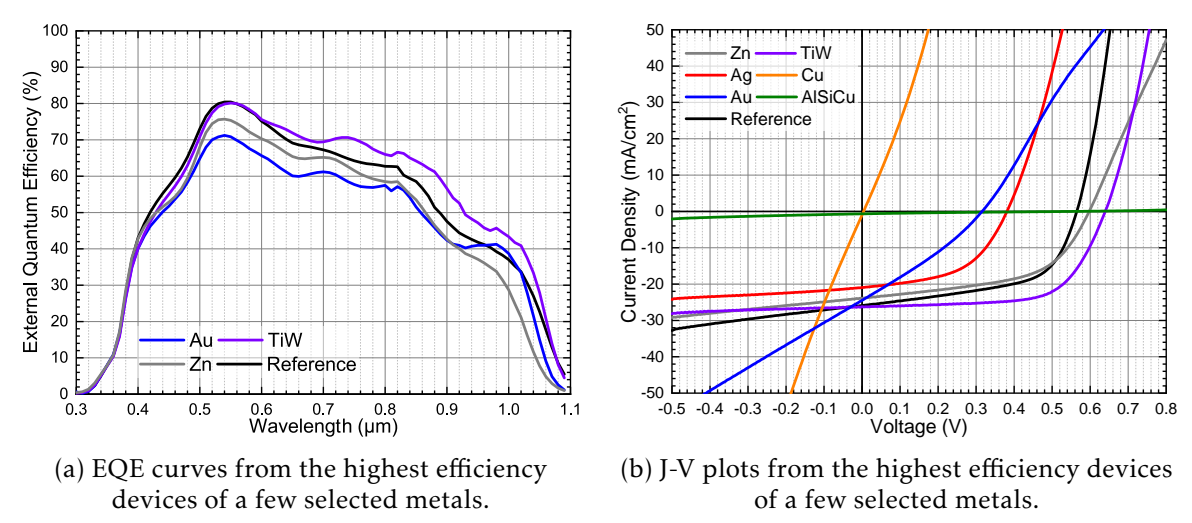


Figure 3.5: Results from J-V and EQE measurements of reference and passivation/reflector samples.

Table 3.2: Average and standard deviation values of each sample with different metals as back reflector.

Sample	J_{SC} (mA/cm ²)	V _{OC} (mV)	FF (%)	η (%)
Reference	24.28±0.39	535±14	47.5±4.6	6.2±0.9
Ag	15.43 ± 3.02	365±13	49.9 ± 2.2	2.8 ± 0.7
Au	22.19±1.61	191±77	26.1 ± 1.4	1.2 ± 0.6
AlSiCu	0.47 ± 0.11	404 ± 66	21.6±1.2	0.0 ± 0.0
Cu	1.34 ± 0.30	2±1	0.0 ± 0.0	0.0 ± 0.0
TiW	25.25 ± 0.81	629±6	61.9 ± 4.5	9.9 ± 1.0
Zn	23.63±1.59	590±8	51.1±2.5	7.1 ± 0.5

From the six samples incorporating a metal or metal alloy back reflector, all but two samples suffered from degraded performance. The proposed failure mechanisms are varied, ranging from rampant metal selenization, unrestrained inter-elemental diffusion from the metal reflector layer into the CIGS[110], to the formation of current blocking compounds[111]. The physical disengagement of the Mo and CIGS layer due to the expansion of the selenized metal layers was also experienced, resulting in the destruction of the entire solar cell.

The two samples that demonstrated an augmented performance were the TiW and Zn samples, but were still short of reaching the full potential of this solar cell architecture. The Zn sample displayed a decrease in the short circuit current density, possibly due to the formation of a n-type ZnSe compound[111]. Additionally, the efficiency increase of the Zn sample is attributed to the open-circuit voltage and fill factor gains caused by the insulator passivation layer.

Even though all the previous samples demonstrated nefarious reactions during the CIGS fabrication step, the TiW sample did not display any negative conditions. It boasted an increase in J_{SC} , V_{OC} and FF, resulting in a 3.7 % absolute efficiency increase, in comparison to the reference solar cell. The only shortcoming burdening this sample, is the fact that the TiW alloy possesses an optical reflection similar to the one of Mo, as demonstrated in Figure 2.4. The similarity in the optical performance of the TiW and Mo materials, means that the demonstrated gains are largely responsibility of the dielectric passivation layer, thus the resulting improvements are not due to superior optical performance but are, instead, electrical in nature. In conclusion, this work demonstrates the consequences of having an exposed rear reflector layer during the CIGS deposition phase. Even though only a small percentage of the total area of the metallic layer was exposed, this segment located in the electrical contact points, proved to be the main vulnerability of this architecture. If highly reflective metals, such as Ag, Al, Au or Cu are to be used, in order to achieve greater current densities, it is imperative that the reflective layer is shielded from exposure to the harsh conditions of the CIGS deposition process.

3.2 Optical Simulations

The usefulness of optical simulations is twofold. Not only do they allow for a better understanding of the optical phenomena that occur inside the structure of a ultrathin CIGS solar cell, but they also allow for the optimization of the design parameters, in order to maximize the performance of the solar cell design in study. These optical simulations where performed using Finite-difference time-domain methods and small portion of the developed workflow will be showcased. The optical models were based on the refractive index, n, and extinction coefficient, k, of each material obtained from several sources. The i:ZnO, Al:ZnO and CdS data was obtained from Carron's et al. work[112], the passivation/back mirror bilayer materials data, Al and SiO_x , was obtained from Palik's publications[91] and the Mo rear contact material data was acquired from Werner's et al. article[113]. Finishing the optical material model, the CIGS index values were determined in-house, through spectroscopy ellipsometry measurements[74]. In terms of layer thickness, unless specified otherwise, the values used were 400 nm of the Al:ZnO layer, 100 nm for the i:ZnO layer, 50 nm for the CdS buffer, 500 nm for the CIGS absorber layer and 350 nm for the Mo rear contact. The passivation layer and metal mirror thickness were dependent on the architecture in question. For the encapsulation architecture developed in this thesis, the simulations were ran with 25 nm for the Al layer, and 20 nm for the SiO_x , while for the previous iterations, the dimensions are according to the values reported in the correspondent articles.

At the start of each simulation, a pulse of a laterally-uniform electromagnetic wave with a wavelength ranging between 0.3 μ m and 1.1 μ m is perpendicularly projected towards the the structure surface. On reaching the structure, the incident light is reflected, transmitted, and absorbed, with the amount depending on the properties of the material in question. In order to properly simulate a solar cell, all three effects need to be known, but the absorption has an added importance, since it is the absorption of the incident radiation that will cause the generation of the photocurrent, due to the photovoltaic effect[114]. Thus, in order to determine the absorbed optical power, P_{abs} , the resulting electric field distribution in each spacial unit cell is measured and the absorbed optical power calculated through the following equation[115–117]:

$$P_{abs} = \frac{1}{2}\omega |E|^2 \operatorname{Im}(\varepsilon_r)$$
(3.1)

with ω representing the angular frequency of the incident spectrum, $|E|^2$ representing the strength of the electric field and ε_r the dielectric permittivity. Integrating P_{abs} over the volume gives the total optical absorption, Abs, at a specific wavelength (λ) for the entire solar cell structure:

$$Abs(\lambda) = \int P_{abs}(\lambda)dV \tag{3.2}$$

Now that the absorption per wavelength is known throughout the solar cell structure, the number of charge carriers generated in the absorber layer can be calculated using the following equation:

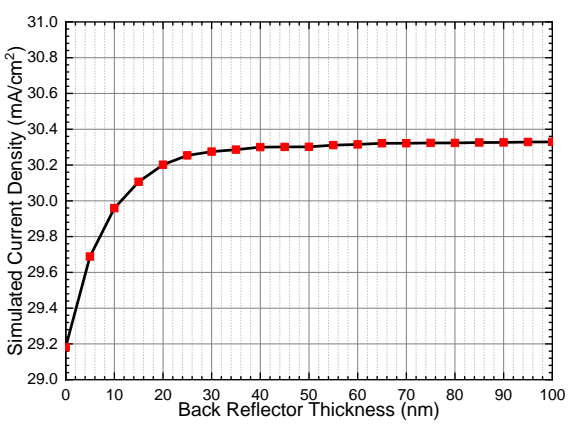
$$G = \int \frac{\lambda}{hc} Abs(\lambda) I_{AM1.5G}(\lambda) d\lambda$$
 (3.3)

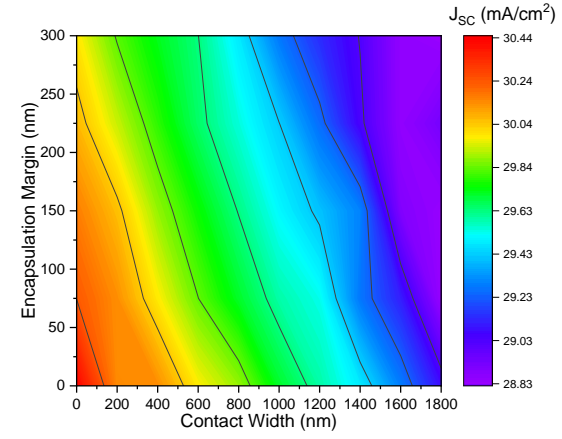
Of the variables shown above that are yet to be introduced, $I_{AM1.5G}$ stands for the standard global terrestrial solar spectrum with 1.5 for air mass, h and c are Planck's constant and the speed of light in vacuum, respectively. With the carrier generation rate and total absorbed power known, the EQE and J_{SC} can be calculated as well. The EQE is attained by calculating the ratio between the total absorbed optical power in the CIGS layer and the optical source power. The J_{SC} is attained by multiplying the generation rate calculated throughout the entire absorber layer, by the elementary electronic charge[118]: $J_{SC} = qG$. This approach will return the maximum theoretical value for the short circuit current of the solar cell. This is due to the fact that the FDTD method does not take into account any charge transport phenomena, meaning that this short circuit current value is reached assuming that every single generated charge carrier is successfully extracted.

3.2.1 Optical Simulations Results

Before drawing comparisons between the different discussed architectures, the simulations performed with the intent of optimizing the proposed encapsulating architecture will be shown. In said optimization runs, there were three main points of contention that required a more indepth study, in order to understand their impact on the solar cell performance. Specifically: i) the thickness of the metal back reflector; ii) the rear contact width and iii) the encapsulation margin. In order to study point i) and understand the impact of the metal reflector thickness on the J_{SC} , a set of simulations were set, wherein an Al layer with 100 % surface coverage was placed on top of the Mo rear contact, followed by a 20 nm layer of SiO_x located above the metal reflector layer. Even though it is not feasible, from an electrical standpoint, to have the rear contact completely covered in an oxide layer, this was done with the intention of determining the maximum optical impact of the passivation/metal reflector bilayer. Consecutively, the thickness of the Al film was varied between 0 and 100 nm in 5 nm steps, with the resulting data plotted in Figure 3.6a. The results show that for each 5 nm increase in the Al layer thickness, the current gains per step diminish. At the 25 nm mark, the Al layer boosts the current in $\approx 1.07 \text{ mA/cm}^2$, while at the 100 nm Al thickness, the current gain reaches its highest value at $\approx 1.15 \text{ mA/cm}^2$. A difference of 0.08 mA/cm² at the cost of 75 nm of additional Al. Thus, the 25 nm thickness value appears to be the optimal target for the Al rear reflector, since thicknesses beyond this value provide meager returns at the cost of extra material usage, longer deposition times and coverage issues during the CIGS deposition step might arise for the larger thicknesses. For the optimization of the contact width and encapsulation margin, simulations were ran wherein these two values were varied independently of one another. Between 0 and 1800 nm for the contact width, with 200 nm steps, and 0 and 300 nm for the encapsulation margin with 50 nm steps. This meant that surface coverage ratios between 0% and 100% were simulated. Thusly, the J_{SC} impact of the back mirror/passivation bilayer for a variety of combinations was simulated and the result is plotted in Figure 3.6b.

The goal of the dimensional optimization run, was to determine what is the response of the photogenerated current when the dimensions of the rear structure are altered, and if there is a point of diminishing returns, as it was observed in the Al thickness simulation run. The resulting data indicates that the relation between the J_{SC} and the two dimensions in question, the contact width and encapsulation margin, is roughly linear. Furthermore, the data indicates that an equal dimensional variation between the contact width and encapsulation margin will not yield the same impact in the photocurrent. The highest impact is caused by shifts in the contact width value. This is expected since variations in the contact width will reduce the overall area covered by both the metal back reflector and the passivation layer, thus increasing





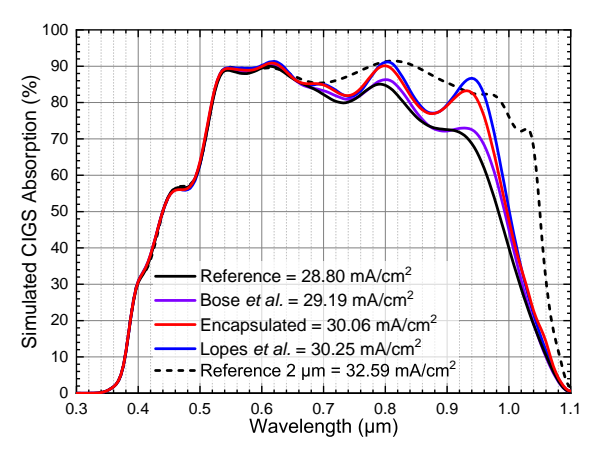
- (a) Short circuit current gains in relation to back reflector thickness.
- (b) Relation between the encapsulation margin, contact width and solar cell photogenerated current.

Figure 3.6: Results from the design parameters optimization simulations.

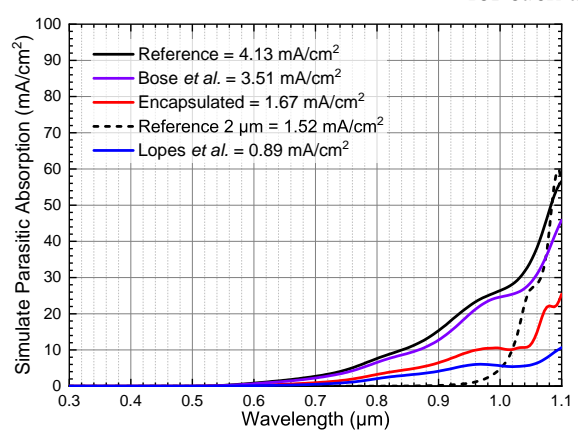
the exposed area of the optically inferior Mo rear contact. Secondly, the impact caused by the variation of the encapsulation margin is lower since this change will only affect the metal back reflector. The width of the insulator film will remain the same, which, even though not as effective as the metal back mirror, still provides significant optical gains. In conclusion, from an optical standpoint, the contact width and encapsulation margin should be as low as the fabrication process can handle, in order to maximize the photocurrent gains.

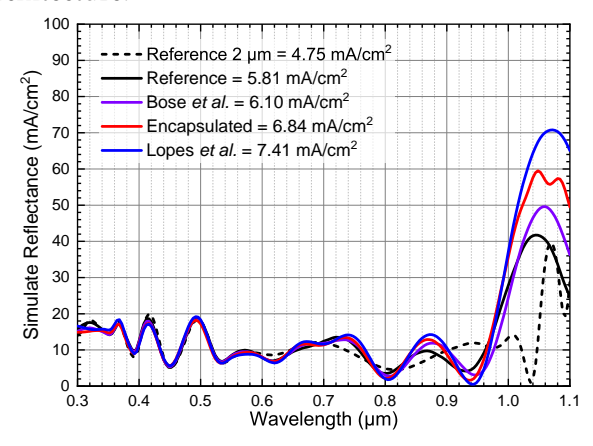
With the encapsulation design optimized, optical simulations were performed with the intent of comparing the current encapsulation design with a reference and previous design iterations of rear contact passivation and optical enhancing structures. The simulations in question provide three major datasets: i) the total CIGS absorption and J_{SC} in Figure 3.7a; ii) the J_{SC} loss due to the substrate parasitic absorption in Figure 3.7b; and iii) the J_{SC} deficit caused by the total reflection of each solar cell design in Figure 3.7c. For the encapsulation design, a contact width of 160 nm and an encapsulation margin of 200 nm were used, as these values are representative of the developed fabrication process. Secondly, an ultrathin 500 nm CIGS reference solar cell and a 2 µm standard thickness CIGS solar cell were simulated, in order to provide context for the performance of ultrathin CIGS solar cells. Since this thesis focuses on ultrathin CIGS solar cells, all further comparisons will be made against the ultrathin 500 nm CIGS solar cell, designated as "Reference".

In terms of the optical performance of the encapsulated substrate, it is expected that the CIGS optical absorption and I_{SC} performance gains are situated between the performance of the structures previously developed in Bose et al. and Lopes et al. articles [53, 54]. When comparing the encapsulation design with the initial iteration of a passivation layer revealed in Bose et al., the expected result is that the encapsulation architecture outperforms its older counterpart, due to the presence of an optically enhancing metallic back mirror. The simulations confirm this claim, since while the passivation structure achieves a 0.39 mA/cm² increase over the reference, the encapsulated design reaches an increase of 1.26 mA/cm² above the reference. On the other hand, when the encapsulation design is compared to the design proposed in Lopes et al., it shows slightly worse performance in terms of current gain. This is expected, since even though the materials and thicknesses are similar between the simulations of the two designs, the layout showcased in Lopes et al. possesses a 97 % coverage of the rear contact surface area. On the other hand, due to the necessity of encapsulating the metal and due to the margins necessitated by the fabrication constraints, the simulated encapsulated design retains 72 % of its surface area occupied by the metal reflector and 92 % covered by the insulator. Nonetheless, the 25 % reduction in metal surface area resulted in a smaller drop in the current gains. While the



(a) Simulated CIGS absorption spectra and J_{SC} for each architecture.





- (b) Simulated parasitic optical absorption spectra of the rear passivation and contact layers.
- (c) Simulated total solar cell reflection spectra.

Figure 3.7: Optical performance of the several iterations of rear contact passivation and optically enhancing layers.

Lopes *et al.* structure achieved a J_{SC} improvement of 1.45 mA/cm², the encapsulation structure achieved an increase of 1.26 mA/cm², a delta of 13 % in the current gains, for a loss of 25 % of metal coverage.

The plot in Figure 3.7b shows the current lost to the parasitic optical absorption of the structures below the CIGS absorber, namely the parasitic absorption of the Mo rear contact and, when present, of the passivation/metallic mirror layers. All three designs show a reduction in the parasitic current loss, meaning that a higher percentage of the unabsorbed radiation is redirected back into the CIGS ultrathin layer, as intended. Furthermore, the behaviour of the parasitic absorption of the substrate in the various simulated designs follow the same trends that are displayed in the CIGS absorption plot. As previously, the performance of the encapsulation design sits in-between the mirrorless Bose's et al. passivation structure and the design shown in Lopes's et al. article. Albeit, even though the encapsulated design shows a reduction in the parasitic current loss of 2.46 mA/cm², the solar cell's J_{SC} gains are merely 1.26 mA/cm². This disparity in the currents is explained by the solar cell's total reflectance plot in Figure 3.7c. The data charted in this plot is the spectral distribution of the total reflected light from each of the solar cell designs, in addition to the lost J_{SC} value by each of the reflection spectra. In order to increase the performance of a solar cell, the solar cell's reflectance has to be suppressed to the lowest value possible, since reflected optical power cannot be converted into photocurrent. Paradoxically, all three passivation designs demonstrate reflections higher than the reference configuration, with the trends seen in the previous graphs remaining true. The passivation

layer shown in Bose's *et al.* article, has an increase over the reference of 0.29 mA/cm^2 , followed by the encapsulation structure with an increase of 1.03 mA/cm^2 of the photocurrent loss to reflection, and with the highest value of 1.60 mA/cm^2 attributed to the design presented in Lopes *et al.* Even though these results might appear as a negative aspect of the rear passivation structures, it has to be mentioned that this phenomena is in reality, an opportunity to further increase the optical performance of CIGS ultrathin solar cells. The simulated designs have no other light trapping scheme present, meaning that the increase in reflection is due to the light that was reflected back into the CIGS from the rear contact structures, but was not completely absorbed. Thus, these structures can enhance the efficacy of other light trapping mechanism, such as nanoparticles or anti-reflection layers, with this synergy resulting in a higher J_{SC} , compared to what would be achieved by the individual use of the mentioned light trapping scheme. Simulations where ran, where the encapsulated rear reflector was accompanied by nanoparticles at the rear interface and an anti-reflection layer in the Al:ZnO front contact. The resulting data can be seen in Figure A.2 located in FDTD Simulations Supplementary Data.

In the preceding chapters, it was mentioned that in ultrathin CIGS, the importance of the rear contact passivation is emphasised, due to a higher percentage of the photogenerated charge carriers being located in close proximity to the highly recombinative rear interface [47, 48]. Substantiating this, is the data plotted in Figure 3.8, which represents the simulated photocurrent generated throughout each nanometer of the height of the CIGS absorber, for 500 nm and 2 µm references and a encapsulated design.

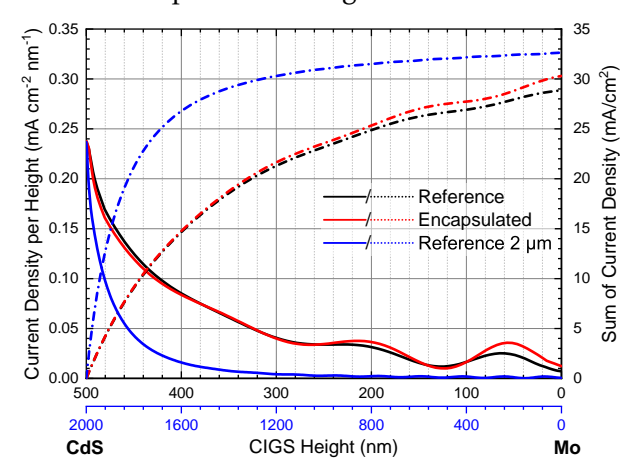


Figure 3.8: Current density generated throughout the height of the CIGS layer. Zero starts at the passivation layer/Mo rear contact and the height goes up to the CdS interface. The data pertaining to the 2 μ m reference is compressed horizontally, with its independent axis colored in blue. The two vertical axis apply to both independent X axis.

If taken into consideration the contribution of the last 100 nm of the CIGS film for all three samples, the previous claim becomes apparent. In the ultrathin reference and in the encapsulated solar cells, the CIGS between 100 nm and 0 nm contributes approximately 14.2 % and 16.6 % to the total J_{SC} value, respectively. On the other hand, the same region in the 2 μ m standard thickness reference cell only contributes 0.6 % to the total photogenerated current. When the rear interface is optically enhanced, as it happens to be in the encapsulated structure, as seen in Figure 3.8, the current gains are located in close proximity to the rear interface, further increasing the importance of the rear passivation. In addition, the plotted data shows that for the 2 μ m standard thickness reference cell, a large percentage of the volume of the absorber layer barely contributes to the overall J_{SC} value. However, on the ultrathin cells, the photocurrent generation is more evenly distributed throughout the height of the absorber layer. This increased spacial efficiency is an additional argument in favor of the development of ultrathin CIGS solar cells.

The data plotted in Figure 3.8 reveals the dependence of the height of the CIGS and the

current generation occurred in the absorber. However, no information is provided regarding the relation between the height of the generation event and the incident wavelength that induced it. The relevancy of this information pertains to the future employment of further light-trapping and optically enhancing structures, such as nanoparticles[74] or Voronoi nanocavity arrays[73]. The relationship between the wavelength of the incident light, the height at the CIGS layer and the consequent generation rate was attained and is plotted in Figure A.1, found in the FDTD Simulations Supplementary Data appendix.

3.3 Electrical Simulations

Optical simulations provide a wealth of information about the solar cell structures developed for rear passivation and light management. However, during the FDTD simulations the charge transport mechanics are completely disregarded, meaning that the results provided by the simulations are only valid in an theoretical setting, where the charge extraction ratio is one. Furthermore, no data is provided in relation to the solar cell's V_{OC} , FF, power conversion efficiency and other electrical figures of merit. Therefore, the information that can be gathered through the optical simulations, about the performance of the various passivation layer designs and their effect on the solar cell is limited to a certain extent.

In order to accurately simulate the repercussions of the several passivation layer schemes previously shown, the physics-based electrical simulation software *Lumerical CHARGE* was used to perform 3D electrical simulations of ultrathin CIGS solar cells. For such, the existence of a suitable ultrathin CIGS electrical model was required, which after an extensive literary review culminated in the model data found in the Table B.1 located in the Appendix B, where further details about the electrical model are given. Besides the bulk properties of each of the material layers composing a CIGS solar cell, the developed model accounts for the CIGS/CdS, CIGS/MoSe₂ and CIGS/SiO_x interface surface recombination velocities (SRV_n/SRV_p) for both carriers independently. The field effect passivation created by fixed charges in the SiO_x layer is accounted for as well. Since CHARGE is a 3D solver, it inherently accounts for the geometrical dependence of the various phenomena that occur during the photovoltaic operation of a solar cell. For instance, the three dimensional distribution of the generated charge carriers imported from the FDTD optical solver, the effectiveness of the passivation layer and its dependence on the percentage of surface coverage. Furthermore the impact of the geometric features of the device is accounted for in the charge transport mechanics.

3.3.1 Electrical Simulations Results

Keeping with the encapsulation design optimization process, electrical simulations were performed with the intent of determining the influence of the rear contact width on the solar cell's figures of merit. To that end, the passivation area was varied between 0% and 99%, with no other design variables being altered. The resulting efficiency and Fill Factor can be found plotted in Figure 3.9.

The results suggest that the contact width should be as small as the fabrication process allows, and that the increase in efficiency and fill factor will be approximately linear, akin to the conclusions provided by the optical simulations. However, the charted data indicates that there is no performance drawback as the passivation area approaches 99 % of the total contact area, a result which goes against what is reported in the literature[43, 85, 108]. The reason behind this discrepancy of the current version of the CIGS electrical model can be attributed to two factors: i) *CHARGE* considers metals, such as the Mo rear contact, as perfect electrical conductors with an infinite conductance and a flawless interface with the semiconductor layers; ii) the developed model is isothermal, meaning that the *CHARGE* solver completely disregards any thermal influences in the charge transport mechanics.

Simulated J-V measurements were performed on the reference and in the encapsulated design, so that the impacts of the passivation layer on the solar cell's performance can be known. Three dimensional maps containing the spacial distribution of the generated carriers,

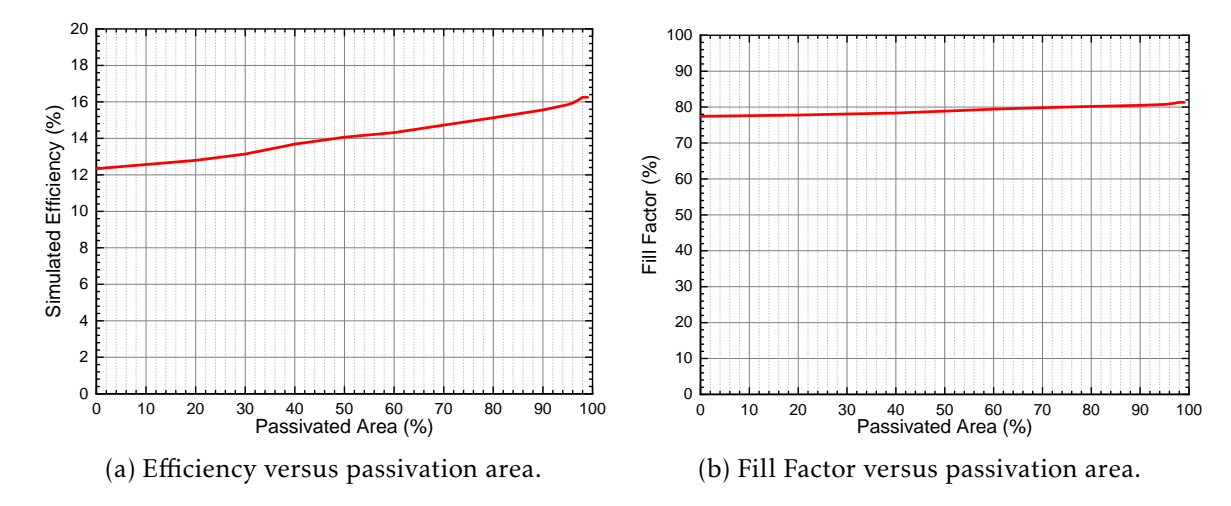


Figure 3.9: Simulated power conversion efficiency and Fill Factor depending on the total rear contact passivated area.

calculated through the FDTD optical simulations were imported into the respective model and the voltage was swept from 0 V to 0.78 V in 20 mV steps. Even though a 20 mV stepping will return coarser results, compared to the 5 mV stepping used in the experimental J-V analysis, it was found that the 20 mV value provided a good compromise between accuracy and the required computational resources. The encapsulated design model possessed a 160 nm contact width and an encapsulation margin of 200 nm. The resulting J-V curves can be found in Figure 3.10 and the figures of merit in Table 3.3.

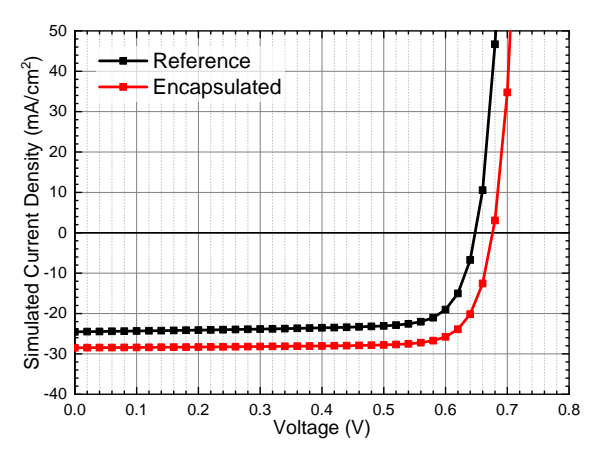


Figure 3.10: Simulated J-V plots of the reference and encapsulated designs.

Table 3.3: Simulated figures of merit of the reference and encapsulated designs.

Sample	J_{SC} (mA/cm ²)	V_{OC} (mV)	FF (%)	η (%)
Reference	24.53	649	77.4	12.3
Encapsulated	28.48	677	80.4	15.5

The encapsulated cell demonstrates increases throughout all the figures of merit, when compared against the reference. The J_{SC} displays an increase of 3.95 mA/cm², by virtue of the increased reflectivity of the rear contact and the reduced recombination. This reduction in the rear interface recombination leads to an augment in the V_{OC} , with it showing a gain of 28 mV over the reference. These J_{SC} and V_{OC} improvements coupled with a 3% increase of the Fill Factor in favor of the encapsulated cell, result in an absolute efficiency gain of 3.2% over the reference.

It was previously claimed that in ultrathin CIGS solar cells, the detrimental effects of rear

interface recombination become more pronounced, thus, the passivation of said interface is essential in order to achieve high efficiency ultrathin solar cells. In addition, it was demonstrated through optical simulations in Figure 3.8 and Figure A.1, that the optical gains generated by the back mirror layer are predominantly located near the rear contact interface. However, at an electrical level, the relationship between the spatial location of the generated charge carriers and the charge extraction efficacy has not been demonstrated. CHARGE does not possess any built-in function to extract a solar cell's EQE, thus an indirect approach had to be developed. The link between the FDTD optical simulations and the CHARGE electrical simulations is a three dimensional map with the distribution of the generated charge carriers. Taking advantage of this feature, the 3D charge distribution map was divided into singular wavelengths, rather than having a single 3D map containing the generation distribution for the whole spectrum. Afterwards, electrical simulations were ran in a short circuit condition per each of the wavelengths, and by comparing the currents obtained through the FDTD optical solver and the CHARGE electrical solver, the influence of the charge transport mechanics can be determined. Said effects are manifested in a ratio between the FDTD J_{SC} and the CHARGE J_{SC} at a specific wavelength, with the ratio being the effectiveness of the extraction of the generated charge carriers. Accordingly, if the solar cell's EQE calculated through FDTD, is multiplied by said extraction ratio, the electrically aware EQE plot of the solar cell can be plotted. This approach was applied to a reference and to a encapsulated solar cell design, with the resulting EQEs and extraction rations plotted in Figure 3.11:

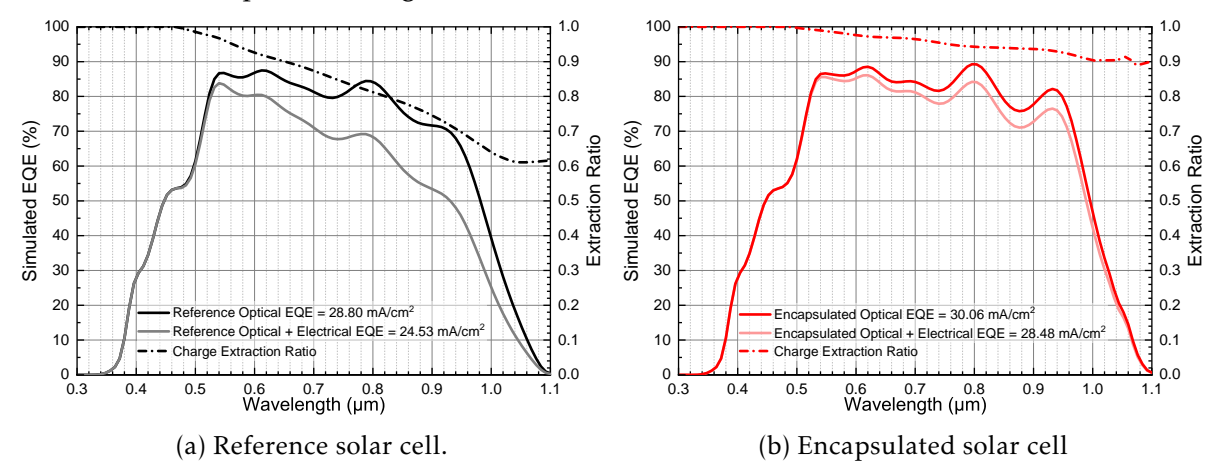


Figure 3.11: Simulated EQE with and without charge transport mechanics of passivated and reference solar cells. The charge carrier extraction ratio per wavelength is shown with the respective axis on the right side.

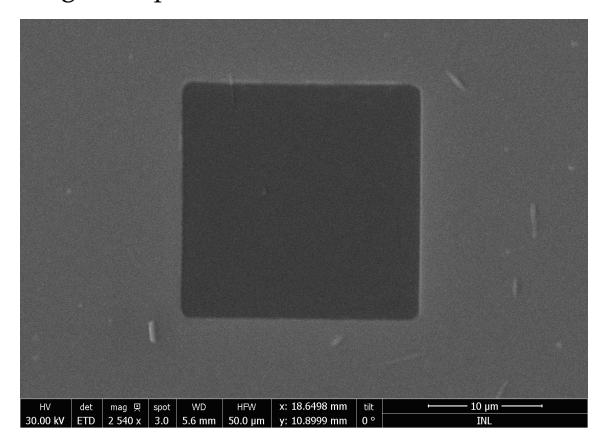
The effectiveness of the passivation layer can be seen by comparing the extraction ratio of the reference cell in Figure 3.11a with the extraction ratio of the passivated solar cell in Figure 3.11b. For the reference, on wavelengths above 0.47 μ m the extraction ratio starts declining, reaching a minimum of 0.61 at the 1.05 μ m wavelength. This leads to a 4.27 mA/cm² reduction of the J_{SC} from the ideal 28.80 mA/cm² to a J_{SC} of 24.53 mA/cm² when the charge transport mechanics are accounted for. In the encapsulated cell, the effectiveness of the passivation layer is demonstrated by the much higher extraction ratio that this design presents. The encapsulated design extraction ratio begins its decline at the 0.50 μ m wavelength, reaching the 0.88 minimum at the 1.08 μ m wavelength, 0.27 higher than the reference's minimum value. The higher extraction ratio throughout the whole spectrum leads to a much smaller reduction of the J_{SC} , dropping the J_{SC} by 1.58 mA/cm², from the ideal 30.06 mA/cm² to 28.48 mA/cm², when the charge transport is no longer ideal. Since it is known, through the optical simulations, that the photogeneration gains provided by the rear reflector are situated closer to the CIGS/Mo interface, these extraction ratios reinforce the benefit and importance of the rear passivation layer. A literary search failed to return simulation results similar to the ones presented by

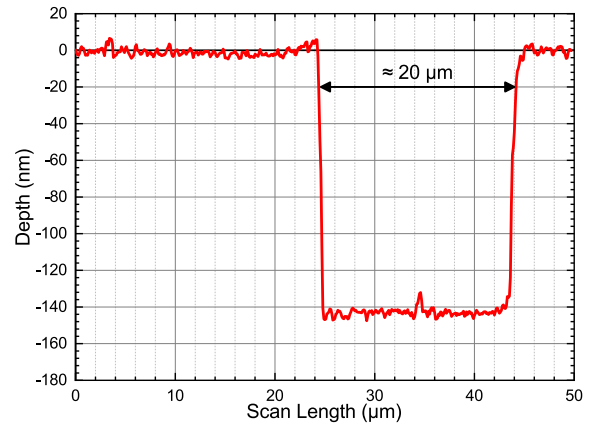
this innovative technique, with the most similar being the ones originated through empirical experiment with e-beam induced current[105, 106, 111].

3.4 Substrate Fabrication & Cell Results

Due to external factors reducing the manufacturing capacity of both the installations at INL and Ångström Solar Center, a reduced number of substrates was fabricated, and only a singular substrate was processed into a complete ultrathin CIGS solar cell. Nevertheless, in conjunction with the substrates fabricated during the development of the fabrication process itself, there is enough data to fully characterize the outcome.

The first characterization step during the fabrication process pertains to the quality of the lithography alignment markers. Even though the 20 μ m width of the markers is well inside the capabilities of the optical lithography equipment, due to the need to maximize the fabrication area in each of the substrates, they are placed as close to the substrate border as possible. On the other hand, due to the square geometry of the substrates, the photoresist deposition is highly uneven near the edges, circumstance worsened by the need to use a 2 μ m thick resist due to the prolonged etching period. Notwithstanding, the process was successfully optimized and the resulting alignment markers were inspected through SEM and their depth was measured at approximately 140 nm, with the aid of a profilometer. The resulting SEM image and profilometer data can be found in Figure 3.12:





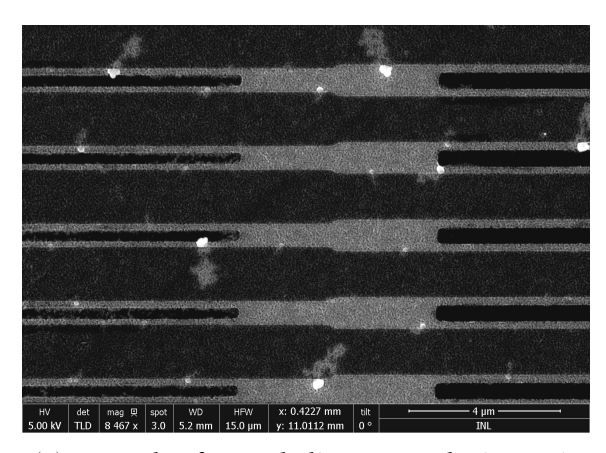
(a) SEM image of a complete alignment marker.

(b) Profile and depth of an etched marker into the Mo layer.

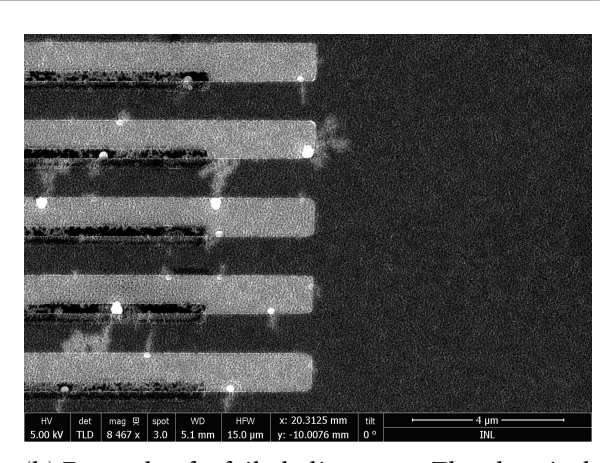
Figure 3.12: Topographical analysis of a lithography marker by a profilometer and SEM.

Despite the use of alignment markers, the alignment success was not guaranteed. The ebeam lithography tool was set to recalibrate the alignment at ten minutes intervals. However, since the exposures could be as long as twenty five hours, there could be hundreds of recalibrations during an exposure, hundreds of opportunities for the alignment to fail. Furthermore, the error margins were very narrow, since the contact lines ran through several centimeters of the substrate, thus, an angle of 1 degree of alignment error was enough for the encapsulation to be compromised. Several measures were put in place to reduce the frequency and the severity of these errors, such as the compartmentalization of the design, or the fabrication of a much higher number of markers than what was necessary. Be that as it may, on completion of the fabrication process, it was necessary to check the quality of the lithographic alignment and the general state of the sample's condition. For such end, the substrates were analysed through SEM, in the interest of determining the quality of the finished pattern. In Figure 3.13, the reader can find SEM images exemplifying both a successful and a failed lithographic alignment.

The substrates that passed through the quality control were shipped to Ångström Solar Center, so that the remainder of the CIGS solar cell fabrication process could be executed. At Uppsala, a modified version of the CIGS fabrication process, as described in the Introduction, was executed. During the Cu-rich deposition phase, a portion of the Cu was substituted for Ag



(a) Example of a good alignment. The image is of a test substrate, thus, two different contact sizes are shown.

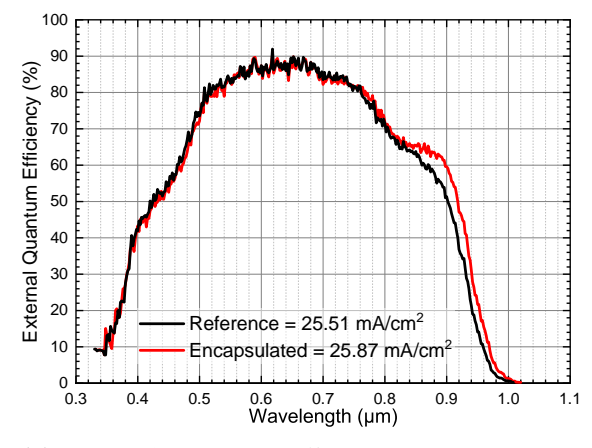


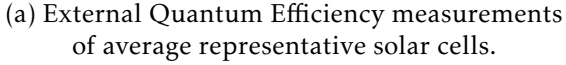
(b) Example of a failed alignment. The electrical contact was etched between the insulator and metal back reflector, exposing the latter.

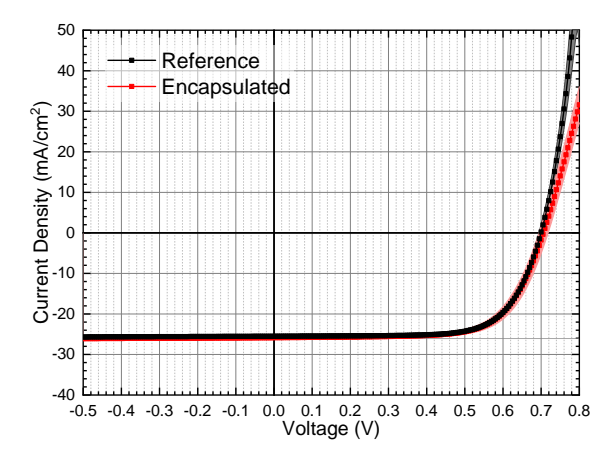
Figure 3.13: SEM images showcasing an example for both a successful and failed lithographic alignment.

with a ratio of $\frac{[Ag]}{[Ag]+[Cu]}$ =0.10, resulting in the formation of (Ag,Cu)(In,Ga)Se₂. This substitution results in a increased V_{OC} , consequence of the elimination of the negative conduction band offset in the CdS/CIGS interface[119, 120]. The CIGS deposition process resulted in a film with an approximate thickness of 610 nm with the composition ratios of $\frac{[Cu]}{[Ga]+[In]}$ =0.8 and $\frac{[Ga]}{[Ga]+[In]}$ =0.42. The buffer layer was deposited to a thickness of 50 nm through chemical bath deposition, followed by the 170 nm thick i:ZnO/Al:ZnO window layer acting as the top contact, since no Ni/Al/Ni grid was deposited.

Solar cell's figures of merit were extracted from the light J-V measurements. Said J-V measurements and the EQE results were performed as previously described. The resulting data can be found plotted in Figure 3.14 for the EQE data and J-V curves, and in Table 3.4 the J-V figures of merit. Each substrate sample contained sixteen 0.1 cm² solar cells, thus, for the encapsulated cell the presented data pertains to the average of said sixteen solar cells. However, for the reference sample, the population size is fifteen, due to the removal of a significantly lower performing outlier solar cell.







(b) Averaged illuminated J-V curve. The curve's shadow is the standard deviation.

Figure 3.14: Electrical measurements of reference and encapsulated architecture solar cells.

The EQE curves shown in Figure 3.14a provide information concerning the optical aspect of the rear passivation and back mirror structures fabricated on the substrate. Even though optical gains are found in the encapsulated sample, they fall short of the gains predicted by the

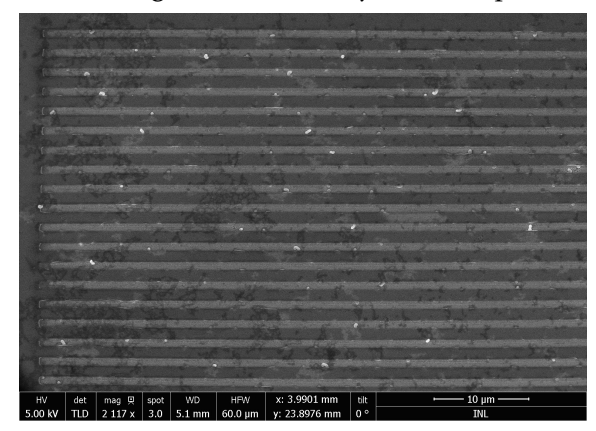
optical simulations, with a J_{SC} increase of 0.36 mA/cm², when the simulations anticipated a 1.26 mA/cm² difference. The J-V curve in Figure 3.14b returns similar results, with the encapsulated cell demonstrating an insignificant 6 mV V_{OC} gain over the reference cell, contradicting the expected V_{OC} increment provided by the passivation layer, as suggested by the electrical simulations.

Table 3.4: Average ar	ıd standard	deviation	values	of the J-V	figures of merit.
				, .	0

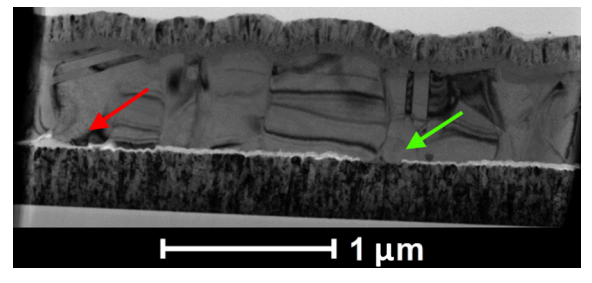
Device		J_{SC} (mA/cm ²)	V _{OC} (mV)	FF (%)	η (%)	G_{SH} (mS/cm ²)	$G_S (mS/cm^2)$
Reference	Best cell	25.90	700	71.1	12.9	0.37	541
Reference	Mean	25.51±0.29	700±6	70.5 ± 1.3	12.6 ± 0.3	0.35 ± 0.07	497±50
Encapsulated	Best Cell	26.41	718	70.6	13.4	0.45	371
	Mean	25.87 ± 0.31	706±12	69.3±1.0	12.7 ± 0.5	$0.45 {\pm} 0.07$	345 ± 34

Even though the J_{SC} and V_{OC} had minor improvements, the Fill Factor of the encapsulated cell suffered a 1.2 % drop over the reference, consequence of the significantly worse shunt conductance (G_{SH}) and series conductance (G_{S}). The lower series conductance for the encapsulated cell on its own is not unexpected, since it is a known result of a passivation layer that could be further optimized. However, the higher shunt conductance goes against the expected results. The insulator layer of the passivation layer should have reduced the shunt conductance, since it acts as a barrier to possible shunt paths. As a result of these figures of merit, the encapsulated solar cells showed a 0.1 % absolute efficiency increase over the reference, with the highest performance encapsulated solar cell being 0.5 % over the best reference cell.

While the exact reasons for the lackluster performance increase of the encapsulated solar cells are not yet known, a few influencing factors will be discussed. Before the CIGS deposition, the substrate in question was analysed by SEM, in order to check not only the alignment, but also the overall quality of the substrate. Succeeding the solar cell fabrication, the sample was examined again, this time by TEM. Representative images can be found in Figure 3.15:



(a) SEM image of the complete substrate before CIGS deposition.



(b) Bright field TEM image of a cross section of the complete CIGS encapsulated solar cell. The red arrow shows an unopened contact, while the green arrow shows an open contact.

Figure 3.15: Electronic microscopy analysis of the substrate before and after the CIGS deposition process.

In Figure 3.15a, it is visible through the SEM image that various residues are present in the surface of the encapsulation structure. The debris consist of scorched PMMA leftover after the ICP etching steps. Various attempts to remove the burned resist were made, from prolonged ultrasounds bath in acetone, isopropyl alcohol and resist strippers such as Microstrip 3001, to oxygen plasma ashing but none succeeded in completely cleaning the substrate. Furthermore, due to the very strict timetable, the substrate was sent in this state, so that solar cells could be manufactured, with the intent of repeating the process after the resist issues were solved.

Promising results are being attained by shifting the conditions of the etching step, namely by utilizing a process with active substrate cooling in a *SPTS Advanced Plasma System*.

After the completion of the solar cell fabrication process, bright field TEM analysis was performed on a cross section of the solar cell, in order to analyse the state of it after it underwent the harsh CIGS deposition process. In Figure 3.15b, an example of a detected defect is found, designated by the red arrow, where the SiO_x layer should have been etched through in order to create the electrical contact. The etch did not occur, thus preventing the local charge collection. Additionally, the sporadic presence of significant sidewalls near the electrical contacts was detected, which can negatively affect the contact quality if severe enough. In order to determine the state of the 10 nm thick Al back mirror layer, and check if the elemental diffusion from the back mirror was prevented, STEM energy dispersive X-ray spectroscopy (EDS) was performed on the cross sections of the complete solar cell. The resulting images with the elemental composition distribution can be found in Figure 3.16:

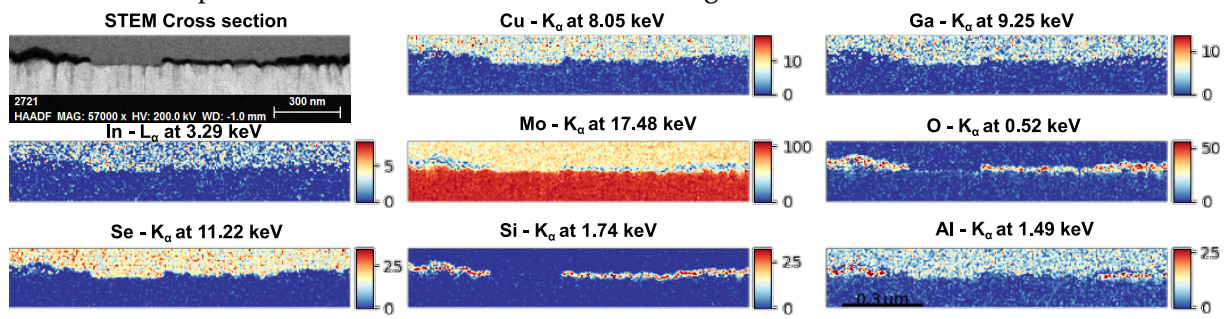


Figure 3.16: Elemental composition distribution of an encapsulated rear passivated CIGS solar cell's cross section.

Through the comparison between the Si and Al elemental distribution, the quality of the alignment between the lithographies can clearly be seen. In this sample, the alignment was heavily biased to the left side, but it was still inside the safety margin and the SiO_x layer overlaid the Al back mirror. The oxygen distribution presents some cues for the lackluster J_{SC} gains provided by the Al back mirror. To facilitate the reader's visualization, the aluminium elemental distribution was overlayed over the oxygen distribution, in Figure 3.16:

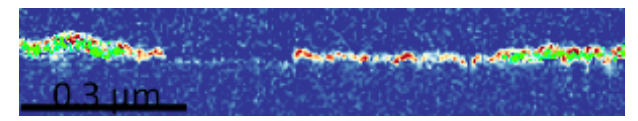


Figure 3.17: Aluminium elemental distribution in green, overlayed over the oxygen elemental distribution.

By comparing the elemental distribution of aluminium and oxygen, it can be concluded that amidst the fabrication process of the CIGS solar cell, the Al back reflector was oxidized and Al_2O_3 was formed. This is heavily detrimental for the back reflector since Al_2O_3 is essentially transparent and provides a much reduced optical gain, resulting in a decrease from 30.06 mA/cm² to 29.53 mA/cm² in optical simulations. The suspected sources for the aluminium oxidation are: i) the SiO_x deposition process, as it occurs in an N_2O atmosphere at high temperatures, thus it is possible that a reaction between the oxygen and aluminium occurs at that stage; ii) the O_2 plasma ashing cleaning steps between the lithographies; iii) the formation of native Al_2O_3 during the substrate handling before the Al layer is encapsulated by the SiO_x , as the substrate is exposed to the atmosphere. To overcome this issue, an oxide layer could be deposited on top of the Al layer, immediately after the deposition of the metal. The oxide deposition needs to occur inside the same machine that deposited the Al, thus avoiding exposing the aluminium to the atmosphere, through the creation of a semi-encapsulating oxide layer. An alternative is the use of a low temperature SiO_x deposition method, assuming that the reduced temperature results in a reduced aluminium oxidation rate.

4 | Conclusion and Future Perspectives

As the cornerstone of this thesis, I delved into the potential of CIGS ultrathin solar cells and what role they can play in the future's energy supply. However, said future will not materialize unless some critical hurdles are overcome, such as the price per kWp or the the volatility of the In supply. A solution to tackle both these issues is the deployment of sub-micrometer CIGS solar cells, known as ultrathin. This contraction allows for the reduction of the material cost, the dependence on the In supply and increases the manufacturing output, resulting in a reduction of the kWp price. However, this material reduction is not without its faults, as it will lower the CIGS optical absorption, and make it more susceptible to rear interface recombination. Nevertheless, these deficiencies can be remedied, as the rear recombination can be repressed by the use of a dielectric passivation layer, and the optical absorption losses can be restored through the placement of a highly reflective metal layer. It was in these two key points that my preliminary work focused on, yet, further improvements were necessary. Accordingly, I set out with the intent of researching and developing an approach to successfully combine the rear passivation and back reflector layers, without the detrimental impact on the CIGS absorber layer from the metal diffusion. To that end, a new architecture and fabrication process was proposed, with the methods to optimize and characterize said architecture explained. The optimization workflow involved the careful deployment of optical simulations through the FDTD method, coupled with the creation and refinement of an electrical model for an in-depth study of the underlying phenomena, and how to best tailor the structures towards them with the intent of maximizing the solar cell's performance. Along side the design optimization, the fabrication efforts successfully fabricated substrates with the desired rear passivation and optical enhancing structures, with characterization steps occurring throughout the fabrication process. On completion, the resulting samples were shipped to the Ångström Solar Center, where the remainder of the CIGS fabrication process took place. The J-V and EQE analysis revealed lackluster results, with results below the expectation set from the design phase. However, TEM analysis revealed flaws in the fabrication process, namely, the oxidation of the rear reflector layer and deficiencies during the etching steps, resulting in unopened electrical contacts and leftover resist residue. Despite said shortcomings, the encapsulated solar cell revealed performance on par with the reference, hinting at the efficacy of the passivation structure, once unrestrained.

The work here displayed is far from what can be achieved by the CIGS technology. In the design phase, the light enhancing structure architecture can be further optimized by the implementation of inverted design routines. In other words, computational tools that allow for the development of the geometry of the rear reflector by inputting the final design figures of merit first, and then determining the design through the desired output performance, instead of the traditional methodology. The electrical model has the potential to be further refined by the implementation of the elemental distribution effects, and the set of results can be further expanded by continuing the development of the data extraction workflow. Furthermore, the accuracy of the electrical model can be improved through the development of the CIGS thermal model, thus including the thermodynamic influence in the charge transport mechanics. In the fabrication stage, with the process flaws that crippled the performance of the fabricated solar cells determined, the respective solutions are already being developed with the intention of reaching the initial goal. The performance of this architecture can be expanded even further through the deployment of additional light trapping schemes, such as nanoparticles. If coupled with industry friendly lithography processes, such as nanoimprint lithography, the architecture here developed can help push ever further the CIGS technology, into solving the energy problems of today and tomorrow.

Bibliography

- [1] M. Z. Jacobson. Review of solutions to global warming, air pollution, and energy security. Jan. 2009. Doi: 10.1039/b809990c.
- [2] F. Creutzig, P. Agoston, J. C. Goldschmidt, G. Luderer, G. Nemet, and R. C. Pietzcker. *The underestimated potential of solar energy to mitigate climate change*. Aug. 2017. DOI: 10.1038/nenergy.2017.140.
- [3] E. Kabir, P. Kumar, S. Kumar, A. A. Adelodun, and K. H. Kim. *Solar energy: Potential and future prospects.* Feb. 2018. DOI: 10.1016/j.rser.2017.09.094.
- [4] T. Tsoutsos, N. Frantzeskaki, and V. Gekas. "Environmental impacts from the solar energy technologies." In: *Energy Policy* 33.3 (Feb. 2005), pp. 289–296. ISSN: 03014215. DOI: 10.1016/S0301-4215(03)00241-6.
- [5] A. Jäger-Waldau. *PV Status Report 2019, EUR 29938*. Tech. rep. 2019, p. 85. doi: 10.2760/326629.
- [6] Champion Photovoltaic Module Efficiency Chart | Photovoltaic Research | NREL. URL: https://www.nrel.gov/pv/module-efficiency.html.
- [7] K. Sopian, S. L. Cheow, and S. H. Zaidi. "An overview of crystalline silicon solar cell technology: Past, present, and future." In: *AIP Conference Proceedings*. Vol. 1877. 1. American Institute of Physics Inc., Sept. 2017, p. 020004. ISBN: 9780735415577. DOI: 10.1063/1.4999854.
- [8] R. E. N. Members. Renewables 2020 global status report. REN21, 2020. ISBN: 9783948393007. URL: https://www.ren21.net.
- [9] S. Philipps. "Photovoltaics Report." In: May (2020). URL: https://www.ise.fraunhofer.de/en/publications/studies/photovoltaics-report.html.
- [10] K. L. Chopra, P. D. Paulson, and V. Dutta. "Thin-film solar cells: an overview." In: *Progress in Photovoltaics: Research and Applications* 12.23 (Mar. 2004), pp. 69–92. ISSN: 1062-7995. DOI: 10.1002/pip.541.
- [11] A. Shah, P. Torres, R. Tscharner, N. Wyrsch, and H. Keppner. *Photovoltaic technology: The case for thin-film solar cells.* July 1999. DOI: 10.1126/science.285.5428.692.
- [12] L. C. Andreani, A. Bozzola, P. Kowalczewski, M. Liscidini, and L. Redorici. *Silicon solar cells: Toward the efficiency limits*. Jan. 2019. DOI: 10.1080/23746149.2018.1548305.
- [13] S. R. Kodigala. *Introduction*. Vol. 35. C. Elsevier Inc., 2010, pp. 1–19. doi: 10.1016/B978-0-12-373697-0.00001-8.
- [14] S. Hegedus. "Review of photovoltaic module energy yield (kWh/kW): comparison of crystalline Si and thin film technologies." In: Wiley Interdisciplinary Reviews: Energy and Environment 2.2 (Mar. 2013), pp. 218–233. ISSN: 20418396. DOI: 10.1002/wene.61.
- [15] R. Gottschalg, T. R. Betts, A. Eeles, S. R. Williams, and J. Zhu. "Influences on the energy delivery of thin film photovoltaic modules." In: *Solar Energy Materials and Solar Cells* 119 (Dec. 2013), pp. 169–180. ISSN: 09270248. DOI: 10.1016/j.solmat.2013.06.011.
- [16] H. Michaels, M. Rinderle, R. Freitag, I. Benesperi, T. Edvinsson, R. Socher, A. Gagliardi, and M. Freitag. "Dye-sensitized solar cells under ambient light powering machine learning: Towards autonomous smart sensors for the internet of things." In: *Chemical Science* 11.11 (Mar. 2020), pp. 2895–2906. ISSN: 20416539. DOI: 10.1039/c9sc06145b.
- [17] Z. Wang, Z. Song, Y. Yan, S. F. Liu, and D. Yang. *Perovskite—a Perfect Top Cell for Tandem Devices to Break the S–Q Limit*. Apr. 2019. DOI: 10.1002/advs.201801704.

- [18] J. Ramanujam, D. M. Bishop, T. K. Todorov, O. Gunawan, J. Rath, R. Nekovei, E. Artegiani, and A. Romeo. *Flexible CIGS, CdTe and a-Si:H based thin film solar cells: A review*. May 2020. DOI: 10.1016/j.pmatsci.2019.100619.
- [19] R. Wuerz, A. Eicke, F. Kessler, and F. Pianezzi. "Influence of iron on the performance of CIGS thin-film solar cells." In: *Solar Energy Materials and Solar Cells* 130 (Nov. 2014), pp. 107–117. ISSN: 09270248. DOI: 10.1016/j.solmat.2014.06.038.
- [20] M. Saifullah, S. Ahn, J. Gwak, S. Ahn, K. Kim, J. Cho, J. H. Park, Y. J. Eo, A. Cho, J. S. Yoo, and J. H. Yun. "Development of semitransparent CIGS thin-film solar cells modified with a sulfurized-AgGa layer for building applications." In: *Journal of Materials Chemistry A* 4.27 (July 2016), pp. 10542–10551. ISSN: 20507496. DOI: 10.1039/c6ta01909a.
- [21] T. Feurer, P. Reinhard, E. Avancini, B. Bissig, J. Löckinger, P. Fuchs, R. Carron, T. P. Weiss, J. Perrenoud, S. Stutterheim, S. Buecheler, and A. N. Tiwari. "Progress in thin film CIGS photovoltaics Research and development, manufacturing, and applications." In: *Progress in Photovoltaics: Research and Applications* 25.7 (July 2017), pp. 645–667. ISSN: 1099159X. DOI: 10.1002/pip.2811.
- [22] B. P. Jelle and C. Breivik. "The path to the building integrated photovoltaics of tomorrow." In: *Energy Procedia*. Vol. 20. Elsevier Ltd, Jan. 2012, pp. 78–87. ISBN: 9781627484299. DOI: 10.1016/j.egypro.2012.03.010.
- [23] PHOTOVOLTAIC AUSTRIA | bipv-award. url: https://www.pvaustria.at/bipv-award/.
- [24] CIGS Modules nice-solar-energy.com [EN]. URL: https://nice-solarenergy.com/en/cigs-modules.html.
- [25] K. U. Clemens Heske, I. Daniel Lincot, Z. Michael Powalla, I. Pedro Salomé, H. Rutger Schlatmann, and E. Ayodhya N. Tiwari. CIGS White Paper 2019 CIGS Thin-Film Photovoltaics. URL: https://cigs-pv.net/cigs-white-paper-2019-now-available/.
- [26] W. Meng, P. Jinqing, Y. Hongxing, and L. Yimo. "Performance evaluation of semi-transparent CdTe thin film PV window applying on commercial buildings in Hong Kong." In: *Energy Procedia*. Vol. 152. Elsevier Ltd, Oct. 2018, pp. 1091–1096. DOI: 10.1016/j.egypro.2018.09.131.
- [27] Best Research-Cell Efficiency Chart | Photovoltaic Research | NREL. URL: https://www.nrel.gov/pv/cell-efficiency.html.
- [28] T. Shimizu. "Staebler-Wronski effect in hydrogenated amorphous silicon and related alloy films." In: Japanese Journal of Applied Physics, Part 1: Regular Papers and Short Notes and Review Papers 43.6 A (June 2004), pp. 3257–3268. ISSN: 00214922. DOI: 10.1143/JJAP.43.3257.
- [29] T. D. Lee and A. U. Ebong. A review of thin film solar cell technologies and challenges. Apr. 2017. DOI: 10.1016/j.rser.2016.12.028.
- [30] M. Konagai. *Present status and future prospects of silicon thin-film solar cells*. Mar. 2011. DOI: 10.1143/JJAP.50.030001.
- [31] A. H. Munshi, N. Sasidharan, S. Pinkayan, K. L. Barth, W. S. Sampath, and W. Ongsakul. "Thin-film CdTe photovoltaics The technology for utility scale sustainable energy generation." In: *Solar Energy* 173 (Oct. 2018), pp. 511–516. ISSN: 0038092X. DOI: 10.1016/j.solener.2018.07.090.
- [32] J. Ramanujam and U. P. Singh. Copper indium gallium selenide based solar cells A review. June 2017. DOI: 10.1039/c7ee00826k.

- [33] A. Ramos-Ruiz, J. V. Wilkening, J. A. Field, and R. Sierra-Alvarez. "Leaching of cadmium and tellurium from cadmium telluride (CdTe) thin-film solar panels under simulated landfill conditions." In: *Journal of Hazardous Materials* 336 (Aug. 2017), pp. 57–64. ISSN: 18733336. DOI: 10.1016/j.jhazmat.2017.04.052.
- [34] L. Stamford and A. Azapagic. "Environmental impacts of copper-indium-gallium-selenide (CIGS) photovoltaics and the elimination of cadmium through atomic layer deposition." In: *Science of the Total Environment* 688 (Oct. 2019), pp. 1092–1101. ISSN: 18791026. DOI: 10.1016/j.scitotenv.2019.06.343.
- [35] M. Nakamura, K. Yamaguchi, Y. Kimoto, Y. Yasaki, T. Kato, and H. Sugimoto. "Cd-Free Cu(In,Ga)(Se,S)₂ thin-film solar cell with record efficiency of 23.35%." In: *IEEE Journal of Photovoltaics* 9.6 (Nov. 2019), pp. 1863–1867. ISSN: 21563403. DOI: 10.1109/JPHOTOV.2019.2937218.
- [36] R. Kamada, T. Yagioka, S. Adachi, A. Handa, K. F. Tai, T. Kato, and H. Sugimoto. "New world record Cu(In,Ga)(Se,S)₂ thin film solar cell efficiency beyond 22%." In: *Conference Record of the IEEE Photovoltaic Specialists Conference*. Vol. 2016-Novem. Institute of Electrical and Electronics Engineers Inc., Nov. 2016, pp. 1287–1291. ISBN: 9781509027248. DOI: 10.1109/PVSC.2016.7749822.
- [37] M. M. A. Moon, M. F. Rahman, J. Hossain, and A. B. M. Ismail. "Comparative Study of the Second Generation a-Si:H, CdTe, and CIGS Thin-Film Solar Cells." In: *Advanced Materials Research* 1154 (June 2019), pp. 102–111. DOI: 10.4028/www.scientific.net/amr.1154.102.
- [38] F. K. A. Jörg Palm. "White paper for CIGS thin film solar cell technology 2016." In: SIVA Marketing (2016). URL: www.cigs-pv.net.
- [39] N. G. Dhere. "Scale-up issues of CIGS thin film PV modules." In: *Solar Energy Materials and Solar Cells*. Vol. 95. 1. North-Holland, Jan. 2011, pp. 277–280. DOI: 10.1016/j.solmat.2010.02.019.
- [40] A. Stamp, P. A. Wäger, and S. Hellweg. "Linking energy scenarios with metal demand modeling-The case of indium in CIGS solar cells." In: *Resources, Conservation and Recycling* 93 (Dec. 2014), pp. 156–167. ISSN: 18790658. DOI: 10.1016/j.resconrec.2014. 10.012.
- [41] C. Candelise, M. Winskel, and R. Gross. "Implications for CdTe and CIGS technologies production costs of indium and tellurium scarcity." In: *Progress in Photovoltaics: Research and Applications*. Vol. 20. 6. John Wiley & Sons, Ltd, Sept. 2012, pp. 816–831. DOI: 10.1002/pip.2216.
- [42] J. M. Cunha, C. Rocha, C. Vinhais, P. A. Fernandes, and P. M. Salome. "Understanding the AC Equivalent Circuit Response of Ultrathin Cu(In,Ga)Se₂ Solar Cells." In: *IEEE Journal of Photovoltaics* 9.5 (Sept. 2019), pp. 1442–1448. ISSN: 21563403. DOI: 10.1109/JPHOTOV.2019.2927918.
- [43] P. M. P. Salomé, B. Vermang, R. Ribeiro-Andrade, J. P. Teixeira, J. M. V. Cunha, M. J. Mendes, S. Haque, J. Borme, H. Águas, E. Fortunato, R. Martins, J. C. González, J. P. Leitão, P. A. Fernandes, M. Edoff, and S. Sadewasser. "Passivation of Interfaces in Thin Film Solar Cells: Understanding the Effects of a Nanostructured Rear Point Contact Layer." In: *Advanced Materials Interfaces* 5.2 (Jan. 2018), p. 1701101. ISSN: 21967350. DOI: 10.1002/admi.201701101.
- [44] R. Brendel and H. J. Queisser. "On the thickness dependence of open circuit voltages of p-n junction solar cells." In: *Solar Energy Materials and Solar Cells* 29.4 (May 1993), pp. 397–401. ISSN: 09270248. DOI: 10.1016/0927-0248(93)90098-N.

- [45] B. Dimmler. "CIGS and CdTe based thin film PV modules, an industrial r/evolution." In: *Conference Record of the IEEE Photovoltaic Specialists Conference*. 2012, pp. 2494–2499. ISBN: 9781467300643. DOI: 10.1109/PVSC.2012.6318101.
- [46] N. Naghavi, F. Mollica, J. Goffard, J. Posada, A. Duchatelet, M. Jubault, F. Donsanti, A. Cattoni, S. Collin, P. P. Grand, J. J. Greffet, and D. Lincot. "Ultrathin Cu(In,Ga)Se₂ based solar cells." In: *Thin Solid Films* 633 (July 2017), pp. 55–60. ISSN: 00406090. DOI: 10.1016/j.tsf.2016.11.029.
- [47] O. Lundberg, M. Edoff, and L. Stolt. "The effect of Ga-grading in CIGS thin film solar cells." In: *Thin Solid Films*. Vol. 480-481. Elsevier, June 2005, pp. 520–525. DOI: 10.1016/j.tsf.2004.11.080.
- [48] J. M. Cunha, P. A. Fernandes, P. M. Salome, T. S. Lopes, S. Bose, A. Hultqvist, W. C. Chen, O. Donzel-Gargand, R. M. Ribeiro, A. J. Oliveira, and M. Edoff. "Decoupling of Optical and Electrical Properties of Rear Contact CIGS Solar Cells." In: *IEEE Journal of Photovoltaics* 9.6 (Nov. 2019), pp. 1857–1862. ISSN: 21563403. DOI: 10.1109/JPHOTOV. 2019.2933357.
- [49] S. Siebentritt. "What limits the efficiency of chalcopyrite solar cells?" In: Solar Energy Materials and Solar Cells 95.6 (June 2011), pp. 1471–1476. ISSN: 09270248. DOI: 10.1016/j.solmat.2010.12.014.
- [50] B. Vermang, V. Fjällström, J. Pettersson, P. Salomé, and M. Edoff. "Development of rear surface passivated Cu(In,Ga)Se₂ thin film solar cells with nano-sized local rear point contacts." In: *Solar Energy Materials and Solar Cells* 117 (2013), pp. 505–511. ISSN: 09270248. DOI: 10.1016/j.solmat.2013.07.025.
- [51] D. Ledinek, P. Salomé, C. Hägglund, U. Zimmermann, and M. Edoff. "Rear Contact Passivation for High Bandgap Cu(In,Ga)Se₂ Solar Cells with a Flat Ga profile." In: *IEEE Journal of Photovoltaics* 8.3 (May 2018), pp. 864–870. ISSN: 21563381. DOI: 10.1109/JPHOTOV.2018.2813259.
- [52] S. Choi, Y. Kamikawa, J. Nishinaga, A. Yamada, H. Shibata, and S. Niki. "Lithographic fabrication of point contact with Al₂O₃ rear-surface-passivated and ultra-thin Cu(In,Ga)Se₂ solar cells." In: *Thin Solid Films* 665 (Nov. 2018), pp. 91–95. ISSN: 00406090. DOI: 10.1016/j.tsf.2018.08.044.
- [53] S. Bose, J. M. V. Cunha, S. Suresh, J. De Wild, T. S. Lopes, J. R. S. Barbosa, R. Silva, J. Borme, P. A. Fernandes, B. Vermang, and P. M. P. Salomé. "Optical Lithography Patterning of SiO₂ Layers for Interface Passivation of Thin Film Solar Cells." In: Solar RRL 2.12 (Dec. 2018), p. 1800212. ISSN: 2367-198X. DOI: 10.1002/solr.201800212.
- [54] T. S. Lopes, J. M. Cunha, S. Bose, J. R. Barbosa, J. Borme, O. Donzel-Gargand, C. Rocha, R. Silva, A. Hultqvist, W. C. Chen, A. G. Silva, M. Edoff, P. A. Fernandes, and P. M. Salome. "Rear Optical Reflection and Passivation Using a Nanopatterned Metal/Dielectric Structure in Thin-Film Solar Cells." In: *IEEE Journal of Photovoltaics* 9.5 (Sept. 2019), pp. 1421–1427. ISSN: 21563403. DOI: 10.1109/JPHOTOV.2019.2922323.
- [55] J. Goffard, C. Colin, F. Mollica, A. Cattoni, C. Sauvan, P. Lalanne, J. F. Guillemoles, N. Naghavi, and S. Collin. "Light Trapping in Ultrathin CIGS Solar Cells with Nanostructured Back Mirrors." In: *IEEE Journal of Photovoltaics* 7.5 (Sept. 2017), pp. 1433–1441. ISSN: 21563381. DOI: 10.1109/JPHOTOV.2017.2726566.
- [56] R. J. Matson, O. Jamjoum, A. D. Buonaquisti, P. E. Russell, L. L. Kazmerski, P. Sheldon, and R. K. Ahrenkiel. "Metal contacts to CuInSe₂." In: *Solar Cells* 11.3 (Apr. 1984), pp. 301–305. ISSN: 03796787. DOI: 10.1016/0379-6787(84)90019-X.

- [57] T. Wada, N. Kohara, S. Nishiwaki, and T. Negami. "Characterization of the Cu(In,Ga)Se₂/Mo interface in CIGS solar cells." In: *Thin Solid Films* 387.1-2 (May 2001), pp. 118–122. ISSN: 00406090. DOI: 10.1016/S0040-6090(00)01846-0.
- [58] Accurately Simulate Photonic Components and Circuits Lumerical. URL: https://www.lumerical.com/products/.
- [59] M. D. Archer and M. A. Green. *Clean Electricity from Photovoltaics*. 2nd. Vol. 4. Series on Photoconversion of Solar Energy. IMPERIAL COLLEGE PRESS, Dec. 2014, p. 671. ISBN: 978-1-84816-767-4. DOI: 10.1142/p798.
- [60] K. Momma and F. Izumi. "VESTA 3 for three-dimensional visualization of crystal volumetric and morphology data." In: *Journal of Applied Crystallography* 44.6 (Dec. 2011), pp. 1272–1276. ISSN: 00218898. DOI: 10.1107/S0021889811038970.
- [61] L. Kaplan, G. Leitus, V. Lyakhovitskaya, F. Frolow, H. Hallak, Kvick, and D. Cahen. "Synchrotron X-ray Diffraction Evidence for Native Defects in the Photovoltaic Semiconductor CuInSe₂." In: *Advanced Materials* 12.5 (Mar. 2000), pp. 366–370. ISSN: 1521-4095. DOI: 10.1002/(SICI)1521-4095(200003)12:5<366::AID-ADMA366>3.0.C0;2-9.
- [62] D. Xia, M. Xu, J. Li, and X. Zhao. "Co-electrodeposition and Characterization of Cu (In, Ga)Se₂ thin films." In: *Journal of Materials Science* 41.7 (Apr. 2006), pp. 1875–1878. ISSN: 00222461. DOI: 10.1007/s10853-006-4432-7.
- [63] A. Romeo, M. Terheggen, D. Abou-Ras, D. L. Bätzner, F.-J. Haug, M. Kälin, D. Rudmann, and A. N. Tiwari. "Development of thin-film Cu(In,Ga)Se₂ and CdTe solar cells." In: *Progress in Photovoltaics: Research and Applications* 12.23 (Mar. 2004), pp. 93–111. ISSN: 1062-7995. DOI: 10.1002/pip.527.
- [64] J. Hedstrom, H. Ohlsen, M. Bodegard, A. Klyner, L. Stolt, D. Hariskos, M. Ruckh, and H. W. Schock. "ZnO/CdS/Cu(In,Ga)Se₂ thin film solar cells with improved performance." In: *Conference Record of the IEEE Photovoltaic Specialists Conference*. Publ by IEEE, 1993, pp. 364–371. ISBN: 0780312201. DOI: 10.1109/pvsc.1993.347154.
- [65] T. Wada, N. Kohara, T. Negami, and M. Nishitani. "Chemical and structural characterization of Cu(In, Ga)Se₂/Mo interface in Cu(In, Ga)Se₂ solar cells." In: *Japanese Journal of Applied Physics, Part 2: Letters* 35.10 PART A (Oct. 1996), p. L1253. ISSN: 00214922. DOI: 10.1143/jjap.35.11253.
- [66] L. Weinhardt, C. Heske, E. Umbach, T. P. Niesen, S. Visbeck, and F. Karg. "Band alignment at the i-ZnO/CdS interface in Cu(In,Ga)(S,Se)₂ thin-film solar cells." In: *Applied Physics Letters* 84.16 (Apr. 2004), pp. 3175–3177. ISSN: 00036951. DOI: 10.1063/1.1704877.
- [67] U. Rau and M. Schmidt. "Electronic properties of ZnO/CdS/Cu(In,Ga)Se₂ solar cells Aspects of heterojunction formation." In: *Thin Solid Films* 387.1-2 (May 2001), pp. 141–146. ISSN: 00406090. DOI: 10.1016/S0040-6090(00)01737-5.
- [68] J. Lindahl, U. Zimmermann, P. Szaniawski, T. Torndahl, A. Hultqvist, P. Salomé, C. Platzer-Björkman, and M. Edoff. "Inline Cu(In,Ga)Se₂ co-evaporation for high-efficiency solar cells and modules." In: *IEEE Journal of Photovoltaics* 3.3 (2013), pp. 1100–1105. ISSN: 21563381. DOI: 10.1109/JPHOTOV.2013.2256232.
- [69] J. L. Shay, S. Wagner, and H. M. Kasper. "Efficient CuInSe₂/CdS solar cells." In: *Applied Physics Letters* 27.2 (July 1975), pp. 89–90. ISSN: 00036951. DOI: 10.1063/1.88372.
- [70] L. L. Kazmerski, F. R. White, and G. K. Morgan. "Thin-film CuInSe₂/CdS heterojunction solar cells." In: *Applied Physics Letters* 29.4 (Aug. 1976), pp. 268–270. ISSN: 00036951. DOI: 10.1063/1.89041.

- [71] K. W. Böer. "Cadmium sulfide enhances solar cell efficiency." In: *Energy Conversion and Management*. Vol. 52. 1. Elsevier Ltd, Jan. 2011, pp. 426–430. DOI: 10.1016/j.enconman.2010.07.017.
- [72] L. M. Mansfield, A. Kanevce, S. P. Harvey, K. Bowers, C. Beall, S. Glynn, and I. L. Repins. "Efficiency increased to 15.2% for ultra-thin Cu(In,Ga)Se₂ solar cells." In: *Progress in Photovoltaics: Research and Applications* 26.11 (Nov. 2018), pp. 949–954. ISSN: 10627995. DOI: 10.1002/pip.3033.
- [73] Y.-C. Wang, C.-W. Chen, T.-Y. Su, T.-Y. Yang, W.-W. Liu, F. Cheng, Z. M. Wang, and Y.-L. Chueh. "Design of suppressing optical and recombination losses in ultrathin CuInGaSe2 solar cells by Voronoi nanocavity arrays." In: *Nano Energy* 78 (Aug. 2020), p. 105225. ISSN: 22112855. DOI: 10.1016/j.nanoen.2020.105225.
- [74] A. Oliveira, J. de Wild, K. Oliveira, B. A. Valença, J. P. Teixeira, J. R. L. Guerreiro, S. Abalde-Cela, T. S. Lopes, R. M. Ribeiro, J. M. V. Cunha, M. A. Curado, M. Monteiro, A. Violas, A. G. Silva, M. Prado, P. A. Fernandes, B. Vermang, and P. M. Salomé. "Encapsulation of Nanostructures in a Dielectric Matrix Providing Optical Enhancement in Ultra-thin Solar Cells." In: *Solar RRL* (Aug. 2020), solr.202000310. ISSN: 2367-198X. DOI: 10.1002/solr.202000310.
- [75] G. Sozzi, S. Di Napoli, R. Menozzi, B. Bissig, S. Buecheler, and A. N. Tiwari. "Impact of front-side point contact/passivation geometry on thin-film solar cell performance." In: *Solar Energy Materials and Solar Cells* 165 (June 2017), pp. 94–102. ISSN: 09270248. DOI: 10.1016/j.solmat.2017.02.031.
- [76] G. Brown, P. Stone, J. Woodruff, B. Cardozo, and D. Jackrel. "Device characteristics of a 17.1% efficient solar cell deposited by a non-vacuum printing method on flexible foil." In: *Conference Record of the IEEE Photovoltaic Specialists Conference*. 2012, pp. 3230–3233. ISBN: 9781467300643. DOI: 10.1109/PVSC.2012.6318265.
- [77] S. Silvestre. "Strategies for Fault Detection and Diagnosis of PV Systems." In: *Advances in Renewable Energies and Power Technologies*. Vol. 1. Elsevier, Feb. 2018, pp. 231–255. ISBN: 9780128132173. DOI: 10.1016/B978-0-12-812959-3.00007-1.
- [78] P. Salomé. "Chalcogenide Thin Films for Solar Cells: Growth and Properties." Doctoral dissertation. Universidade de Aveiro, 2011, pp. 1–161. URL: http://hdl.handle.net/10773/3723.
- [79] F. Mollica, J. Goffard, M. Jubault, F. Donsanti, S. Collin, A. Cattoni, L. Lombez, and N. Naghavi. "Comparative study of patterned TiO₂ and Al₂O₃ layers as passivated back-contact for ultra-thin Cu(In, Ga)Se₂ solar cells." In: *Conference Record of the IEEE Photovoltaic Specialists Conference*. Vol. 2016-Novem. Institute of Electrical and Electronics Engineers Inc., Nov. 2016, pp. 2213–2217. ISBN: 9781509027248. DOI: 10.1109/PVSC.2016.7750028.
- [80] O. Lundberg, M. Bodegard, J. Malmstrom, and L. Stolt. "Influence of the Cu(In,Ga)Se₂ thickness and Ga grading on solar cell performance." In: *Progress in Photovoltaics: Research and Applications* 11.2 (Mar. 2003), pp. 77–88. ISSN: 10627995. DOI: 10.1002/pip.462.
- [81] O. Isabella, K. Jager, A. Smets, R. Van Swaaij, and M. Zeman. *Solar Energy: The Physics and Engineering of Photovoltaic Conversion, Technologies and Systems*. UIT Cambridge Ltd., 2016. ISBN: 9781906860738.
- [82] S. Karki, P. Paul, G. Rajan, B. Belfore, D. Poudel, A. Rockett, E. Danilov, F. Castellano, A. Arehart, and S. Marsillac. "Analysis of recombination mechanisms in rbf-treated cigs solar cells." In: *IEEE Journal of Photovoltaics* 9.1 (Jan. 2019), pp. 313–318. ISSN: 21563381. DOI: 10.1109/JPHOTOV.2018.2877596.

- [83] S. Sze and K. K. Ng. "Photodetectors and Solar Cells." In: *Physics of Semiconductor Devices*. Hoboken, NJ, USA: John Wiley & Sons, Inc., Apr. 2006, pp. 663–742. DOI: 10.1002/9780470068328.ch13.
- [84] L. A. Kosyachenko, X. Mathew, P. D. Paulson, V. Y. Lytvynenko, and O. L. Maslyanchuk. "Optical and recombination losses in thin-film Cu(In,Ga)Se₂ solar cells." In: *Solar Energy Materials and Solar Cells* 130 (Nov. 2014), pp. 291–302. ISSN: 09270248. DOI: 10.1016/j.solmat.2014.07.019.
- [85] G. Birant, J. de Wild, M. Meuris, J. Poortmans, and B. Vermang. "Dielectric-Based Rear Surface Passivation Approaches for Cu(In,Ga)Se₂ Solar Cells—A Review." In: *Applied Sciences* 9.4 (Feb. 2019), p. 677. ISSN: 2076-3417. DOI: 10.3390/app9040677.
- [86] W. Li, W. Li, Y. Feng, and C. Yang. "Numerical analysis of the back interface for high efficiency wide band gap chalcopyrite solar cells." In: *Solar Energy* 180 (Mar. 2019), pp. 207–215. ISSN: 0038092X. DOI: 10.1016/j.solener.2019.01.018.
- [87] J. M. Cunha, P. A. Fernandes, A. Hultqvist, J. P. Teixeira, S. Bose, B. Vermang, S. Garud, D. Buldu, J. Gaspar, M. Edoff, J. P. Leitao, and P. M. Salome. "Insulator Materials for Interface Passivation of Cu(In,Ga)Se₂ Thin Films." In: *IEEE Journal of Photovoltaics* 8.5 (Sept. 2018), pp. 1313–1319. ISSN: 21563381. DOI: 10.1109/JPHOTOV.2018.2846674.
- [88] B. Vermang, J. T. Wätjen, V. Fjällström, F. Rostvall, M. Edoff, R. Kotipalli, F. Henry, and D. Flandre. "Employing Si solar cell technology to increase efficiency of ultra-thin Cu(In,Ga)Se₂ solar cells." In: *Progress in Photovoltaics: Research and Applications* 22.10 (Oct. 2014), pp. 1023–1029. ISSN: 10627995. DOI: 10.1002/pip.2527.
- [89] W. Li, X. Yan, W. L. Xu, J. Long, A. G. Aberle, and S. Venkataraj. "Efficiency improvement of CIGS solar cells by a modified rear contact." In: *Solar Energy* 157 (Nov. 2017), pp. 486–495. ISSN: 0038092X. DOI: 10.1016/j.solener.2017.08.054.
- [90] S. Morawiec, M. J. Mendes, S. Mirabella, F. Simone, F. Priolo, and I. Crupi. "Self-assembled silver nanoparticles for plasmon-enhanced solar cell back reflectors: correlation between structural and optical properties." In: *Nanotechnology* 24.26 (July 2013), p. 265601. ISSN: 0957-4484. DOI: 10.1088/0957-4484/24/26/265601.
- [91] E. D. Palik. *Handbook of optical constants of solids*. Academic Press, 1985. ISBN: 0125444206 9780125444200. DOI: https://doi.org/10.1016/C2009-0-20920-2.
- [92] W. M. Haynes. CRC Handbook of Chemistry and Physics, 101st Edition. Ed. by CRC Press. Taylor & Francis, 2020. ISBN: 9780367417246.
- [93] T. A. Green. "Gold etching for microfabrication." In: *Gold Bulletin* 47.3 (Sept. 2014), pp. 205–216. ISSN: 2190-7579. DOI: 10.1007/s13404-014-0143-z.
- [94] High resolution lithography: EBL tool EBPG5200. URL: https://www.raith.com/products/ebpg5200.html.
- [95] DWL Series High Resolution Pattern Generators Heidelberg Instruments: The power of direct writing. URL: https://heidelberg-instruments.com/en/products/dwl-2000-4000.html.
- [96] Optoelectronic Modeling Lumerical. URL: https://www.lumerical.com/learn/whitepapers/optoelectronic-modeling/.
- [97] A. Taflove and S. C. Hagness. *Computational electrodynamics: the finite-difference time-domain method; 3rd ed.* Artech House antennas and propagation library. Boston, MA: Artech House, 2005. URL: https://cds.cern.ch/record/1698084.
- [98] Overcoming the Multi-wavelength FDTD Challenge Lumerical. URL: https://www.lumerical.com/learn/whitepapers/overcoming-the-multi-wavelength-fdtd-challenge/.

- [99] Finite Difference Time Domain (FDTD) solver introduction Lumerical Support. URL: https://support.lumerical.com/hc/en-us/articles/360034914633-Finite-Difference-Time-Domain-FDTD-solver-introduction.
- [100] CHARGE solver introduction Lumerical Support. URL: https://support.lumerical.com/hc/en-us/articles/360034917693-CHARGE-solver-introduction.
- [101] D. Vasileska, S. M. Goodnick, and G. Klimeck. *Computational electronics: Semiclassical and quantum device modeling and simulation*. CRC Press, Jan. 2017, pp. 1–764. ISBN: 9781420064841. DOI: 10.1201/b13776.
- [102] S. Garud, B. Vermang, S. Sahayaraj, S. Ranjbar, G. Brammertz, M. Meuris, A. Smets, and J. Poortmans. "Alkali Assisted Reduction of Open-Circuit Voltage Deficit in CZTSe Solar Cells." In: *Physica Status Solidi (C) Current Topics in Solid State Physics*. Vol. 14. 10. Wiley-VCH Verlag, Oct. 2017. DOI: 10.1002/pssc.201700171.
- [103] C. Van Lare, G. Yin, A. Polman, and M. Schmid. "Light Coupling and Trapping in Ultrathin Cu(In,Ga)Se₂ Solar Cells Using Dielectric Scattering Patterns." In: *ACS Nano* 9.10 (Sept. 2015), pp. 9603–9613. ISSN: 1936086X. DOI: 10.1021/acsnano.5b04091.
- [104] J. H. Werner, J. Mattheis, and U. Rau. "Efficiency limitations of polycrystalline thin film solar cells: Case of Cu(In,Ga)Se₂." In: *Thin Solid Films*. Vol. 480-481. Elsevier, June 2005, pp. 399–409. DOI: 10.1016/j.tsf.2004.11.052.
- [105] G. Brown, V. Faifer, A. Pudov, S. Anikeev, E. Bykov, M. Contreras, and J. Wu. "Determination of the minority carrier diffusion length in compositionally graded Cu(In,Ga)Se₂ solar cells using electron beam induced current." In: *Applied Physics Letters* 96.2 (Jan. 2010), p. 022104. ISSN: 00036951. DOI: 10.1063/1.3291046.
- [106] R. Kniese, M. Powalla, and U. Rau. "Evaluation of electron beam induced current profiles of Cu(In,Ga)Se₂ solar cells with different Ga-contents." In: *Thin Solid Films* 517.7 (Feb. 2009), pp. 2357–2359. ISSN: 00406090. DOI: 10.1016/j.tsf.2008.11.049.
- [107] S. Bose, J. Cunha, J. Borme, W. Chen, N. Nilsson, J. Teixeira, J. Gaspar, J. Leitão, M. Edoff, P. Fernandes, and P. Salomé. "A morphological and electronic study of ultrathin rear passivated Cu(In,Ga)Se₂ solar cells." In: *Thin Solid Films* 671 (Feb. 2019), pp. 77–84. ISSN: 00406090. DOI: 10.1016/j.tsf.2018.12.028.
- [108] J. Lontchi, M. Zhukova, M. Kovacic, J. Krc, W.-C. Chen, M. Edoff, S. Bose, P. M. P. Salome, J. Goffard, A. Cattoni, L. Gouillart, S. Collin, V. Gusak, and D. Flandre. "Optimization of Back Contact Grid Size in Al₂O₃ Rear Passivated Ultrathin CIGS PV Cells by 2D Simulations." In: *IEEE Journal of Photovoltaics* (Aug. 2020), pp. 1–10. ISSN: 2156-3381. DOI: 10.1109/jphotov.2020.3012631.
- [109] W. W. Hsu, J. Y. Chen, T. H. Cheng, S. C. Lu, W. S. Ho, Y. Y. Chen, Y. J. Chien, and C. W. Liu. "Surface passivation of Cu(In,Ga)Se₂ using atomic layer deposited Al₂O₃." In: Applied Physics Letters 100.2 (Jan. 2012), p. 023508. ISSN: 00036951. DOI: 10.1063/1.3675849.
- [110] K. Gartsman, L. Chernyak, V. Lyahovitskaya, D. Cahen, V. Didik, V. Kozlovsky, R. Malkovich, E. Skoryatina, and V. Usacheva. "Direct evidence for diffusion and electromigration of Cu in CuInSe₂." In: *Journal of Applied Physics* 82.9 (Nov. 1997), pp. 4282–4285. ISSN: 00218979. DOI: 10.1063/1.366252.
- [111] J. Timo Watjen, J. Engman, M. Edoff, and C. Platzer-Björkman. "Direct evidence of current blocking by ZnSe in Cu₂ZnSnSe₄ solar cells." In: Applied Physics Letters 100.17 (Apr. 2012), p. 173510. ISSN: 00036951. DOI: 10.1063/1.4706256.

- [112] R. Carron, E. Avancini, T. Feurer, B. Bissig, P. A. Losio, R. Figi, C. Schreiner, M. Bürki, E. Bourgeois, Z. Remes, M. Nesladek, S. Buecheler, and A. N. Tiwari. "Refractive indices of layers and optical simulations of Cu(In,Ga)Se₂ solar cells." In: *Science and Technology of Advanced Materials* 19.1 (Dec. 2018), pp. 396–410. ISSN: 18785514. DOI: 10.1080/14686996.2018.1458579.
- [113] W. S. M. Werner, K. Glantschnig, and C. Ambrosch-Draxl. "Optical Constants and Inelastic Electron-Scattering Data for 17 Elemental Metals." In: *Journal of Physical and Chemical Reference Data* 38.4 (2009), pp. 1013–1092. DOI: 10.1063/1.3243762.
- [114] P. Rappaport. "The photovoltaic effect and its utilization." In: *Solar Energy* 3.4 (Dec. 1959), pp. 8–18. ISSN: 0038092X. DOI: 10.1016/0038-092X(59)90002-7.
- [115] M. J. Mendes, A. Araújo, A. Vicente, H. Águas, I. Ferreira, E. Fortunato, and R. Martins. "Design of optimized wave-optical spheroidal nanostructures for photonic-enhanced solar cells." In: *Nano Energy* 26 (Aug. 2016), pp. 286–296. ISSN: 22112855. DOI: 10.1016/j.nanoen.2016.05.038.
- [116] S. Haque, M. Alexandre, M. J. Mendes, H. Águas, E. Fortunato, and R. Martins. "Design of wave-optical structured substrates for ultra-thin perovskite solar cells." In: *Applied Materials Today* 20 (Sept. 2020), p. 100720. ISSN: 23529407. DOI: 10.1016/j.apmt. 2020.100720.
- [117] Calculating absorbed optical power Higher accuracy Lumerical Support. URL: https://support.lumerical.com/hc/en-us/articles/360034915693.
- [118] M. J. Mendes, S. Haque, O. Sanchez-Sobrado, A. Araújo, H. Águas, E. Fortunato, and R. Martins. "Optimal-Enhanced Solar Cell Ultra-thinning with Broadband Nanophotonic Light Capture." In: *iScience* 3 (May 2018), pp. 238–254. ISSN: 25890042. DOI: 10.1016/j.isci.2018.04.018.
- [119] M. Edoff, T. Jarmar, N. S. Nilsson, E. Wallin, D. Hogstrom, O. Stolt, O. Lundberg, W. Shafarman, and L. Stolt. "High Voc in (Cu,Ag)(In,Ga)Se2 Solar Cells." In: *IEEE Journal of Photovoltaics* 7.6 (Nov. 2017), pp. 1789–1794. ISSN: 21563381. DOI: 10.1109/JPHOTOV. 2017.2756058.
- [120] J. Keller, K. V. Sopiha, O. Stolt, L. Stolt, C. Persson, J. J. Scragg, T. Törndahl, and M. Edoff. "Wide-gap (Ag,Cu)(In,Ga)Se 2 solar cells with different buffer materials—A path to a better heterojunction." In: *Progress in Photovoltaics: Research and Applications* 28.4 (Apr. 2020), pp. 237–250. ISSN: 1062-7995. DOI: 10.1002/pip.3232.
- [121] J. Pettersson, C. Platzer-Björkman, U. Zimmermann, and M. Edoff. "Baseline model of graded-absorber Cu(In,Ga)Se₂ solar cells applied to cells with Zn1 XMgxO buffer layers." In: *Thin Solid Films*. Vol. 519. 21. Elsevier, Aug. 2011, pp. 7476–7480. DOI: 10.1016/j.tsf.2010.12.141.
- [122] T. M. Friedlmeier, P. Jackson, A. Bauer, D. Hariskos, O. Kiowski, R. Wuerz, and M. Powalla. "Improved Photocurrent in Cu(In,Ga)Se₂ Solar Cells: From 20.8% to 21.7% Efficiency with CdS Buffer and 21.0% Cd-Free." In: *IEEE Journal of Photovoltaics* 5.5 (Sept. 2015), pp. 1487–1491. ISSN: 21563381. DOI: 10.1109/JPH0TOV.2015.2458039.
- [123] M Gloeckler, A. L. Fahrenbruch, and J. R. Sites. "Numerical modeling of CIGS and CdTe solar cells: setting the baseline." In: 3rd World Conference on Photovoltaic Energy Conversion, 2003. Proceedings of. Vol. 1. 2003, pp. 491–494.
- [124] S. H. Wei and S. B. Zhang. "Defect properties of CuInSe2 and CuGaSe2." In: *Journal of Physics and Chemistry of Solids*. Vol. 66. 11. Pergamon, Nov. 2005, pp. 1994–1999. DOI: 10.1016/j.jpcs.2005.10.003.

- [125] Semiconductor material model properties Lumerical Support. URL: https://support.lumerical.com/hc/en-us/articles/360034919113-Semiconductor-material-model-properties.
- [126] U. Rau, K. Taretto, and S. Siebentritt. "Grain boundaries in Cu(In,Ga)(Se,S)₂ thin-film solar cells." In: *Applied Physics A: Materials Science and Processing* 96.1 (July 2009), pp. 221–234. ISSN: 09478396. DOI: 10.1007/s00339-008-4978-0.
- [127] S. Berge, P. O. Gartland, and B. J. Slagsvold. "Photoelectric work function of a molybdenum single crystal for the (100), (110), (111), (112), (114), and (332) faces." In: *Surface Science* 43.1 (May 1974), pp. 275–292. ISSN: 00396028. DOI: 10.1016/0039-6028(74)90231-3.
- [128] S. Chandra, D. P. Singh, P. C. Srivastava, and S. N. Sahu. "Electrodeposited semiconducting molybdenum selenide films. II. Optical, electrical, electrochemical and photoelectrochemical solar cell studies." In: *Journal of Physics D: Applied Physics* 17.10 (1984), pp. 2125–2138. ISSN: 00223727. DOI: 10.1088/0022-3727/17/10/023.
- [129] O. Madelung. *Semiconductors: Data Handbook*. Springer Berlin Heidelberg, 2004. DOI: 10.1007/978-3-642-18865-7.
- [130] J. S. Ross, S. Wu, H. Yu, N. J. Ghimire, A. M. Jones, G. Aivazian, J. Yan, D. G. Mandrus, D. Xiao, W. Yao, and X. Xu. "Electrical control of neutral and charged excitons in a monolayer semiconductor." In: *Nature Communications* 4.1 (Feb. 2013), pp. 1–6. ISSN: 20411723. DOI: 10.1038/ncomms2498.
- [131] N. R. Pradhan, D. Rhodes, Y. Xin, S. Memaran, L. Bhaskaran, M. Siddiq, S. Hill, P. M. Ajayan, and L. Balicas. "Ambipolar molybdenum diselenide field-effect transistors: Field-effect and hall mobilities." In: *ACS Nano* 8.8 (2014), pp. 7923–7929. ISSN: 1936086X. DOI: 10.1021/nn501693d.
- [132] Z. Jehl. "Realization of ultrathin Copper Indium Gallium Di-selenide (CIGSe) solar cells." Doctoral dissertation. Université Paris Sud Paris XI, 2012. URL: https://tel.archives-ouvertes.fr/tel-00697615.
- [133] D. Baek. "Carrier lifetimes in thin-film photovoltaics." In: *Journal of the Korean Physical Society* 67.6 (Sept. 2015), pp. 1064–1070. ISSN: 19768524. DOI: 10.3938/jkps.67. 1064.
- [134] L. Ruan, H. Zhao, D. Li, S. Jin, S. Li, L. Gu, and J. Liang. "Enhancement of Thermoelectric Properties of Molybdenum Diselenide Through Combined Mg Intercalation and Nb Doping." In: *Journal of Electronic Materials* 45.6 (June 2016), pp. 2926–2934. ISSN: 03615235. DOI: 10.1007/s11664-016-4334-7.

A | FDTD Simulations Supplementary Data

In Figure 3.8, the dependence between the height of the CIGS and the current generation was shown. However, said plot does not provide any information about the relationship between the frequency of the incident radiation and the height at where the current generation occurs. Thusly, in Figure A.1 the charge carrier generation dependence on the wavelength of the incident light and on the height in the CIGS absorber layer can be seen:

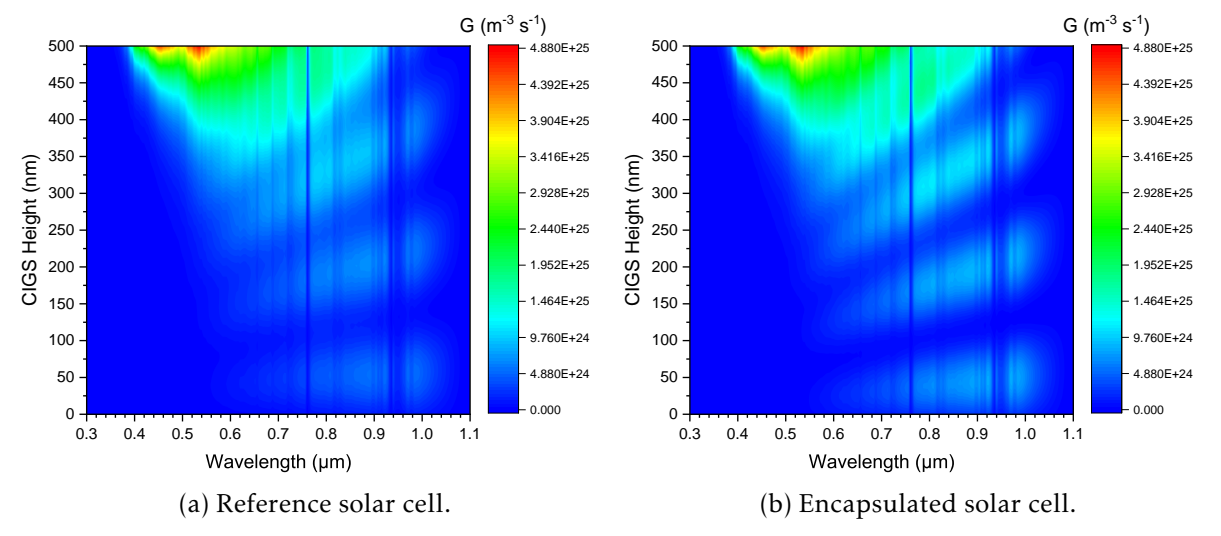


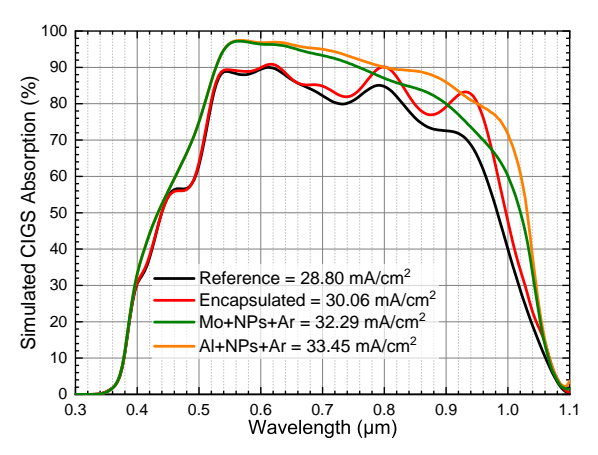
Figure A.1: Generation rate per wavelength and depending on the height of the CIGS, with 0 of the CIGS height at the Mo rear contact.

Comparing the results of the reference cell in Figure A.1a, and the encapsulated cell in Figure A.1b, it can be concluded that the optical gains in the encapsulated design occur mainly at the longer wavelengths, between 0.7 μ m and 1.0 μ m, and that a shift occurs of the carrier generation locations, being it moved closer to the highly recombinative rear interface. Future developments of the rear passivation and light trapping schemes should have the 0.7 μ m to 1.0 μ m wavelength interval into account.

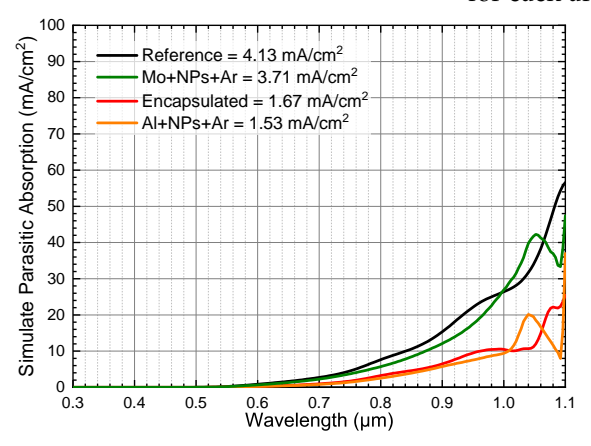
It was previously mentioned that the rear reflector and passivation layers can be coupled with other light trapping schemes, in order to further boost the photocurrent generation in a ultrathin CIGS solar cell. Therefore, further backing up said claim, simulations were ran in designs containing nanoparticles in the rear interface and with anti-reflection structures in the Al:ZnO frontal contact. The differentiating factor was the existence, or lack thereof, of the Al back reflector layer. The simulated EQE, substrate parasitic absorption (including the absorption by the nanoparticles) and total solar cell reflectance can be found in Figure A.2:

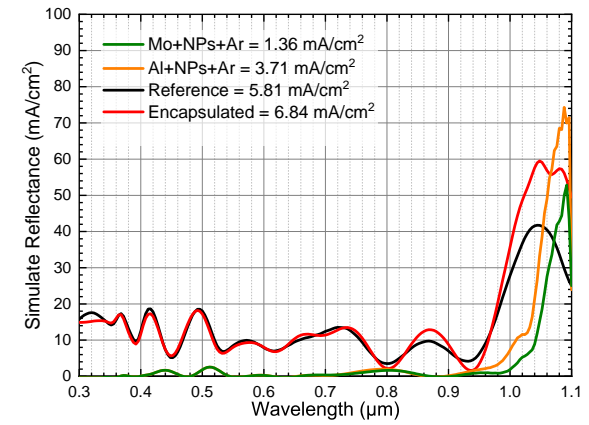
When the nanoparticles and anti-reflection layers are coupled with the rear reflector, the J_{SC} reaches 33.45 mA/cm², an 1.16 mA/cm² increase compared to a similar architecture without the rear reflector. When compared to the reference, the combination of all three light trapping schemes increase the J_{SC} by 4,65 mA/cm², a 16% increase. While the parasitic absorption in Figure A.2b, did not show very significant changes, since the nanoparticles have an inherent parasitic absorption, the reflection spectra in Figure A.2c shows the efficacy of the light trapping structures. The only significant reflection pertains to the wavelengths near or below the 1.15 eV CIGS bandgap, where the CIGS cannot absorb.

From the STEM-EDS analysis it was discovered that the 10 nm Al back reflector layer was oxidized, forming Al_2O_3 . As a consequence, the optical reflectivity of the back reflector was severely affected. This is due to the fact that Al_2O_3 at those reduced thicknesses is mostly transparent, as can be seen in the data plotted in Figure A.3:



(a) Simulated CIGS absorption spectra and J_{SC} for each architecture.





- (b) Simulated parasitic optical absorption spectra of the rear passivation and contact layers.
- (c) Simulated total solar cell reflection spectra.

Figure A.2: Optical performance of the several iterations of rear contact passivation and optically enhancing layers.

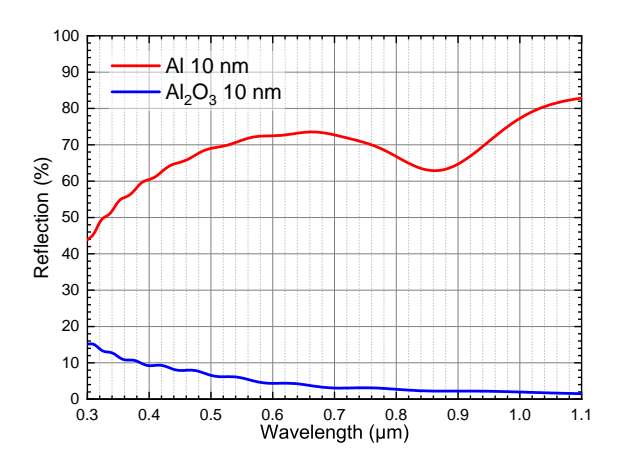


Figure A.3: Simulated reflection of 10 nm Al and Al₂O₃ films.

B CHARGE Simulations Supplementary Data

As mentioned in the electrical simulations subchapter, there was the need to create an electrical model for CIGS for the simulation software *Lumerical CHARGE*. However, even though several models are available in the literature [75, 121–123], a vast majority of them are based in the optical and electrical 1D simulator "Solar Cell Capacitance Simulator" (*SCAPS*) software which in turn, requires a set of variables that slightly differs from the ones requested by *CHARGE*. Thus, some parameters used in the *CHARGE* model were calculated from the *SCAPS* models available. Said calculations will be demonstrated below.

CIGS is a highly complex semiconductor material that displays some properties that are not found in more traditional semiconductors, such as self-doping[124] or the ability to tune the material bandgap[47]. This inherent complexity, coupled with the fact that *CHARGE* was designed with more common semiconductors in mind, such as Si or Ge, means that if the goal was to develop a model that accurately modeled the CIGS complex behaviour, the time budget required would mean that the other goals of this thesis would have to suffer a reduction in scope. Therefore instead, the aim was to create a model that while modest, was still able to provide an acceptable representation of the phenomena relevant to this thesis, such as the effects of rear contact passivation layers, while simultaneously having the possibility of being further developed at a later date.

CHARGE treats the doping of the semiconductor as a parameter detached from the fundamental material properties, as it occurs in semiconductors that can be found in an intrinsic form, such as Si. Thus, when creating a new material model, such as it was done for CIGS, the software requires the input of the work function (ϕ) of the intrinsic base material. This is a predicament for CIGS considering that this material is self-doping[124], thus, it is not possible to determine the properties of this material in an intrinsic state. As a consequence, all available models report the material electron affinity (χ) instead. Nevertheless, if the value of the electron affinity, the bandgap (E_G) and the effective density of states in conduction band (N_C) and valence band (N_V) are known, an approximation of the work function can be made through the equation B.1 [125]:

$$\chi_{s} = \phi_{s,i} - \frac{E_{G}}{2} + \frac{k_{B}T}{2} \ln \frac{N_{C}}{N_{V}}$$
(B.1)

The electrical solver takes into account various effects that might influence the mobility of the charge carriers inside the semiconductors, such as e.g. lattice scattering, impurity scattering and free carrier scattering. Thus, the effective mass of electrons and holes needs to be provided to the model. Since the value of the effective density of states for each band is known, the electron effective mass (m_e^*) and hole effective mass (m_h^*) can be calculated through the equations [125]:

$$N_C = 2 \cdot \left(\frac{2\pi m_e^* k_B T}{h^2}\right)^{3/2} \tag{B.2}$$

$$N_V = 2 \cdot \left(\frac{2\pi m_h^* k_B T}{h^2}\right)^{3/2} \tag{B.3}$$

The last parameters that needed to be calculated in order to satisfy *CHARGE* model requirements were the carrier lifetime for electrons (τ_e) and the carrier lifetime for holes (τ_h). For such, knowing the capture cross-section for electrons (σ_e), the capture cross-section for holes (σ_h) and the bulk-trap concentration (N_t) the lifetimes of each of the charge carriers can be calculated

through the equation B.4 [125]:

$$\tau_{e,h} = \left(\sigma_{e,h} N_t \sqrt{\frac{3k_B T}{m_{e,h}^*}}\right)^{-1} \tag{B.4}$$

The model makes some concessions once again, in the bandgap profile of the CIGS absorber layer. Most high efficiency CIGS solar cells will vary the Ga contents throughout the height of the absorber, in order to spatially vary the CIGS bandgap. Such feature can be implemented in *CHARGE* but it requires the modeling of CuInSe₂ and CuGaSe₂ independently. Furthermore, the bowing parameters for the alloying need to be provided. Since no reputable source for said parameter was found, instead an ungraded model was adopted, where the bandgap was set as constant throughout the CIGS absorber layer.

In order to keep the present model at a modest scale, and prevent the challenges that a more complex model faces during validation testing, certain electronic events were disregarded due to either the difficulty in their implementation, or the minute repercussions that they might have in the solar cell performance, such as the electronic activity that occurs at the CIGS grain boundaries [126].

All the necessary parameters employed in the constructed model can be found in Table B.1:

Table B.1: Model parameters used in the CIGS electrical model.

Material Properties							
	Mo	SiO_2	$MoSe_2$	CIGS	CdS	i:ZnO	Al:ZnO
φ (eV)	4.55ª	-	4.45 ^b	5.04 ^c	5.53 ^c	6.20 ^c	6.15 ^c
ε_r (DC)	-	3.9 ^d	4.8^{b}	13.6 ^e	8.73 ^f	8.75 ^f	-
Conduction Band Valley	-	-	Γ	Γ	Γ	Γ	-
$m_e^* (1/m_e)$	-	-	0.5^{g}	0.09 ^e	0.14^{e}	0.24^{e}	-
$m_h^*(1/m_e)$	-	-	0.5^{g}	0.71 ^e	0.51 ^e	0.78 ^e	-
E_G^{n} (eV)	-	-	1.66^{g}	1.15 ^e	2.40 ^e	3.30 ^e	-
$\mu_e (cm^2/V \cdot s)$	-	-	25 ^h	100 ^e	72 ^e	100 ^c	-
$\mu_h (cm^2/V \cdot s)$	-	-	150 ^h	12.5 ^e	20 ^e	31 ^c	-
τ_e (s)	-	-	-	$2.6 \cdot 10^{-9}$ e	$6.4 \cdot 10^{-10}$ e	$4.2 \cdot 10^{-9}$ e	-
τ_h (s)	-	-	-	$7.1 \cdot 10^{-9}$ e	$2.4 \cdot 10^{-12}$ e	$1.5 \cdot 10^{-11}$ e	-
SRH Trap Offset (eV)	-	-	-	-	1.2^{i}		-
C_n (cm^6/s)	-	-	-	-	$1 \cdot 10^{-31}$ d	-	-
C_p (cm^6/s)	-	-	-	-	$1 \cdot 10^{-31}$ d	-	-
$R_r (cm^3/s)$	-	-	-	$2\cdot 10^{-15j}$	$1\cdot 10^{-20\mathrm{d}}$	-	-
Doping							
Dopant Type	-	-	p	p	n	n	-
Concentration (cm ³)	-	-	$5 \cdot 10^{19}$ k	$3 \cdot 10^{161}$	$5 \cdot 10^{17}$ e	$1 \cdot 10^{181}$	-
Interface Properties							
	Mo	SiO ₂ /CIGS	MoSe ₂ /CIGS	CIG	S/CdS	Al:Zı	nO
Force Ohmic	Yes	-	-		-	Yes	3
Surf. Charge Concent. (C/cm^2)	-	$-9\cdot10^{-7}\mathrm{m}$	-		-	-	

 $1\cdot 10^{7}{\text{n}}$

 $1\cdot 10^{7}{\text{n}}$

Yes

0

 $9.3\cdot 10^{5}{}^{\text{o}}$

 $4.8 \cdot 10^{5}$

Yes

0

 $1\cdot 10^{4\text{n}}$

 $1\cdot 10^{4\text{n}}$

Yes

0

 SRV_n (cm/s)

 ${\color{red} SRV_p} \ (cm/s)$

Trap Offset (eV)

Apply to Maj. Carriers

^aValue attained from [127]

^bValue attained from [128]

^cValue attained from [122]

^dValue attained from [100]

^eValue attained from [121]

^fValue attained from [129]

gValue attained from [130]

^hValue attained from [131]

ⁱValue attained from [132]

^jValue attained from [133]

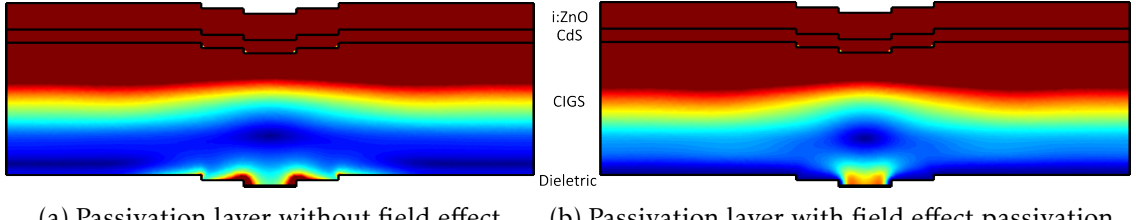
^kValue attained from [134]

^lValue attained from [108] $^{\rm m}$ Value attained from [109]

ⁿValue attained from [50]

^oValue attained from [75]

One of the ways that the SiO_x layer passivates the CIGS/Mo interface is through the field effect passivation. In short, the fixed negative charges in the insulator layer create an electric field that repels the electron minority carriers from the highly recombinative rear contact interface and the dieletric surface. This effect was accounted for during the creation of the CIGS electric model, and thus it is possible to visualize it in action. In Figure B.1 the reader finds the spacial distribution of the electron current density at a linear scale, for passivation layers with and without fixed charges in the dielectric layer:



(a) Passivation layer without field effect passivation.

(b) Passivation layer with field effect passivation.

Figure B.1: Simulated electron current density distribution in a passivated ultrathin CIGS solar cell.

By comparing the results between the passivation layer without fixed charges in Figure B.1a, and with fixed charges in Figure B.1b, it is visible that in the case where no fixed charges are present, the electron current is the densest at the surface of the dielectric. However, when fixed charges are present in the SiO_x layer, the current at the surface of the dielectric is completely repressed and driven away from the recombinative interface.

C | Python Tools

Throughout the duration of this thesis, several hundreds of optical and electrical simulations runs were performed. With each single simulation run possessing multiple datasets, and with each dataset requiring a different workflow, automated tools had to be developed, in order to automate these highly repetitive tasks. For that end, several Python scripts were developed. For the FDTD optical simulations, the scripts were capable of accurately extracting the optical absorption of complex 3D structures, the parasitic absorption of certain layers, the solar cell reflection and the 3D distribution of the charge carriers generation, accounting for the 3D shape of the CIGS absorber layer. In addition, the developed program had the capabilities of automatically setting up, running and processing the electrical simulations for each respective optical simulation.

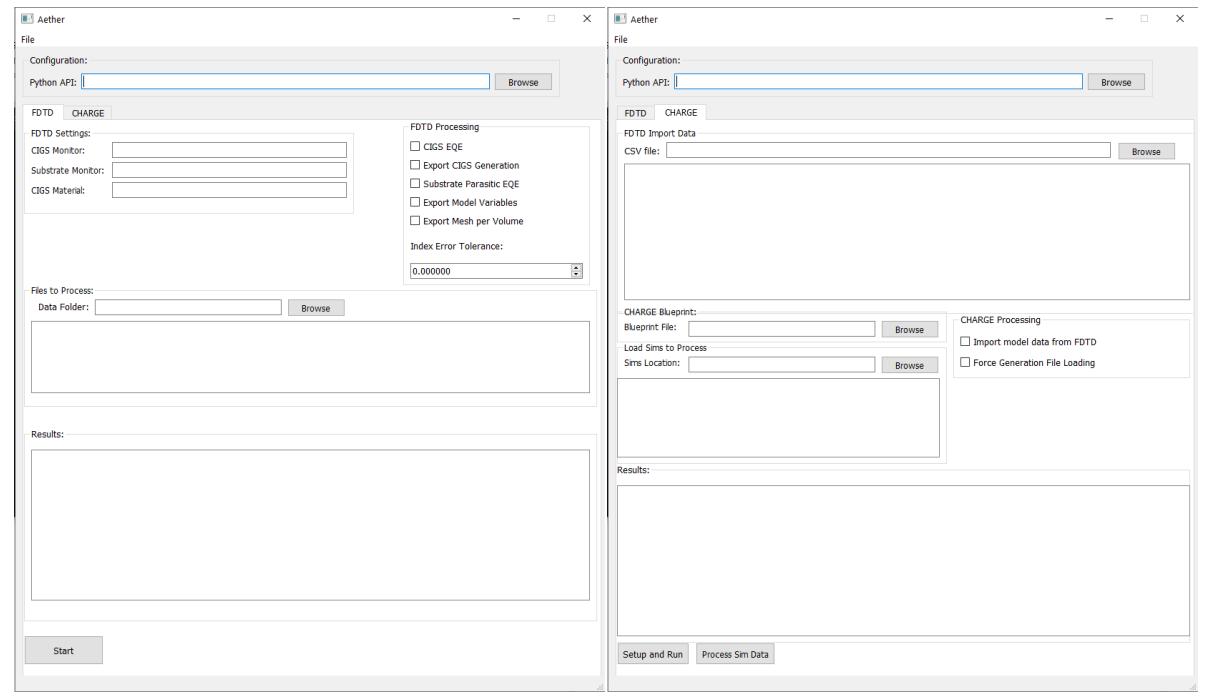


Figure C.1: Screen capture of the graphical user interface developed for the automation scripts.

In addition, the *Lumerical* data processing scripts were modified and optimized, in order to both reduce the processing time and RAM requirements. Thus allowing for either a faster workflow, or more accurate simulations due to the more efficient use of the computational resources available. In total, over two thousands lines of code were either newly written, modified or optimized throughout the duration of this thesis. At a later date, the developed tools will become available in an open-source licensing scheme, as part of a scientific publication.

Annex 1

COMMUNICATION



Optoelectronics

www.solar-rrl.com

Optical Lithography Patterning of SiO₂ Layers for Interface Passivation of Thin Film Solar Cells

Sourav Bose, José M. V. Cunha, Sunil Suresh, Jessica De Wild, Tomás S. Lopes, **João R. S. Barbosa**, Ricardo Silva, Jérôme Borme, Paulo A. Fernandes, Bart Vermang, and Pedro M. P. Salomé*

Ultrathin Cu(In,Ga)Se2 solar cells are a promising way to reduce costs and to increase the electrical performance of thin film solar cells. An optical lithography process that can produce sub-micrometer contacts in a SiO₂ passivation layer at the CIGS rear contact is developed in this work. Furthermore, an optimization of the patterning dimensions reveals constrains over the features sizes. High passivation areas of the rear contact are needed to passivate the CIGS interface so that high performing solar cells can be obtained. However, these dimensions should not be achieved by using long distances between the contacts as they lead to poor electrical performance due to poor carrier extraction. This study expands the choice of passivation materials already known for ultrathin solar cells and its fabrication techniques.

S. Bose, J. M. V. Cunha, T. S. Lopes, J. R. S. Barbosa, R. Silva, Dr. J. Borme, Prof. P. A. Fernandes, Prof. P. M. P. Salomé INL - International Iberian Nanotechnology Laboratory Avenida Mestre José Veiga, 4715-330 Braga, Portugal E-mail: pedro.salome@inl.int

S. Bose Angström Laboratory Solid State Electronics Ångström Solar Center Uppsala University SE-751 21 Uppsala, Sweden J. M. V. Cunha, Prof. P. M. P. Salomé Departamento de Física

Universidade de Aveiro Campus Universitário de Santiago 3810-193 Aveiro, Portugal

The ORCID identification number(s) for the author(s) of this article

can be found under https://doi.org/10.1002/solr.201800212.

IMEC - Partner in Solliance Leuven 3001, Belgium S. Suresh, Dr. J. De Wild, Prof. B. Vermang IMOMEC - Partner in Solliance Diepenbeek 3590, Belgium Prof. P. A. Fernandes CIETI

S. Suresh, Dr. J. De Wild, Prof. B. Vermang

University of Hasselt - Partner in Solliance

S. Suresh, Dr. J. De Wild, Prof. B. Vermang

Diepenbeek 3590, Belgium

Departamento de Física Instituto Superior de Engenharia do Porto Instituto Politécnico do Porto Porto 4200-072, Portugal

Prof. P. A. Fernandes

Universidade de Aveiro Aveiro 3810-193, Portugal

DOI: 10.1002/solr.201800212

1800212 (1 of 6)

© 2018 WILEY-VCH Verlag GmbH & Co. KGaA, Weinheim

Rear Optical Reflection and Passivation Using a Nanopatterned Metal/Dielectric Structure in Thin-Film Solar Cells

Tomás S. Lopes, José M. V. Cunha , Sourav Bose , João R. S. Barbosa, Jérôme Borme , Olivier Donzel-Gargand, Célia Rocha, Ricardo Silva, Adam Hultqvist, Wei-Chao Chen [0], Ana G. Silva, Marika Edoff, Paulo A. Fernandes, and Pedro M. P. Salomé

Abstract—Currently, one of the main limitations in ultrathin Cu(In,Ga)Se₂ (CIGS) solar cells are the optical losses, since the absorber layer is thinner than the light optical path. Hence, light

Manuscript received March 26, 2019; revised May 7, 2019; accepted June 2, 2019. Date of publication July 3, 2019; date of current version August 22, 2019. This work was supported in part by the Fundação para a Ciência e a Tecnologia (FCT) under Projects IF/00133/2015 and PD/BD/142780/2018, in part by The European Union's Horizon 2020 Research and Innovation Programme ARCIGS-M project under Grant Agreement 720887, and in part by NovaCell (028075) and InovSolarCells (029696) co-funded by FCT and the ERDF through COMPETE2020. (Tomás S. Lopes and José M. V. Cunha contributed equally to this work.) (Corresponding author: José M. V. Cunha.)

- T. S. Lopes, J. R. S. Barbosa, J. Borme, and C. Rocha are with the International Iberian Nanotechnology Laboratory, Braga 4715-330, Portugal (e-mail: tomas.lopes@inl.int; jr.barbosa@campus.fct.unl.pt; jerome.borme@ inl.int; cc.rocha@campus.fct.unl.pt).
- J. M. V. Cunha is with the International Iberian Nanotechnology Laboratory, Braga 4715-330, Portugal, with the Departamento de Física, Universidade de Aveiro, Campus Universitário de Santiago, Aveiro 3810-193, Portugal, and also with the I3N, Universidade de Aveiro, Aveiro 3810-193, Portugal (e-mail: jose.cunha@inl.int).
- S. Bose is with the International Iberian Nanotechnology Laboratory, Braga 4715-330, Portugal, and also with the Ångström Laboratory, Solid State Electronics, Ångström Solar Center, Uppsala University, Uppsala SE-751 21, Sweden (e-mail: sourav.bose@inl.int).
- O. Donzel-Gargand is with the International Iberian Nanotechnology Laboratory, Braga 4715-330, Portugal, and also with the Ångström Laboratory, Solid State Electronics, Ångström Solar Center, Uppsala University, Uppsala SE-751 21, Sweden (e-mail: olivier.donzel-gargand@angstrom.uu.se).
- R. Silva is with the International Iberian Nanotechnology Laboratory, Braga 4715-330, Portugal, and also with the CEFITEC, Departamento de Física, Faculdade de Ciências e Tecnologia, Universidade Nova de Lisboa, Campus de Caparica, Caparica 2829-516, Portugal (e-mail: rbe.silva@campus.fct.unl.pt).
- A. Hultqvist, W.-C. Chen, and M. Edoff are with the Ångström Laboratory, Solid State Electronics, Ångström Solar Center, Uppsala University, Uppsala SE-751 21, Sweden (e-mail: adam.hultqvist@angstrom.uu.se; chen.weichao@ angstrom.uu.se; marika.edoff@angstrom.uu.se).
- A. G. Silva is with the CEFITEC, Departamento de Física, Faculdade de Ciências e Tecnologia, Universidade Nova de Lisboa, Campus de Caparica, Caparica 2829-516, Portugal (e-mail: acs@fct.unl.pt).
- P. A. Fernandes is with the International Iberian Nanotechnology Laboratory, Braga 4715-330, Portugal, with the CIETI, Departamento de Física, Instituto Superior de Engenharia do Porto, Instituto Politécnico do Porto, Porto 4200-072, Portugal, and also with the I3N, Universidade de Aveiro, Aveiro 3810-193, Portugal (e-mail: paulo.fernandes@inl.int).
- P. M. P. Salomé is with the International Iberian Nanotechnology Laboratory, Braga 4715-330, Portugal, and also with the Departamento de Física, Universidade de Aveiro, Campus Universitário de Santiago, Aveiro 3810-193, Portugal (e-mail: pedro.salome@inl.int).

Color versions of one or more of the figures in this paper are available online at http://ieeexplore.ieee.org.
Digital Object Identifier 10.1109/JPHOTOV.2019.2922323

management, including rear optical reflection, and light trapping is needed. In this paper, we focus on increasing the rear optical reflection. For this, a novel structure based on having a metal interlayer in between the Mo rear contact and the rear passivation layer is presented. In total, eight different metallic interlayers are compared. For the whole series, the passivation layer is aluminum oxide (Al₂O₂). The interlayers are used to enhance the reflectivity of the rear contact and thereby increasing the amount of light reflected back into the absorber. In order to understand the effects of the interlayer in the solar cell performance both from optical and/or electrical point of view, optical simulations were performed together with fabrication and electrical measurements. Optical simulations results are compared with current density-voltage (J-V) behavior and external quantum efficiency measurements. A detailed comparison between all the interlayers is done, in order to identify the material with the greatest potential to be used as a rear reflective layer for ultrathin CIGS solar cells and to establish fabrication challenges. The Ti-W alloy is a promising a rear reflective layer since it provides solar cells with light to power conversion efficiency values of 9.9%, which is 2.2% (abs) higher than the passivated ultrathin sample and 3.7% (abs) higher than the unpassivated ultrathin reference sample.

Index Terms—Back/rear contact, Cu(In,Ga)Se2 (CIGS), light trapping, optical simulation, thin-film solar cells.

2156-3381 © 2019 IEEE. Personal use is permitted, but republication/redistribution requires IEEE permission. See http://www.ieee.org/publications_standards/publications/rights/index.html for more information.